Department of Physics and Astronomy

University of Heidelberg

Master thesis

in Physics

submitted by

Christoph Tremmel

born in Grünstadt

2012

Improving ion beam therapy treatment planning for metal implants by using dual-energy CT scanning

This Master thesis has been carried out by Christoph Tremmel

at the

German Cancer Research Center (DKFZ)

under the supervision of

Prof. Dr. Oliver Jäkel

and

Prof. Dr. Uwe Oelfke

Zusammenfassung:

Eine der größten Unsicherheiten in der Behandlungsplanung der Ionenstrahltherapie ist die Reichweitenvorhersage anhand von CT-Bildern. Nichtgewebeäquivalente Materialien und Materialien mit hoher Photonenabschwächung wie etwa Metalle können dieses Problem noch verstärken.

Die Zwei-Spektren-Computertomographie (DECT) erlaubt die Berechnung der Elektronendichte und effektiven Ladungszahl. Es konnte bereits in Untersuchungen gezeigt werden, dass diese zusätzliche Gewebeinformation eine genauere Reichweitenbestimmung ermöglicht.

Diese Arbeit untersucht die Anwendbarkeit des DECT Ansatzes für eine Reihe von Metallen von Aluminium ($Z = 13$) bis Wolfram ($Z = 74$). Auf einer 16 bit CT-Skala rekonstruierte DECT-Scans der Proben mit zusätzlicher rohdatenbasierter Strahlaufhärtungskorrektur wurden hierzu analysiert. Die Elektronendichte und effektive Ladungszahl konnte für Aluminium und Titan ($Z = 22$) mit Abweichungen im Prozentbereich bestimmt werden. Für Messproben mit $Z \geq 22$ konnten diese Größen nicht präzise bestimmt werden. Bis zu Molybdän ($Z = 42$) waren allerdings alle Proben anhand ihrer unterschiedlichen CT-Zahlen unterscheidbar. Die Genauigkeit der Ionenreichweitebestimmung konnte mit DECT gegenüber 120 kV CT für Aluminium von -11.46% auf 4.88% und für Titan von -36.4% auf 2.75% verbessert werden. Der Durchmesser fast aller Messproben konnte aus den DECT Bildern bis auf die Voxelgröße von 0.6 mm genau bestimmt werden. Streifenartefakte waren um die Aluminium- und Titanprobe schwach ausgeprägt. Starke Artefakte wurden um Materialien mit $Z \geq 26$ beobachtet.

Die Proben wurden außerdem mit Megavolt-Computertomographie (MVCT) untersucht, um DECT mit dieser konkurrierenden Methode zu vergleichen. Bei Materialien mit $Z \geq 26$ wurden mit MVCT bessere Resultate als mit DECT erzielt. Für klinische Routineanwendungen hat DECT allerdings den Vorteil schnellerer Scangeschwindigkeit und größerer technischer Ausgereiftheit des Scanners.

Als alternative Möglichkeit zur Reichweitenbestimmung ohne physikalisches Modell wurde Diskriminanzanalyse betrachtet. Bei einer tierischen Gewebeprobe wurden im Mittel nur geringe absolute Abweichungen von Referenz-Ionenreichweiten festgestellt.

Abstract:

One of the major uncertainties in ion beam therapy planning is the calculation of ion ranges in the patient's tissue from CT images. The presence of non-tissue-equivalent materials and materials with high photon attenuation like metals may aggravate this problem.

Dual Energy Computed Tomography (DECT) allows to compute the electron density and effective atomic number. It could already be shown that this additional material information enables a more precise calculation of ion ranges.

This thesis investigates the feasibility of the DECT approach for a range of metals from aluminum ($Z = 13$) up to tungsten ($Z = 74$). DECT scans of the samples reconstructed with a 16 bit CT scale and raw data based beam hardening correction were analyzed. The electron density and effective atomic number of aluminum and titanium ($Z = 22$) could be determined within the range of a few percent. These quantities could not be determined for samples with $Z \geq 22$, but the samples were distinguishable from each other by their different CT numbers up to molybdenum ($Z = 42$). The precision of the determined ion

ranges could be improved for aluminum from -11.46% to 4.88% and for titanium from -36.4% to 2.75% compared to ion range estimations from 120 kV CT. The size of nearly all metal samples could be assessed from the images with precision in the range of the voxel size of 0.6 mm. Streaking artifacts around the samples were minor for aluminum and titanium. For materials with $Z \geq 26$, severe artifacts could be observed.

The samples were investigated with Mega Voltage Computed Tomography to compare DECT with this rivaling method. It was found that MVCT yielded superior results in case of materials with $Z \geq 26$. However, DECT offers in clinical routine the advantage of faster scanning times and greater technical maturity of the scanner.

Discriminant analysis was tested as an alternative way to obtain ion ranges from Dual Energy CT images without physical model. Only small mean absolute deviations from reference ion ranges were observed for an animal sample.

Contents

1 Introduction

Ion beam therapy (IBT) offers in principle sharp dose distributions and therefore high dose conformality as charged ions deposit most of their energy shortly before they stop. The depth dose curve of ions in matter is characterized by a low plateau region and a high and sharp Bragg peak. Low entrance dose and the fact that ions stop shortly after the their bragg peak separate this treatment modality from conventional radiation therapy with x-ray photons.

However, several uncertainties impair its high precision potential. The conversion of computed tomography (CT) data to ion ranges during the treatment planning process is the most significant among those. The presence of metal implants even aggravates the problem due to high attenuation of photons. This leads to saturation of CT numbers and severe imaging artifacts. The consequences are incorrect CT values both in implants and surrounding tissue and subsequently wrong ion ranges. At present, approximately 50% of all patients at the Heidelberg Ion Beam Therapy Center (HIT) have at least minor implants. 5% of all patients have implants that may cause significant range uncertainties [10]. This may in extreme cases even lead to the rejection of patients with metal implants of high density.

Recently emerged Dual Energy Computed Tomography (DECT) imaging offers two CT contrasts and hereby allows to compute the electron density and effective atomic number of a material. This additional material information enables a more accurate prediction of ion ranges, especially for non-tissue materials [14], [40]. Additionally, novel pre-clinical reconstruction algorithms extend the common CT scale to 16 bit, i.e. beyond 3071 HU.

This thesis therefore investigated the potential to apply DECT for a more accurate prediction of ion ranges in metals with atomic number of 13 or higher. To do so, a series of metal samples with high purity from aluminum up to tungsten was studied. Measured ion ranges in those materials were compared to predictions obtained from DECT. The effective range of metals that can be measured with DECT was evaluated. A DECT Hounsfield look up table (HLUT) was used to calculate ion ranges in the sample materials. The accuracy of the estimation of the metal samples' sizes from CT images and the severeness of artifacts in the material around the metal samples were assessed.

The DECT method was compared to Mega Voltage CT (MVCT) which allows to measure even very dense materials because of the lower attenuation in this energy regime and may be considered as a competitor regarding the characterization of dense materials. Therefore, the metal samples were measured with MVCT and ion rages were calculated with a MVCT HLUT. The accuracy of the obtained ion ranges, size estimations of the samples and artifact severeness around the samples were compared to the respective results with DECT.

As a possible alternative, classification was studied to obtain ion ranges from DECT numbers directly without any physical model. It allows to assign ion ranges to regions in the DECT data space. A tissue sample was used to assess the applicability of the method. The resulting ion ranges were compared to range estimations obtained with a standard HLUT from 120 kV CT images.

In chapter 2 the fundamental physical and technical concepts used in this thesis are introduced. Chapter 3 describes the devices, imaging protocols and sample materials utilized in the measurements for this thesis. In chapter 4 the measurements and their results are presented. The results are finally discussed in chapter 5.

2 Fundamentals

2.1 Computed Tomography

Computed tomography is an imaging modality widely used in clinical practice. The basic idea is to take x-ray images of an object from many different angles using a fan beam. These two-dimensional x-ray projection images are then used to calculate the original three-dimensional image. This is usually done using filtered back projection, however iterative reconstruction has recently emerged as an alternative.

Today CT scans are normally recorded in spiral scan mode. This means that the couch with the patient is moved without stopping through the gantry where the x-ray tubes and detectors rotate continuously. This allows for much faster scanning than the method used before, where single rotations of source and detector around the patient are done and the couch is moved in between those rotations (this is also called "sequential mode"). In contrast to sequential mode, a correction is necessary in spiral scan mode to account for the slight shifts on the transversal axis induced by the continuous movement of the couch.

For general information about CT imaging see [17]. A comprehensive mathematical description of image reconstruction for spiral CT can e.g. be found in chapter 7 of [7].

2.1.1 The Quantity Measured in CT

Photons traversing matter experience attenuation, resulting in a decrease of the initial intensity. The signal measured in a CT scanner's detector array is proportional to the photon intensity decreased during the traversal through the patient's body. The attenuation of photons in matter is described by the Beer-Lambert law:

$$I(x) = I(0) \cdot e^{-\mu \cdot x} \tag{2.1}$$

with $I(x)$ being the intensity at point x, $I(0)$ being the initial intensity and μ the linear absorption coefficient. The latter consists of three contributing attenuation mechanisms at diagnostic x-ray energies: incoherent scattering (Compton scattering), the photoelectric effect and coherent scattering (elastic Rayleigh scattering):

$$\mu = \mu_{incoh} + \mu_{photo} + \mu_{coh} \tag{2.2}$$

Following [34], the linear absorption coefficient in the energy regime relevant for CT imaging (80-140 kV x-ray spectra) can be written as

$$\mu = \rho_e \cdot (F(E, Z) + Z^n \cdot G(E, Z)) \tag{2.3}$$

with ρ_e being the electron density of the traversed material, a scattering term $F(E, Z)$ accounting for elastic and inelastic scattering and the photo effect term $Z^n \cdot G(E, Z)$. The exponent n is chosen to be 4 in [34], [3] and [4].

The linear absorption coefficient is the physical quantity that determines CT contrast. In case of a homogeneous object and a monochromatic photon beam it follows directly from from 2.1:

$$\mu = \frac{1}{x} \cdot ln\left(\frac{I(0)}{I(x)}\right) \tag{2.4}$$

$ln\left(\frac{I(0)}{I(x)}\right)$ can be regarded as the value of the measured projection. In case of heterogeneous objects μ is a function of the position along the projection line, i.e. $\mu(x, y)$. Therefore, it is in general necessary to employ more sophisticated methods to calculate the original $\mu(x, y)$ distribution from the measured projections. The most common method is filtered back projection. For a detailed explanation see also chapter 1.2 of [17] and chapter 5 of [7].

Usually, the radiation source used in CT does not emit monoenergetic photons but a x-ray spectrum. Image reconstruction algorithms account for this fact, but it still can be a source of problems (see 2.1.6).

2.1.2 Hounsfield Units And The CT Scale

The reconstructed linear attenuation coefficient of the material in a volume element $\mu(x, y)$ is usually not displayed directly but relative to the linear attenuation coefficient of water. The so called CT number is then defined as

$$CT = \frac{\mu - \mu_{water}}{\mu_{water}} \cdot 1000 \tag{2.5}$$

The measurement unit is called "Hounsfield Unit" or "HU"[1].

The reason for the normalization of CT numbers is that μ depends on the energy spectrum. A display of μ alone would make it hard to compare images between scanners with different energy spectra[2]. The normalization to water makes the CT numbers of water and water-like materials such as soft tissues independent from the energy spectrum. For more dense materials, however, different CT numbers are observed for different photon energy spectra. Further information on this topic can e.g. be found in chapter 1.2 of [17].

The scale of a standard CT image in Hounsfield units ranges from -1024 to 3071, i.e. the image information is stored with 12 bit ($2^{12} = 4096$). This is sufficient to cover the typical CT values of all human tissues. Water has by definition a CT value of 0 HU , air has -1000 HU. High Z materials like metals, however, can only be measured until they reach the highest CT value 3071. Aluminum is the only metal used in this thesis that has a CT value below the upper limit of the 12 bit CT scale. Titanium with $Z = 22$ is

[1] Named after the the inventor of CT, Godfrey Hounsfield

[2] For example due to filtration of the x-rays and other scanner-specific factors or because a different tube voltage was chosen.

already beyond that scale. Therefore, the measurement scale must be extended to measure materials with high atomic numbers. This can be done by using a 16 bit scale for the CT values which extends the CT scale to $2^{16} - 1025 = 64511$[3].

2.1.3 Dual Energy CT

Dual energy CT or DECT measures CT numbers of an object with two different photon energy spectra. The tubes are operated at different voltages and allow to measure two CT numbers for each voxel in different photon attenuation regimes. Due to the energy dependency of photon attenuation, additional tissue information can be obtained [16]. The attenuation of the high energy photon beam is dominated by Compton scattering, whereas the attenuation of the low energy photon beam is dominated by the photo effect. The cross section of the photo effect depends in contrary to Compton scattering strongly on the effective atomic number. This additional information makes it possible to calculate the electron density and effective atomic number of a material since one has two measured quantities (μ at low and high energy) that can be described by two equations with two unknowns (ρ_e and Z):

$$\mu_{low} = \rho_e \cdot (F_{low}(E, Z) + Z^n \cdot G_{low}(E, Z))$$
$$\mu_{high} = \rho_e \cdot (F_{high}(E, Z) + Z^n \cdot G_{high}(E, Z))$$

Since polychromatic x-ray spectra are used, $F_k(E, Z)$ and $G_k(E, Z)$ are averaged over the energy spectra E^k:

$$F_k(E^k, Z) = \sum_i \omega_i^k F(E_i^k, Z)$$
$$G_k(E^k, Z) = \sum_i \omega_i^k G(E_i^k, Z)$$

with $k \in \{\text{low, high}\}$ and spectral weights ω_i^k [40].

To separate both spectra further, the high energy beam may be filtered through a thin sheet of metal to remove low energy photons.

2.1.4 Electron Density And Effective Atomic Number

It is possible to calculate relative electron density and effective atomic number from DECT images. The relative electron density is the electron density of a material divided by the electron density of water. The electron density of a composite material m can be written as:

$$\rho_e^m = N_a \cdot \rho_m \cdot \sum_i \frac{\omega_i Z_i}{A_i} \tag{2.6}$$

[3]The scale starts at -1024 and includes 0.

with N_a being Avogadro's constant, ρ_m the mass density of material m and ω_i the proportion by weight, Z_i the atomic number and A_i the relative atomic weight of the elements of material m.

The effective atomic number of a composite material is the atomic number of a virtual homogeneous material with equal x-ray attenuation properties as the composite material for a specific x-ray spectrum (see [43]). It can be defined as

$$Z_{eff} = \left(\frac{\sum_i w_i \cdot Z_i^E \cdot \frac{Z_i}{A_i}}{\sum_i w_i \cdot \frac{Z_i}{A_i}} \right)^{\frac{1}{E}} \tag{2.7}$$

with w_i being the mass weight, Z_i the atomic number and A_i the relative atomic weight of material i. E is a parameter that depends on the x-ray energy spectrum. In this thesis $E = 3.1$ is used.

2.1.5 MVCT

An alternative to CT with kilo voltage photon spectra is mega voltage CT which uses photon beams produced by mega voltage linear accelerators. In this energy regime, the contrast of soft tissue is reduced in comparison to kilo voltage CT and images suffer from more noise. However, due to the lower attenuation of mega voltage photons by even very dense materials like metals, MVCT does not suffer from image artifacts introduced by such materials in kV CT. This makes MVCT a promising candidate for the evaluation of metal objects. Further, the attenuation in this regime is dominated by Compton scattering which has only a weak dependency on the atomic number. Therefore, one would expect a close relationship between MVCT number and electron density.

2.1.6 Imaging Artifacts in CT

A number of imaging artifacts may occur in CT. The types of artifact relevant to this thesis are except for partial volume artifacts those related to the high photon attenuation of high density materials. Other artifacts may be induced by patient motion or incorrect sampling. They are not covered here as they are beyond the scope of this thesis.

Beam Hardening

Beam hardening occurs due to the energy dependence of the attenuation coefficient $\mu(E)$. Photons with lower energy experience stronger attenuation than high energy photons. The mean photon energy of the x-ray spectrum is therefore shifted to a higher energy while the photon beam traverses matter (the spectrum "hardens"). The detectors employed in today's CT scanners usually measure the total intensity of the whole photon spectrum. Photon energies cannot be distinguished in the detectors of these scanners[4]. The total intensity measured for projections that contain contributions from materials with strong attenuation are therefore inconsistent with projections that don't contain such contributions. This

[4]So called "spectral CT" with energy sensitive detectors is a subject of current research but not yet available for clinical applications due to various technical issues [31]

leads eventually to artifacts in the image. One type of artifact caused by beam hardening is "cupping", which can be noted by a decrease of CT values towards the center of a dense object due to the lower attenuation after the spectrum was hardened in the outer parts of the object. Very dense objects like certain bones or metal implants can also lead to streaks in the back-projected image because reconstruction with filtered back projection smears the incorrect values over the image along the directions of the affected projections. The base of skull is one region where this effect may occur. See also chapter 8.5.2 in [7] on this topic.

It is possible to correct for beam hardening caused by a known substance. Therefore, a beam hardening correction for soft tissue is usually done by default. A data base of beam hardening measured for water phantoms of various sizes is used to estimate the beam hardening due to the patient's soft tissue. This possible because soft tissue is more or less water-equivalent. However, this so-called water precorrection is not sufficient for denser materials like bone or even metals. Further beam hardening correction methods are for example proposed in [19] and specifically for metal implants in [25]. Both use segmentation of the artifact causing, dense materials to apply a raw data based correction. [35] presents an iterative correction method and gives in addition an overview over of beam hardening correction methods. These techniques describe how beam hardening can be dealt with in single energy CT.

For monoenergetic photons beam hardening does not occur because there is only one photon energy. Dual energy CT therefore allows to correct for beam hardening because it is possible to calculate virtual monoenergetic images from the DECT measurements by decomposing the DECT information into a photo effect component and a Compton scattering component and combining them linearly. This technique was already proposed in the mid 1970s [1] and later implemented [8]. [20] describes an iterative method to correct for beam hardening in DECT images.

Photon Starvation

Photon starvation occurs when attenuation is so strong that effectively no photons reach the detector[5] Projections through a metal object where no photons are detected suggest that the object has an infinite attenuation coefficient. Subsequently this leads to inconsistent projections for certain voxels around the high density object because the infinite attenuation of the projection(s) through the object cannot be compensated by other projections where photon starvation does not occur. Reconstruction with filtered back projection then smears the incorrect values over the image along the directions of the projections through the metal object. Images affected by this kind of artifact exhibit bright and dark streaks around the artifact-causing object. Chapter 8.5.6 of [7] covers this topic more in depth.

Iterative reconstruction of inconsistent rays may be a possibility to reduce these artifacts. Basically, one identifies and removes projections for which total absorption occurs and tries to estimate their value from adjacent projections. The affected projections can be identified by segmentation of the artifact-causing object in the reconstructed image or by more sophisticated methods directly in raw data space. A number of methods to do so have been proposed [39], [44], [36], [37].

[5] Of course, this rather means that the number of photons reaching the detector is so low that the signal cannot be distinguished from noise.

(a) An example for beam hardening due to dense bone. Reprinted from [7], p. 369.

(b) Streak artifacts due to photon starvation. The streaks are centered around the dense objects, in this case dental implants.

Figure 2.1

Scattering

Scattering is one of the mechanisms contributing to attenuation. If the CT scanner is equipped with two detectors as in Dual Energy CT, photons produced in one tube may be scattered into the detector belonging to the other tube. This additionally hampers image quality. Normally the signal would still be higher than the contribution by cross scattering. However, if the signal is low because the photon beam traversed objects with high attenuation, the scattered photons may become the main contribution to the signal. This leads to inconsistent projection in filtered back projection which eventually lead to streaking artifacts. This problem can to a certain extent be circumvented by additional collimation of the detector elements. Chapter 8.5.7 of [7] illustrates the problem more detailed.

For more information on scattering and cross scattering between detectors in DECT see also [11] on the impact on image quality. On scatter correction approaches see [28] and [24], the latter introducing two correction methods specifically for DECT. One method assumes that cross scattering is mainly scattering from object surfaces and uses look-up tables containing measurement data of surface scattering for different surface shapes for a correction. The second method corrects for cross-scattering by using real time data from a cross-scatter sensor mounted on the CT scanners detector(s) outside of the beam penumbra.

Partial Volume Artifacts

For objects with sharp edges or very small objects partial volume artifacts may be observed. If the boundary between two objects is not exactly at the edge of a detector element, the intensity measured in the detector is given by a linear combination of ray intensities that would occur for each object individually. According to 2.1.1 the value of a projection P is in principle $P = ln\left(\frac{I(0)}{I(x)}\right)$. If the beam traverses two neighboring objects with different attenuation coefficients, the projection P is given by the logarithm of a linear combination of

the two intensities belonging to each object: $ln\left(\omega \cdot I_1 + (1-\omega) \cdot I_2\right)$. This is in general not equal to a linear combination of the logarithms of intensities $\omega \cdot ln\left(I_1\right) + (1-\omega) \cdot ln\left(I_2\right)$ because the logarithm is not a linear function. This non-linearity means that the CT values of voxels containing two objects are not an average of the CT values the individual objects would have. Partial volume effects lead to errors therefore especially if the gradient in density between the two objects is very high. Small metal implants are one example where this kind of artifact emerges. A detailed description of this problem can be found in chapter 8.5.1 of [7].

Object Size

Without appropriate windowing[6] the size of high density objects may appear as too large or too small. This can be understood by considering how a simple rectangle object of high density is reconstructed using filtered back projection. Figure 2.2a shows a one dimensional profile in x direction through a titanium rod measured in CT. Two vertical black lines indicate the edges of the rod. Full width at half maximum is a good approximation for the true rod diameter. In figure 2.2b the window reaches from -1024 HU to 1000 HU. The diameter suggested by this image is larger than the actual rod diameter. In the case of objects with very high attenuation coefficient, the 12 bit CT scale may prevent appropriate windowing because its maximal CT number 3071 is not high enough to set the right window limits like in this example. It may therefore be hard to obtain precise information on the object's size from the image if an object's CT number is beyond the standard 12 bit CT scale.

Ultimately, the problem occurs because the rod's edges are not reconstructed perfectly vertical as they are in reality. However, if one accepts imperfect image reconstruction as a given fact, the reason for wrong size estimations is inappropriate windowing. In case of dense objects sufficient windowing may be impossible in 12 bit CT images due to insufficient range of the CT scale.

2.2 Ion Beam Therapy

Ion Beam Therapy offers in principle very high dose conformality. However, the narrow dose peaks at the end of the ions path demand a precise knowledge of the ion range in the patient's tissue. Range uncertainties of a few percent that are acceptable in photon therapy may lead in the worst case to dose peaks in organs at risk in ion beam therapy. Therefore it is essential to know ion ranges in the patients tissue as exact as possible.

The CT numbers of materials with high atomic number can usually not be measured in kilo voltage CT scanners. This means that no ion ranges are available for these materials in the treatment planning process. The artifacts in the tissue around the metal object add to the problem by causing inaccurate CT numbers. Range uncertainties can be the consequence and may eventually lead to inaccurate treatment. In [15] the typical range uncertainty in case of irradiation through a hip endo prosthesis is estimated as 18 % for a steel prosthesis and 5% for titanium..

[6] Since the human eye can only distinguish a limited number of gray values, CT images often focus on a subrange of the whole scale to highlight certain features, e.g. soft tissue contrast.

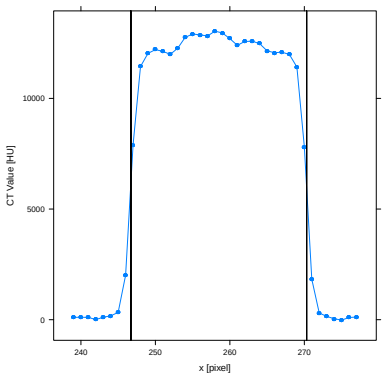

(a) Profile of a titanium rod measured in the CT. Black lines mark the true edges of the rod.

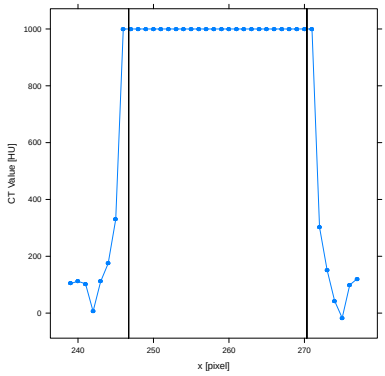

(b) The same rod, but with a upper limit of the CT number window of 1000 HU. Black lines mark the true edges of the rod. The size of the titanium rod is clearly overestimated.

Figure 2.2

To determine ion ranges in the patient's tissue a CT scan is performed and the CT numbers are used to obtain ion ranges. This is feasible since both CT number and stopping power of ions depend on the electron density. The next paragraphs introduce the technique currently used in clinical practice and subsequently a novel approach using DECT.

2.2.1 The Stopping of Ions

The stopping power of a material relative to the stopping power of water or relative stopping power is the actual input parameter for treatment planning systems. As described, it is usually obtained from CT images. The stopping power is given by the Bethe formula, see e.g. chapter 2 of [23]. The relative stopping power is essentially a function of the relative electron density and the logarithm of the mean ionization potential of a material m:

$$\frac{S_m}{S_w} = \frac{\rho_e^m}{\rho w_e} \cdot f(ln(I_m)) \tag{2.8}$$

The mean ionization potential of a composite material m can be computed using the Bragg additivity rule:

$$ln(I_m) = \left(\sum_i \frac{\omega_i Z_i}{A_i} ln(I_i)\right) \left(\sum_i \frac{\omega_i Z_i}{A_i}\right)^{-1} \tag{2.9}$$

with Z_i, A_i, ω_i and I_i being the atomic number, relative atomic weight, proportion by weight and mean ionization potential of element i of the composite material.

2.2.2 Water Equivalent Path Length WEPL

An empirical concept to describe the range of ions of a certain energy in matter is provided through the water equivalent path length (WEPL, see [27]). It is defined as

$$WEPL = \frac{P_m - P_w}{d} \tag{2.10}$$

with P_m being the depth of the distal end of the depth dose curve in water at 90% maximum value when an additional slab of material was placed in the beam path, P_w the same position of the depth dose curve without material slab in the beam path and d the slab thickness. Figure 2.3 shows the measurement principle. The depth dose curve of the ion beam is measured in a water column with and without a slab of the sample material in front of the column and the WEPL is calculated as described.

The WEPL of a certain material specifies the length of a water slab that would lead to the same ion range in a water column as a slab of one length unit of the material. If a material has for instance a WEPL of 2, one would need 2 cm of water to observe the same ion range as with a 1 cm slab of the material. Therefore, the ion range in water R_w may be written as the product of the ion range in the material and its WEPL $R_m \cdot WEPL_m$. If the ion range is approximated by the CSDA range

$$R_m^{CSDA} = \int_{E_0}^{0} \frac{1}{S_m} \, \mathrm{d}E \tag{2.11}$$

the WEPL is related to the relative stopping power $\frac{S_m}{S_w}$ in the following way:

$$WEPL_m \propto \frac{S_m}{S_w} \tag{2.12}$$

with the stopping power of the material S_m and the stopping power of water S_w. Here it is assumed that the relative stopping power is independent of the energy.

2.2.3 Stoichiometric Hounsfield Look-Up Table

A simple way to relate CT number and corresponding ion range would be to measure both quantities for a set of tissue equivalent materials and fit the results to obtain a relation between these quantities. This is sometimes called "empirical HLUT". At present, a stoichiometric Hounsfield look-up table is used instead. It is the current state-of-the-art method to relate 120 kV CT numbers and ion ranges. The basic idea is to use materials of known composition to calibrate a mathematical model of the cross sections of photo effect, coherent and incoherent scattering for a specific CT scanner. The photon attenuation cross sections from 2.2 are parametrized in the following way

$$\sigma = K^{ph} Z^{3.62} + K^{coh} Z^{1.86} + K^{KN} \tag{2.13}$$

$K^{ph} Z^{3.62}$ represents the photo effect, $K^{coh} Z^{1.86}$ coherent scattering and K^{KN} the Klein-Nishina cross section for incoherent scattering. The energy dependency is included in the

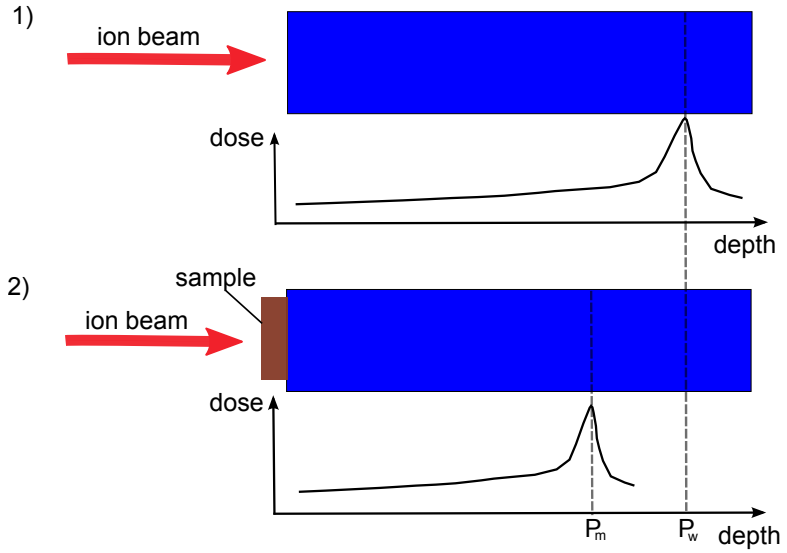

Figure 2.3: The ion range in water is first measured without a sample material in 1). Then a slab of the sample material is placed in front of the water column and the ion range is measured again in 2).

model parameters K. The calibration materials do not need to be tissue equivalent as they are only used to find the model's parameters.

The electron density and effective atomic number of tissues can be computed using the relations from 2.1.4. The exponent E in 2.7 must be set to the values of the particular exponents of Z in 2.13, so actually the effective atomic number has to be calculated for the photo effect part and the coherent scattering part seperately. Once the cross section and electron density of a material is computed, it is possible to calculate its CT number. Thus, in the next step the CT numbers of a number of body tissues is calculated using tissue composition tables. Analogously, one may calculate the relative stopping power of tissue materials from these tables using the relations from 2.2.1. In the last step, the computed CT numbers and stopping powers are used to set up a scanner-specific HLUT. They serve as nodes between which the HLUT is linearly interpolated. This method showed to be more precise than a CT number to ion range fit using tissue equivalent materials. A concise description of the method can be found in [29]. Figure 2.4 shows an example of a stoichiometric HLUT[7].

2.2.4 DECT Look-Up Table

The relative electron density and effective atomic number obtained from DECT can be used to calculate the relative stopping power directly. To do so, the tissue parameter occurring in the Bethe formula must be determined. The relative electron density is immediately available from DECT. The mean ionization potential is not available in a straight-forward way but can be parametrized by the effective atomic number. This method was proposed

[7]Provided by B. Ackermann, HIT

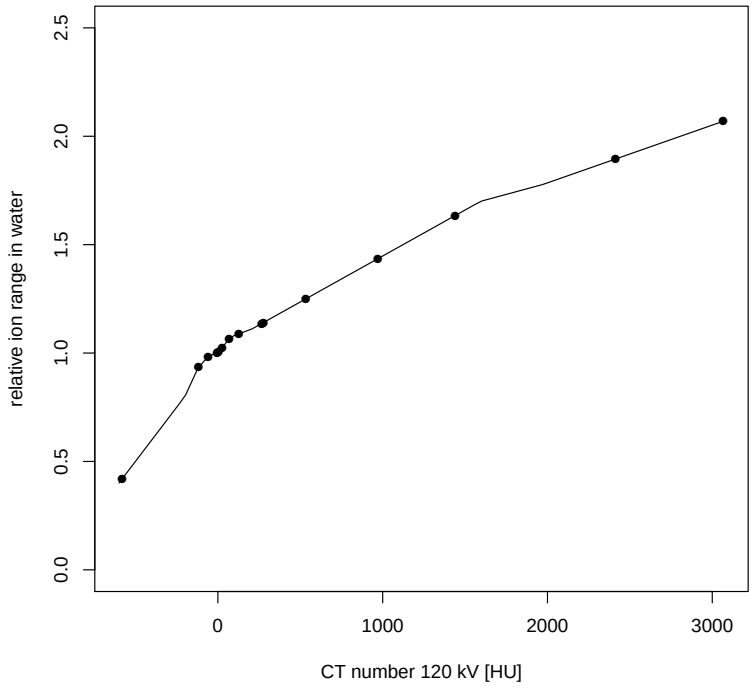

Figure 2.4: A standard stoichiometric Hounsfield look up table to convert 120 kV CT numbers to ion ranges. The data points are measurements of Gammex tissue equivalent materials and are plotted for illustration. The Gammex materials are introduced in the next chapter.

by N. Hünemohr [13]. The relative stopping power is then calculated as follows:

$$\frac{S_m}{S_w} = \frac{\rho_m^e}{\rho_w^e} \cdot \frac{12.77 - a \cdot ln(Z_{eff}) - b}{8.45} \tag{2.14}$$

with $\frac{\rho_m^e}{\rho_w^e}$ being the relative electron density, Z_{eff} the effective atomic number and fit parameters $a = 0.41$ and $b = 3.4$. The $ln(Z_{eff})$ part parametrizes the mean ionization potential occurring in the Bethe formula linearly. The remaining numerical parameters of 2.14 include other quantities occurring in the Bethe formula: physical constants, the mean ionization potential of water for which 75 eV is used and β which is 0.6.

2.3 Discriminant Analysis

Discriminant Analysis is a method used to classify (multivariate) data. Each data point of the data sample is assigned a class based on one or more observation variables. An example would be the if two CT numbers of a sample material at different voltages were measured (the observation variables) and one would try to assign a stopping power (the class) to the sample based on these two observations.

To do so, the data points belonging to a certain class are fit with a (multivariate) Gaussian. Then discriminant functions are used to separate regions belonging to different classes in the space of the observational variables. The discriminant functions are functions of the observation variables. If the covariance matrices of the Gaussians are not identical, the discriminant functions are quadratic; the method is then called quadratic discriminant analysis or QDA. The discriminant function can formally be written as

$$\delta_k(x) = \mathbf{x}^{Tr} A\, \mathbf{x} + b\, \mathbf{x} + c \tag{2.15}$$

with $\mathbf{x}$ being a vector of observations and k the class. The parameters of the discriminant function are calculated from the Gaussian's parameters.

If the covariance matrices of the Gaussians used to describe the data distribution of each class the the observation space are identical, the discriminant functions are linear. This is called linear discriminant analysis or just LDA. LDA is a special case of the more general QDA where all quadratic terms cancel due to the identity of the covariance matrices.

To use discriminant analysis one must first estimate the parameters of the Gaussians which describe the distribution of data points of each class. This is done by using a set of data where the class of each data point is already known. Gaussians can then be fit to the data sample and the parameters of the Gaussians be calculated. After that the Gaussian parameters allow to calculate discriminant functions that separate class regions in the observation space. This is sometimes called "Learning". Once the discriminant functions are obtained they can be used to classify new data where the classes are unknown. For a more detailed description of this topic see [12] Chapter 4.2.

The primary result of discriminant analysis are the predicted classes. However, it is possible to compute the posterior probability of a certain class for the sample using the assumed probability distribution of the sample and that of the learning data ([12] Chapter 7.7).

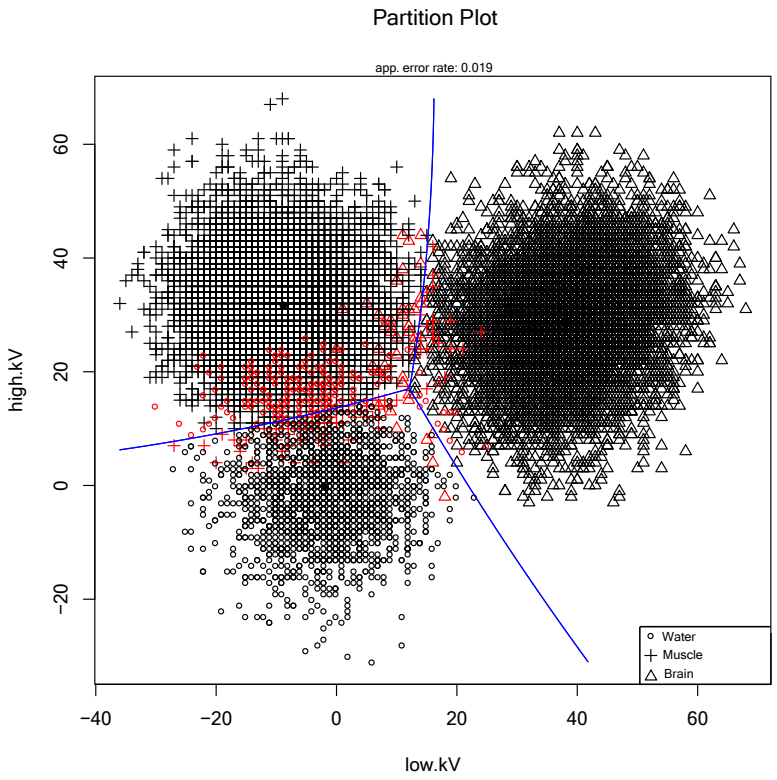

Figure 2.5: Example for classification with QDA. Two CT numbers measured with 80 kV and 140 kV are used to predict relative ion rages in three tissue equivalent materials. The three ion range classes are clearly seperated by the discriminant functions. Red color indicates data points that were classified incorrectly. Note that neither of the two CT numbers alone would suffice to separate all three samples.

3 Materials And Methods

This chapter describes the devices, experimental techniques and sample materials used in this thesis. In the first section the measured materials and phantoms are introduced. In the next section the scanning devices are presented and the employed protocols and image types are specified. The last section of this chapter covers the measurement of ion ranges at the Heidelberg Ion Beam Therapy Center (HIT).

3.1 Sample Materials

3.1.1 PMMA phantom

In the CT measurements cylindrical PMMA phantoms were used to simulate surrounding tissue that would be present in a real patient. This is necessary to account for beam hardening effects caused by additional absorbing material around the region of interest. The phantoms used in the measurements have outer radii of 14 mm, 25 mm, 50 mm and 80 mm. Several phantom radii were used to investigate if the imaging protocols are stable under variation of phantom size.

3.1.2 Used Material Sets

To investigate the performance of the imaging modalities considered in this thesis, three material sets were set up. One set is a collection of metals, the other two sets consist of tissue-equivalent and non-tissue-equivalent polymers. All materials are cylindrical rods with a diameter of 15 mm (metals) or 28 mm (non-metals) and lengths between 50 mm and 56 mm. Table 3.5 gives on overview of all sample materials and some material properties relevant to this study.

Metal Samples

To assess the image properties of metal implants a set of metals covering (effective) atomic numbers from 13 (Aluminum) to 79.99 (MCP-96 alloy) was assorted. The selected materials are aluminum, titanium, iron, copper, molybdenum, tin, tungsten and MCP-96[1]. All materials except MCP-96 are pure (>99.5%) to make sure that the electron density and the effective atomic number are well defined. Furthermore, titanium and molybdenum were included as they are relevant implant materials. Especially titanium is highly biocompatible and often used in implants. The metal parts of modern hip prostheses, for example, are often either made from titanium or cobalt-chromium-molybdenum alloys. Tungsten was included to act as a affordable substitute for gold (Z = 79) which is frequently used

[1] An alloy comprised of 52% bismuth, 32% lead and 16% tin by MCP Mining and Chemical Products Ltd. Northants, England

as material for dental crowns. MCP-96 is the only alloy. It normally serves in radiation therapy as collimation material. It was chosen to serve as a high upper limit of the Z scale because of it's high effective atomic number.

Figure 3.1: The metal rods used in the CT measurements. From left to right: MCP-96, aluminum, titanium, iron, copper, molybdenum, tin, tungsten.

Gammex Tissue Equivalent Materials

The second material set is composed of tissue equivalent materials. These materials are manufactured by Gammex[2] and are included in the Tissue Characterization Phantom Gammex 467. Normally they are used for quality assurance in radio therapy. The inserts are made from plastic and try to mimic the photon attenuation properties of real tissues.

Figure 3.2: Gammex tissue equivalent materials used in the CT measurements. First row from left to right: Lung (LN-450), Adipose (AP6), Breast, CT Solid Water, Muscle, Brain, Liver LV1. Second row from left to right: Inner Bone, Bone B200, Bone CB2-30% Mineral, Bone CB2-50% Mineral, Cortical Bone SB3 and the true water bin.

[2]Gammex Inc., Middleton, WI, USA

Plastic Materials

A third material set is comprised of various plastic materials without tissue like properties. They are normally not found in the human body but may be used as phantom materials in quality assurance in radiation therapy. In addition, PEEK materials are utilized in orthopedic surgery, while PMMA may be used as a component in bone cement to anchor artificial joints like hip endoprostheses [5].

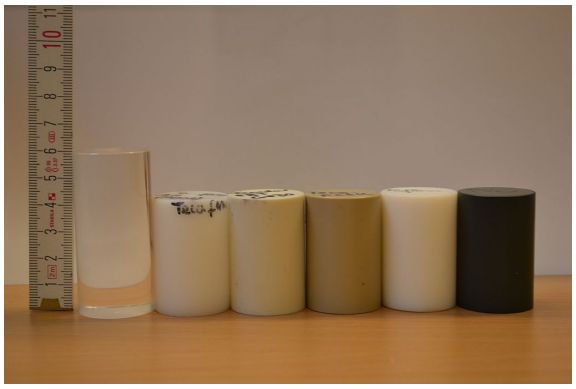

Figure 3.3: Polymers used in the CT measurements. From left to right: PMMA, Tecaform, Tecadur, Tecapeek, Teflon, PVC.

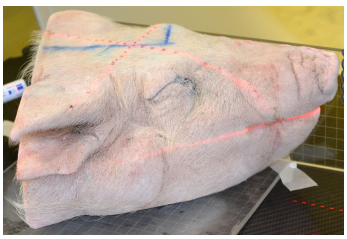

(a) Pig head sample.

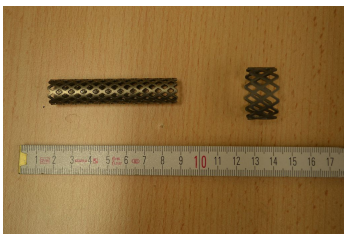

(b) Two Harms cages made from titanium.

(c) Hip endoprosthesis. Metal parts made from Protasul 10 alloy.

Figure 3.4

3.1.3 Tissue And Implant Samples

In addition to the materials described above, a small number of realistic tissue and implant samples was studied: A frozen pig head (Figure 3.4a), a hip endoprosthesis and two harms cages (Figure 3.4b and 3.4c). The pig head sample is in fact previously a measured data set comprised of 120 kV images measured on a Siemens Somatom S4 and DECT images measured on a Siemens Somatom Definition Flash with 80/140 kV. These data were supplied by N. H ünemohr. The implant samples are a hip endoprosthesis made from Protasul 10, a Co-Cr-Ni-Mo alloy [30]. The harms cages are made from an Ti-Al-V alloy (Fa. DePuy, DIN ISO 5832-3). The implants were embedded in a 4% agarose gel to simulate soft tissue.

3.2 CT Scanners And Image Types

3.2.1 Siemens Somaton Definition Flash

The Siemens Somatom Definition Flash is a dual source CT scanner. It features two x-ray tubes at an angle of 95° and a detector array opposite of each x-ray tube. It can be used for fast imaging and 4D CT in cardiac imaging. If the tubes are operated at different voltages, dual energy CT is possible.

The device allows to operate the tubes at 70, 80, 100, 120 and 140 kV. The high energy tube is equipped with a tin filter which allows to further separate the photon spectra. This feature can be accessed by selecting “Sn 140 kV” as voltage. The spectra relevant in this thesis are the 80/140Sn kV and 100/140Sn kV spectra. The ratio of the currents of both x-ray tubes is always fixed to predefined values. The value of these ratios depend on the chosen voltages and the image protocol and can be found in [32]. The field of view is 500 mm for detector A and 332 mm for detector B [16].

3.2.2 Tomotherapy HiArt II

The Tomotherapy HiArt II manufactured by Accuray[3] is a tomotherapy treatment device. It is basically a 6 MV linear accelerator mounted on a gantry that can be moved around the patient. On the opposite side a detector array is installed. This setup allows to irradiate

[3] Accuray, Sunnyvale, CA, USA

Figure 3.5: Overview of all sample materials.

Materials	Density [g/cm3]	Relative Electron Density	Effective Atomic Number	Relative Atomic Mass A (mean)	I [eV]	WEPL	Composition	Set
Lung	0.46	0.444	7.622	12.37	71.48	0.444	8.47% H, 59.57% C, 1.97% N, 18.11% O, 11.21% Mg, 0.58% Si, 0.1% Cl	Gammex
Adipose	0.942	0.925	6.33	10.86	65.47	0.943	9.06% H, 72.30% C, 2.25% N, 16.27% O, 0.13% Cl	Gammex
Breast	0.988	0.965	6.938	11.25	66.9	0.983	8.59% H, 70.11 % C, 2.33% N, 17.90% O, 0.13% Cl, 0.95% Ca	Gammex
Solid Water	1.018	0.989	7.645	11.80	68.81	1.001	8.00% H, 67.30% C, 2.39% N, 19.87% O,0.14% Cl,2.31% Ca	Gammex
Muscle	1.05	1.019	7.649	11.78	68.65	1.033	8.10% H, 67.17% C, 2.42% N, 19.85% O, 0.14% Cl, 2.32% Ca	Gammex
Brain	1.052	1.048	6.238	10.46	62.61	1.064	10.83% H, 72.54% C, 1.69% N, 14.86% O, 0.08% Cl	Gammex
Liver	1.089	1.058	7.649	11.79	68.73	1.073	8.06% H, 67.01% C, 2.47% N, 20.01% O, 0.14% Cl, 2.31 Ca	Gammex
Inner Bone	1.147	1.099	10.231	14.47	77.11	1.099	6.67% H, 55.64% C, 1.96% N, 23.52% O, 3.23% P, 0.11% Cl, 8.86% Ca	Gammex
Bone Mineral	1.153	1.105	10.234	14.49	77.18	1.108	6.65% H, 55.52% C, 1.98% N, 23.64% O, 3.24% P, 0.11% Cl, 8.87% Ca	Gammex
CB2-30%	1.333	1.278	10.685	14.82	77.57	1.263	6.68% H, 53.58% C, 2.12% N, 25.61% O, 0.11% Cl, 12.01% Ca	Gammex
CB2-50%	1.56	1.47	12.307	17.64	88.02	1.426	4.77% H, 41.63% C, 1.52% N, 32% O, 0.08% Cl, 20.02% Ca	Gammex
Cortical Bone	1.823	1.695	13.403	20.02	97.45	1.612	3.41% H, 31.41% C, 1.84% N, 36.50% O, 0.04% Cl, 26.81% Ca	Gammex
Water	1	1	7.7	14.32	75	1	11.19% H, 88.81% O	
PMMA	1.183	1.18	6.646	12.41	74	1.165	8.00% H, 60.00% C, 32.00% O	Polymers
Tecadur	1.463	1.41	6.857	13.15	77.8	1.315	3.61% H, 57.83% C, 38.55% O	Polymers
Tecaform	1.41	1.42	7.111	13.40	73.37	1.354	6.67% H, 40.00% C, 53.33% O	Polymers
Tecapeek	1.305	1.26	6.4	12.25	73.22	1.241	4.76% H, 76.19% C, 19.05% O	Polymers
Teflon	2.151	1.86	8.462	17.32	99.1	1.782	24.00% C, 76.00% F	Polymers
PVC	1.445	1.4	14.197	24.77	108.2	1.277	4.838% H, 38.436% C, 56.726% Cl	Polymers
Al	2.7	2.34	13	26.98	166	2.14	99.999%Al	Metals
Ti	4.54	3.76	22	47.87	233	3.254	99.6+% Ti	Metals
Fe	7.87	6.61	26	55.85	286	5.586	99.8+% Fe	Metals
Cu	8.96	7.37	29	63.55	322	6.118	99.99+% Cu	Metals
Mo	10.22	8.06	42	95.96	424	6.371	99.9% Mo	Metals
Sn	7.31	5.55	50	118.71	488	4.318	99.75% Sn	Metals
W	19.3	14	74	183.84	727	10.04	99.95% W	Metals
MCP-96	9.85	7.13	79.222	193.96	754	5.189	16% Sn, 32% Pb, 52% Bi	Metals

patients with a high number of single fields to improve dose conformity. Additionally, it can be used for mega voltage computed tomography (MVCT). In imaging mode an acceleration voltage of 3.5 MV is used. The mean energy of the resulting photon spectrum is 0.75 MeV [6]. The only a field of view of 390.86 mm which is equivalent to a pixel size of 0.76 mm is possible. CT numbers are stored on a 16 bit scale. The main purpose of this mode is to check the positioning of the patient. MVCT imaging can be utilized in the treatment planning process, too.

It has to be noted that this particular MVCT machine is affected by a design related issue: Because of the fact that the focus of the photon source and the focus of the detector are not identical, the outer detector bins are not correctly illuminated. This leads to a shift of the CT numbers in the isocenter of the image and a so called "zipper" or "button" artifact occurs. The problem was mitigated by shifting the position of the insert out of the isocenter. Another issue is that the CT numbers measured in the scanner are not constant but will experience a drift over time. This is due to decreasing energy of the beam caused by target wear. In this thesis this issue was not further considered because all samples were measured with MVCT in one single measurement.

3.2.3 Computation of Electron Density And Effective Atomic Number

It is possible to calculate the electron density and effective atomic numbers from two dual energy CT images. There are several methods to do so.

1. A method introduced by [3] basically parametrizes the two attenuation coefficients measured in the dual energy CT with the electron density and the effective atomic number. This approach uses polynomials in Z to parametrize photon cross sections. However, it neglects the binding of the electrons to their atoms. Because the cross sections are fitted with polynomials, discontinuities like K edges of the photoelectric cross section are not accounted for. Another disadvantage is that the energy spectrum of the x-ray tubes must be known. The exact spectra of the x-ray tubes are, however, usually not supplied with CT scanners and have to be measured or estimated.

2. A second, more empirical possibility is to calculate the electron density and effective atomic number with a method based on material decomposition. One may think of material decomposition as essentially a base vector transformation. The original system is the space set up by the two measured DECT numbers. The new coordinate system is defined by the vectors of two virtual base materials. Each of these base materials is thought of to be affected by exactly one attenuation mechanism: One material represents attenuation by the photo effect, the other one attenuation due to Compton scattering. The electron density can be calculated by a linear combination of the two material components. A calibration with a material of known electron density is necessary to calculate a mixing parameter for the linear combination. The effective atomic number can be calculated similarly. For a description of material decomposition see chapter 2.4 of [16]. This approach implicitly includes a correction for electron binding and seems to be more accurate than the aforementioned parametrization method [38].

The electron densities and effective atomic numbers of the measured materials were provided by Siemens through a strategic cooperation. The computation utilizes the described material decomposition method. The computation of electron density and effective atomic number using the method introduced by [3] was found to be less accurate than the base material decomposition in an earlier study [14].

The computed electron density and effective atomic number is ultimately used to estimate the WEPL. An alternative way to do so may be discriminant analysis, see 3.5.

3.3 Evaluation of The CT Measurements

Several software tools were used to evaluate the measured data.

1. The analysis of measurement results was mostly done with *R*, a free language optimized for statistical computing and visualization of multivariate data [26]. Several expansion packages were used to extend the functionality of the language. Medical imaging data are usually provided in the DICOM format. DICOM images were read into R with the the *oro.dicom* package. The plotting of data and results was done with the *lattice* and *latticeExtra* packages. Other packages were used for tasks not directly related to measurement evaluation. They will be introduced where appropriate.

2. *MITK 3M3* is a DICOM viewer developed at DKFZ. It was used to evaluate DICOM images qualitatively and to determinate certain parameters used in image analysis with R, e.g. image centers of the CT images.

3. *ImageJ* is a free software with many tools for image analysis. It is able to display a wide range of image formats and was used for image analysis if a more flexible tool was needed. It was especially useful to evaluate images in binary format.

3.4 Ion Beam Therapy

In this section the Heidelberg Ion Beam Therapy Center HIT will be shortly introduced. After that the measurement of ion ranges in material samples using the peak finder will be addressed.

3.4.1 Heidelberg Ion Beam Therapy Center HIT

The Heidelberg Ion Beam Therapy Center HIT offers treatment of malicious tumors with proton and heavy ion beams. The first patients were treated in November 2009. Until now more than 1000 have been treated, 600 of which alone in 2011. The facility features three treatment rooms. Two of those have a horizontal beam line, the third room is equipped with a gantry to rotate the beam tube around the patient. This enables to irradiate from additional directions allowing for more efficient treatment delivery. Tumors are irradiated with active spot scanning. This means that a pencil beam with a certain energy (i.e. at a certain depth in the tumor) deposits dose in a grid pattern across the lateral tumor profile. The maximal energy is 221 MeV for protons and 430 MeV/u for carbon ions [9].

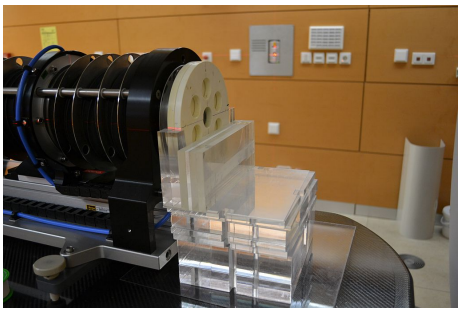

(a) The Peakfinder with a measurement sample in front of it.

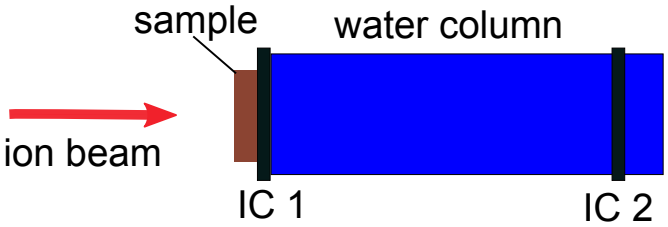

(b) Principal set up of the peak finder. A material sample is placed in front of the water column. The depth dose curve of an ion beam is measured with two ionization chambers. Chamber IC 1 is fixed at the proximal end of the column, the second chamber IC 2 can be moved through the water column.

Figure 3.6

3.4.2 Treatment of Patients With Metal Implants

Up to now patients with metal implants receive in general no additional imaging. One tries to avoid the sites of metal implants. Beam paths may be sent perpendicular to streaking artifacts in the assumption that uncertainties caused by incorrect CT numbers average out [15]. If it cannot be avoided to send the beam directly through a metal implant of high density with unknown true CT number that may cause range uncertainties, one assumes a CT number of the implant such that critical organs will under no circumstances receive too much dose. If e.g. a organ of risk is situated behind the tumor, one assigns a CT number to the implant that is rather too low than too high. This makes sure that dose is either deposited in the tumor if the assumed CT number was near the true CT number or in front of the tumor if the assumed CT number was too low. This allows to spare the organ at risk, but will lead to an underdosage of the target volume [10]. However, material identification or even a direct inclusion of high density materials in the treatment planning process would be desirable to achieve a higher dose conformality in such cases.

3.4.3 Ion Range Measurements With The Peakfinder

The stopping of ions in the materials presented in this chapter was determined by measuring the water equivalent path length (WEPL) of ions in these materials. All WEPLs were measured using a PTW Peakfinder (PTW Freiburg GmbH, Freiburg, Germany) which is in principle a water column with two ionization chambers. One of those chambers is at the front end, the other can be moved in axial direction through the water column. This setup allows to determine the ionization in the water at a certain axial position relative to the ionization at the entrance point. A curve proportional to a depth dose curve can so be measured. Figure 3.6b shows the experimental set up.

The actual determination of the WEPL is done in several steps. First, one must measure a reference curve without material slab in front of the water column. Then a depth dose curve with material slab is measured. It is crucial to choose an appropriate particle energy to make sure that the Bragg peak is situated in the water column for all measurements. This is especially important if large slabs of materials with high electron density are measured.

3.5 Discriminant Analysis

Discriminant analysis was applied in this thesis to investigate if the WEPL could be predicted from two DECT numbers. Quadratic discriminant analysis was performed as it was expected that the covariance matrices of the Gaussians describing the CT number distribution in the WEPL classes are not identical. All discriminant analysis studies in this thesis were done with R utilizing functions from the *MASS* package.

In this thesis, the WEPL of a tissue sample is predicted using discriminant analysis. The sample is a pig's head as described in 3.1. The learning data used in this study are 80 kV and 140 kV DECT numbers of the Gammex tissue equivalent materials and polymer samples introduced in 3.1.

A reference WEPL of the pig head was calculated for each voxel. The reference WEPL was obtained by using a standard 120 kV stoichiometric Hounsfield look-up table (HLUT) as it is currently used in treatment planning. The necessary 120 kV image of the pig head was scanned on a Siemens Somatom S4.

The applied discriminant analysis yields besides the WEPL classes a second kind of information: the posterior probabilities. They may be used to interpolate between the WEPL classes that are predicted for a sample voxel to make up for the fact that the predicted WEPL classes are discrete numbers rather than values from a continuous range.

4 Experiments And Results

This chapter presents the results of the conducted measurements. The main part deals with the estimation of ion ranges from CT numbers using HLUTs. It can be divided into three steps:

1. The measured CT numbers, electron densities and effective atomic numbers are shown and the achieved accuracy is presented in 4.1.
2. The results of the WEPL measurements are presented in 4.2.
3. The WEPL of the samples is estimated using HLUTs and compared to the measured values in 4.3. This part brings together the previous steps.

The remaining sections comprise the determination of insert diameters (4.4.1) and the assessment of the severity of artifacts in the material around the metal samples (4.4.2).

4.1 Evaluation of The CT Measurements

The mean CT numbers of all measured samples were computed. Only voxels within a 5 mm radius around the image center were considered to avoid partial volume effects at the edges of the samples. For the same reason 2–3 image slices at the axial ends of the samples were left out of the analysis. A radius of 5 mm is appropriate for the metal samples but quite small for the larger Gammex and polymer inserts. However, it was kept at 5 mm for consistency. The insert centers and axial ends were determined manually using MITK 3M3 1.1.0 and passed to a R script that calculated mean value and standard deviation.

4.1.1 DECT

In this thesis, spiral scans were used to measure CT numbers of the non-metal samples. The metal inserts were scanned with single rotations. One slice is enough to asses imaging quality and artifacts as the metal inserts are symmetrical in transversal direction and very homogeneous. Additionally, it is possible to compute reasonable mean CT numbers of the metal samples from just one slice because of the high image resolution and insert homogeneity.

The following protocols and reconstruction kernels were used in the Dual Energy measurements: Spiral scans were measured with the protocol
DE Abdomen LiverVNC, the pitch was 0.6 and the rotation time 1s. The single rotation scans were done with the protocol *Dual Energy Abdomen Sequence*. In all measurements of non-metal samples the reconstruction kernel was D30 and the field of view 300 mm which sets the pixel size in a 512x512 pixel image to 0.59 mm. The raw data of the metal samples was reconstructed with a pre-clinical reconstruction kernel using a 16 bit scale

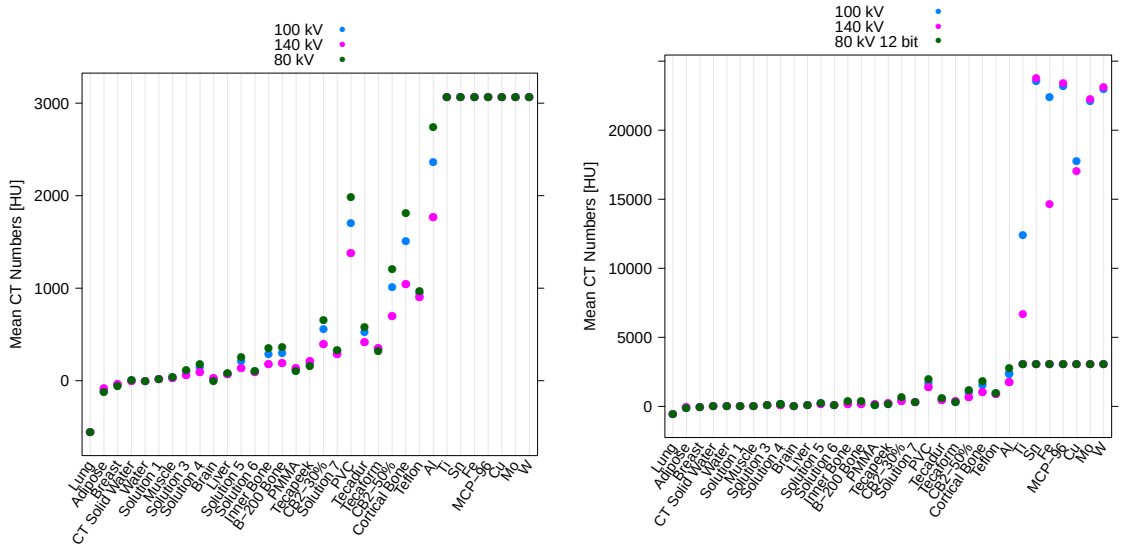

(a) CT numbers of all sample materials with 12 bit reconstruction.

(b) CT numbers with 12 bit and additional 16 bit reconstruction of the 100/140 kV measurement of the metal samples.

Figure 4.1

and including a raw data based DECT beam hardening correction[1] as described in 2.1.6. The field of view was 320 mm which yields a pixel size of 0.625 mm. The slice thickness was 2mm. For the spiral scans 500 mAs was used at first, but later it had to be reduced to 300 mAs to prevent overheating of the scanner. The single rotation scans of the metal samples were done with 650 mAs to increase photon statistics. All samples were measured with the voltage pairs 80/140Sn kV and 100/140Sn kV. The relative electron density and effective atomic number were provided by Siemens as described in 3.2.3.

The mean CT numbers of all measured materials reconstructed with 12 bit are shown in Figure 4.1a. It is clearly visible that the limit of the 12 bit scale is reached beyond aluminum. The materials are ordered by ascending electron density. Note the non-identical CT values at different voltages for non water-like materials. Figure 4.1b shows an additional 16 bit reconstruction of the metal samples measured with 100/140 kV. The CT values of all metals beyond aluminum are now well above the 12 bit scale's limit of 3071 HU. However, metals heavier than copper seem to have reached the measurement limit of the scanner. For molybdenum, tin, tungsten and MCP-96 the measured CT numbers are very similar and no information can be obtained.

Figure 4.2 shows the measured electron densities and effective atomic numbers of all sample materials compared to their reference values and underneath plots with the respective residuals. It can be noted that materials up to titanium are measurable in DECT with a precision of a few percent. PVC seems to be an exception to this observation. In 4.3 the results for materials up to titanium are plotted. For PVC, both electron density and effective atomic number show large deviations from the reference values. The effec-

[1]Provided and carried out by Siemens AG, Healthcare Sector, Forchheim, Germany.

tive atomic numbers of “Cortical Bone” and “Tecadur” are quite inaccurate as well. The effective atomic number of the “Lung” insert could not be determined. In 4.4 the focus is finally set on the metal samples. Figure 4.4a shows the relative electron density of the metal samples. Aluminum and titanium can be measured with deviations from the reference value of -2.54 % for aluminum and -7.12 % for titanium. Both results underestimate the reference values. It is clearly visible that the method does not work well for iron and copper, no correct results can be expected here.

The results of the effective atomic number calculations are similar. The results for aluminum and titanium are again close to the reference values. Aluminum shows a deviation of 4.76% and titanium a deviation of 5.05% from the reference. The results for iron and copper deviate significantly from the reference values like in case of the electron density measurements. No information can be obtained for all metals heavier than copper.

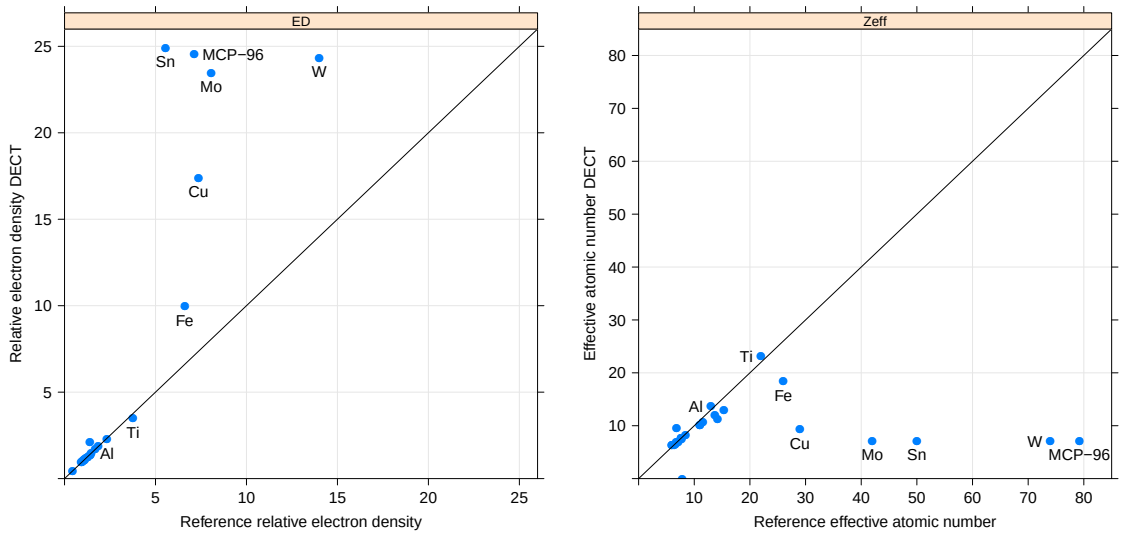

(a) Measured relative electron density over reference electron density. A black line indicates identity.

(b) Measured effective atomic number over reference effective atomic number. A black line indicates identity.

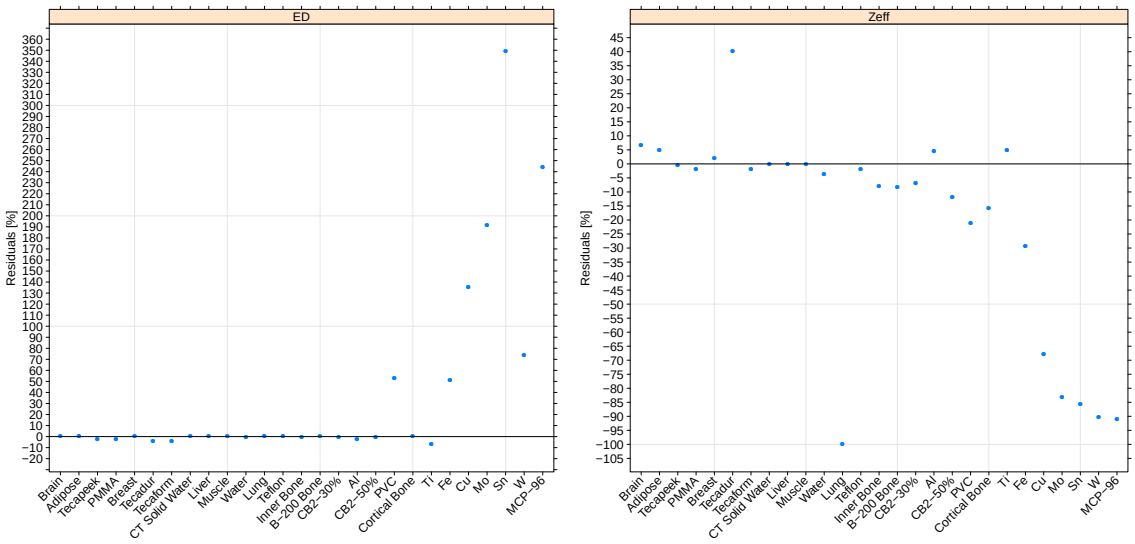

(c) Residuals of measured relative electron density and reference electron density.

(d) Residuals of measured effective atomic number and reference effective atomic number.

Figure 4.2

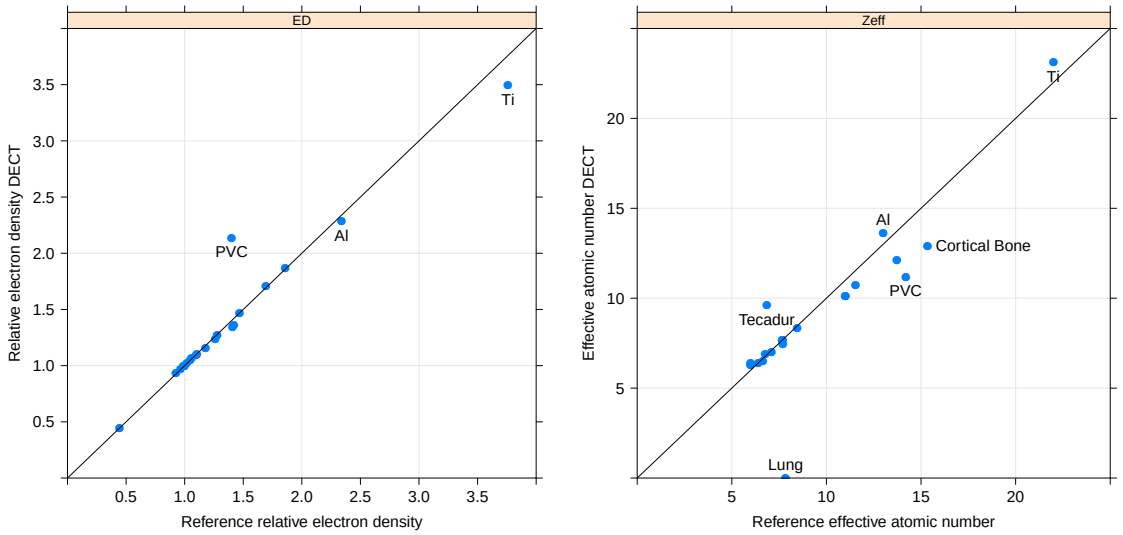

(a) Measured relative electron density over reference electron density for all materials up to titanium. A black line indicates identity.

(b) Measured effective atomic number over reference effective atomic number for all materials up to titanium. A black line indicates identity.

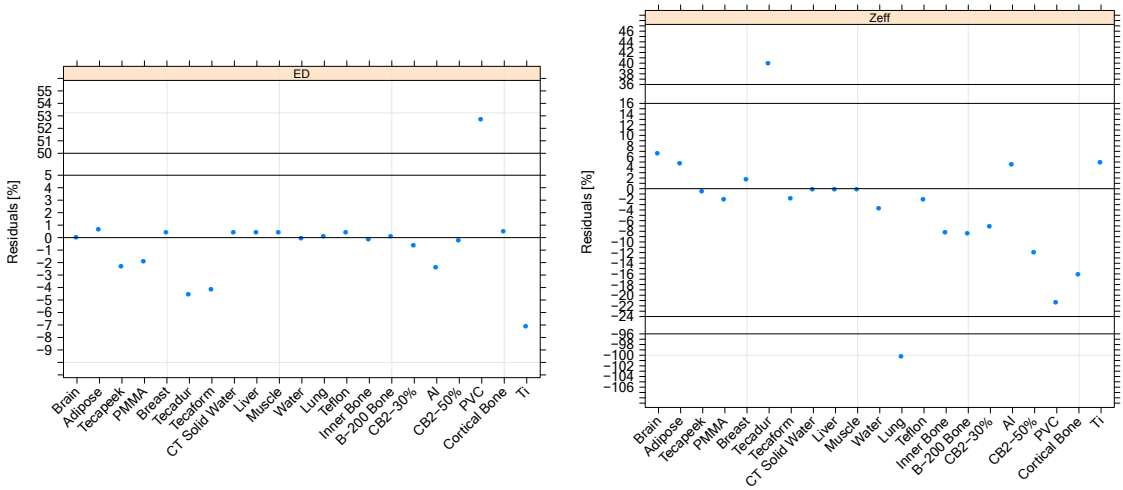

(c) Residuals of measured relative electron density and reference electron density.

(d) Residuals of measured effective atomic number and reference effective atomic number.

Figure 4.3

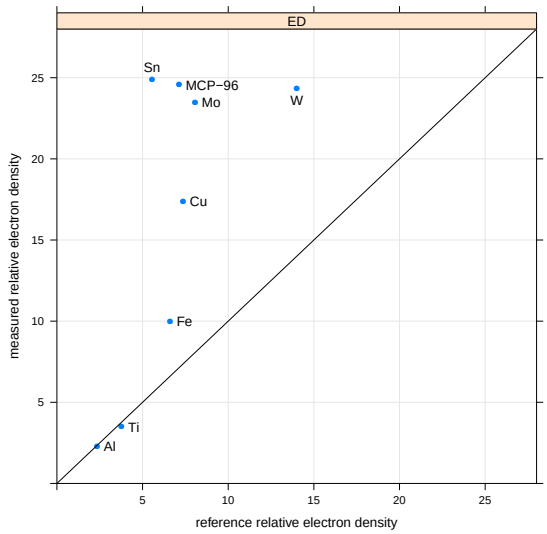

(a) Measured relative electron density of the metal samples over reference electron density. A black line indicates identity.

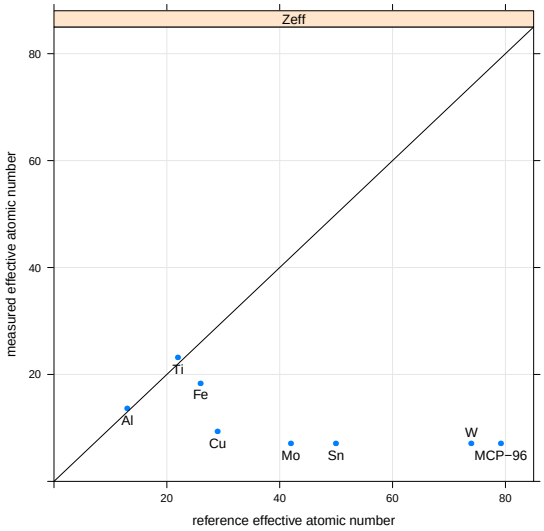

(b) Measured effective atomic number of the metal samples over reference effective atomic number. A black line indicates identity.

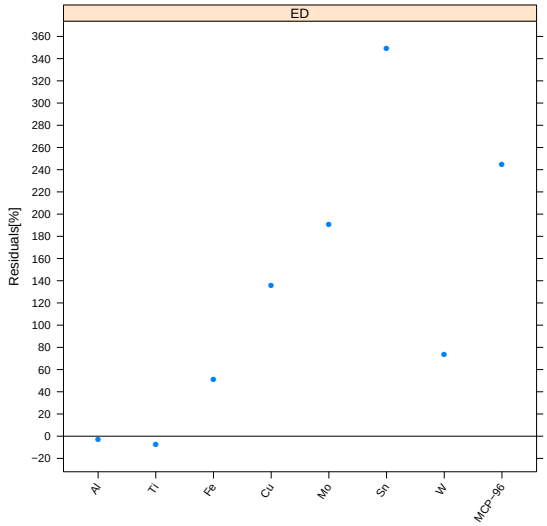

(c) Residuals of measured relative electron density and reference electron density of the metal samples.

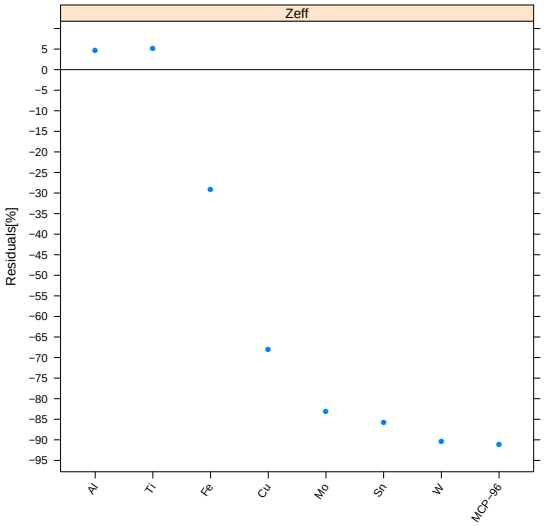

(d) Residuals of measured effective atomic number and reference effective atomic number of the metal samples.

Figure 4.4

4.1.2 MVCT

The metal samples were measured with MVCT. The field of view was 390.86 mm, the pixel size 0.76 mm. A slice thickness of 6 mm was choosen because of the considerably longer measurement time for finer slices. The voltage was set automatically to 3.5 MV.

Figure 4.5a shows the results of these measurements. It can be noted that in contrast to DECT all metals are measurable. However, one has to cope with much higher image noise. In 4.5b the relation between MVCT number and relative electron density is depicted. Since the photon cross section is a rather flat function of the atomic number in the energy range of MVCT, one would expect a linear relation between MVCT number and electron density in first approximation. This seems to be the case for pure sample materials. The alloy MCP-96, however, does not follow this trend.

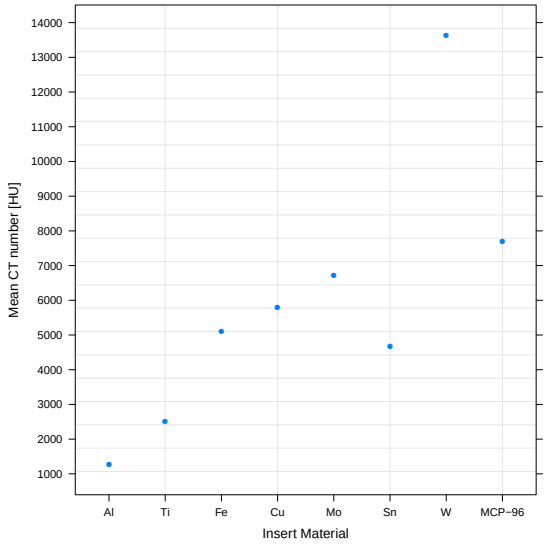

(a) CT numbers measured in MVCT.

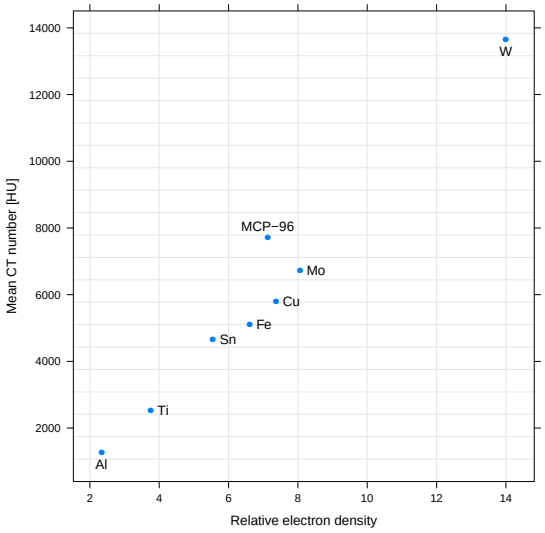

(b) MVCT numbers plotted over the relative electron density. Note how MCP-96 does not follow a linear MVCT number – electron density relation.

Figure 4.5

4.2 WEPL Measurements

The Peakfinder was sued to measure depth dose curves for the metal and polymer samples. To calculate the WEPL the depth at 90% maximum value of the distal end of the depth dose curve was used as range of the ions. The distal end of the curve was chosen because of it's sharp fall off which results in less ambiguity of the position. In this thesis C-12 with 270.55 MeV per nucleon was used for all measurements except for the Gammex tissue equivalent materials. These samples were irradiated with C-12 at 200 MeV per nucleon[2].

[2]Data provided by Benjamin Ackermann, HIT

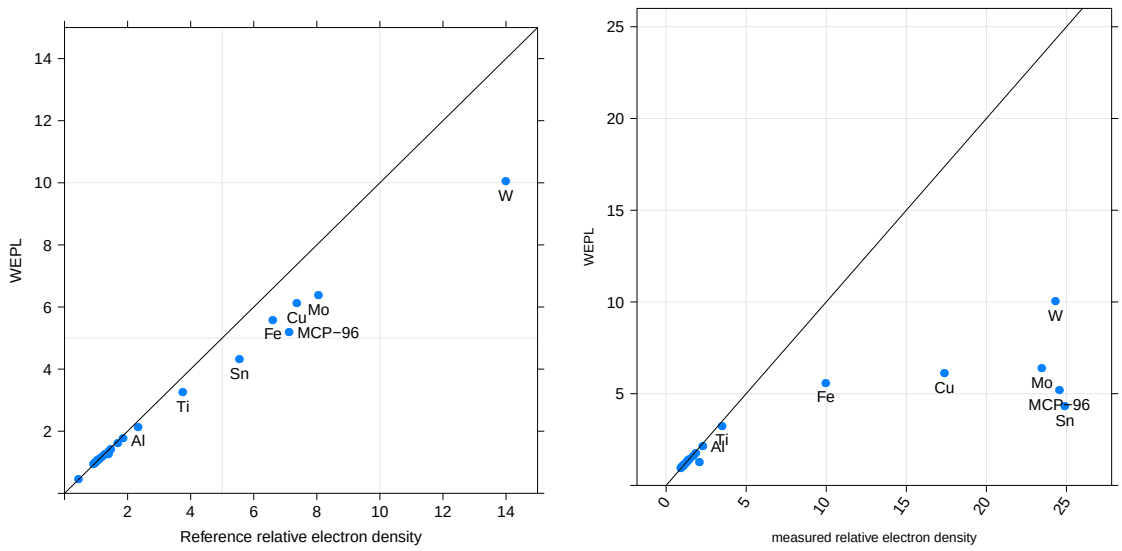

(a) WEPL over measured relative electron density of the metal samples.

(b) WEPL over measured relative electron density.

Figure 4.6

However, in both cases the slab is in the plateau region of the depth dose curve. Therefore, the difference in energy should not influence the results.

Table 4.1 gives an overview of the sample's WEPL. Figure 4.6a shows the measured WEPL plotted over the reference value of the relative electron density. Note the linear relation between electron density and WEPL for water-like materials and the deviations from linearity for samples with higher electron density like metals. This effect occurs because the effective ionization potential of these materials is significantly larger than that of water and thus the relative stopping power of these materials cannot be described accurately by the electron density alone. In figure 4.6b the WEPL is plotted over the electron density measured with DECT. The metal samples that could not be measured accurately are clustered on the right.

In Figure 4.7a only the WEPL of the metal samples is plotted over the reference value of the relative electron density. Again, it is clearly visible that a linear relation between electron density and WEPL cannot describe the measured WEPL precisely and that a correction is necessary. This figure is to demonstrate how the WEPL of the metal samples relates to the reference values of the relative electron density because the latter could only be calculated from DECT for aluminum and titanium. Figure 4.7b shows the WEPL of the metal samples plotted over the relative electron density measured with DECT.

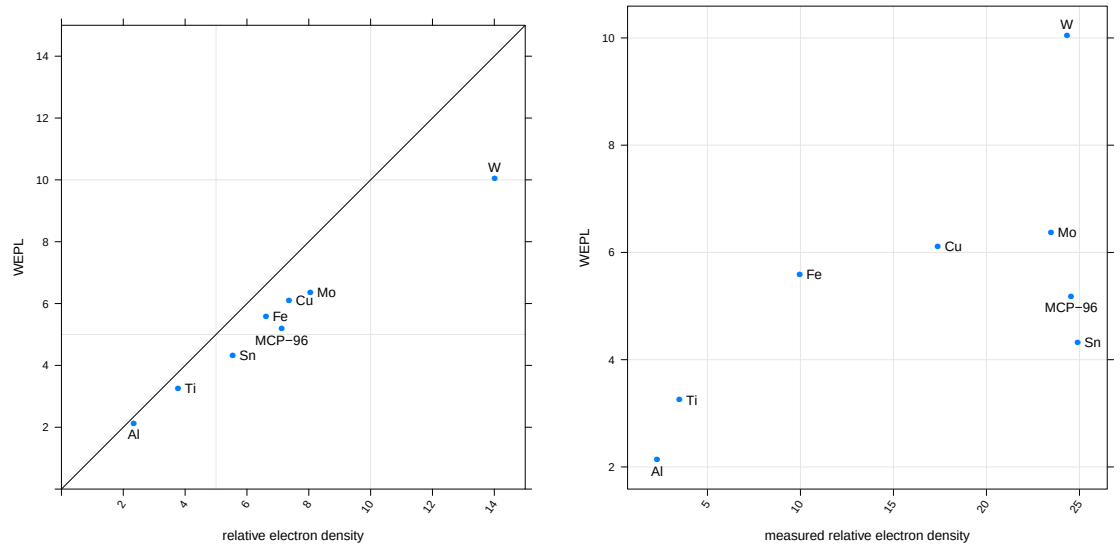

(a) WEPL over reference relative electron density of the metal samples.

(b) WEPL over measured relative electron density of the metal samples.

Figure 4.7

Table 4.1: Measured WEPL, particle type, particle energy of the WEPL measurement, reference relative electron density and effective atomic number of all sample materials.

Material	WEPL	Particle Type	Energy [MeV/u]	Relative Electron Density	Z_{eff}
Al	2.14	C12	270.55	2.34	13
Ti	3.254	C12	270.55	3.76	22
Fe	5.586	C12	270.55	6.61	26
Cu	6.118	C12	270.55	7.37	29
Mo	6.371	C12	270.55	8.06	42
Sn	4.318	C12	270.55	5.55	50
W	10.04	C12	270.55	14	74
MCP-96	5.189	C12	270.55	7.13	79.222
Tecadur	1.315	C12	270.55	1.41	6.857
Tecapeek	1.241	C12	270.55	1.26	6.4
Tecaform	1.354	C12	270.55	1.42	7.111
Teflon	1.782	C12	270.55	1.86	8.462
PVC	1.277	C12	270.55	1.4	14.197
Water	0.995	C12	270.55	1	7.7
Lung	0.444	C12	200	0.444	7.622
Adipose	0.943	C12	200	0.925	6.33
Breast	0.983	C12	200	0.965	6.938
CT Solid Water	1.001	C12	200	0.989	7.645
Muscle	1.033	C12	200	1.019	7.649
Brain	1.064	C12	200	1.048	6.238
Liver	1.073	C12	200	1.058	7.649
Inner Bone	1.099	C12	200	1.099	10.231
B-200 Bone	1.108	C12	200	1.105	10.234
CB2-30%	1.263	C12	200	1.278	10.685
CB2-50%	1.426	C12	200	1.47	12.307
Cortical Bone	1.612	C12	200	1.695	13.403
PMMA	1.165	C12	200	1.18	6.649

4.3 Hounsfield Look-Up Tables

4.3.1 DECT

The measured DECT values were related to the WEPL using the prototype HLUT described in 2.2.4. Figure 4.8 shows the results of this DECT to WEPL relation. The measured WEPL is plotted over the WEPL yielded by the HLUT. Almost all materials are very near to their reference values. The PVC sample is an exception and shows significant deviations between calculated and measured WEPL. Figure 4.9 compares the accuracy of the DECT HLUT to a standard 120 kV HLUT as described in 2.2. The results yielded by the DECT HLUT using electron density and effective atomic number are depicted in blue. The results from the 120 kV Hounsfield look up table (HLUT) are depicted in red. The necessary 120 kV CT scans of the samples were done with a Siemens Somaton 4 in case of the Gammex and Metal samples and with a Siemens Biograph 40 in case of the polymer and water samples. The field of view was 310mm, the reconstruction kernel H40s in both cases. The 120 kV CT data of the Gammex and polymer samples was provided by N. Hünemohr. The DECT method improves the WEPL estimation for water equivalent Gammex samples like the "brain" insert and polymers like PMMA where a huge improvement can be noted. These results are in agreement with earlier studies [14]. The WEPL of the "Lung" sample could not be estimated from the DECT measurements since it was not possible to calculate its effective atomic number. The precision of the WEPL estimations for aluminum and titanium increased notably, especially for titanium. The accuracy of the WEPL of aluminum could be increased from -11.46 % to 4.88 %. For titanium the accuracy increased from -36.41 % to 2.75 %. It has to be said, however, that the superior result of DECT for titanium is at least in part due to the fact that titanium cannot be measured properly on the 12 bit scale of the 120 kV images.

Figure 4.10 shows the influence of the atomic number fit in 2.14 by plotting the deviations between the WEPL predicted with electron density and effective atomic number and the WEPL predicted using only the electron density. The difference in WEPL is at most 2% for tissue-like materials and up to 4% for metals. For metals heavier than titanium, one would expect an even greater difference.

Table 4.2: Residuals in percent of WEPL calculated from DECT and 120 kV HLUT.

Material	Residuals WEPL from DECT [%]	Residuals WEPL from 120 kV HLUT [%]
Brain	0.460	-5.668[a]
Adipose	0.720	-0.699[a]
Tecapeek	1.178	-10.710[b]
PMMA	1.169	-6.599[a]
Breast	0.154	-0.250[a]
Tecadur	2.341	-5.158[b]
Tecaform	2.059	-13.230[b]
CT Solid Water	0.308	-0.165[a]
Liver	0.070	-0.713[a]
Muscle	0.116	-0.683[a]
Water	1.662	0.395[b]
Lung	Inf	-5.492[a]
Teflon	5.566	-19.301[b]
Inner Bone	-0.418	3.385[a]
B-200 Bone	-0.426	2.929[a]
CB2-30%	-0.030	-1.028[a]
Al	4.879	-11.464[a]
CB2-50%	1.656	0.631[a]
PVC	66.102	35.113[b]
Cortical Bone	4.120	1.390[a]
Ti	2.748	-36.409[a]

a Siemens Somatom S4
b Siemens Biograph 40

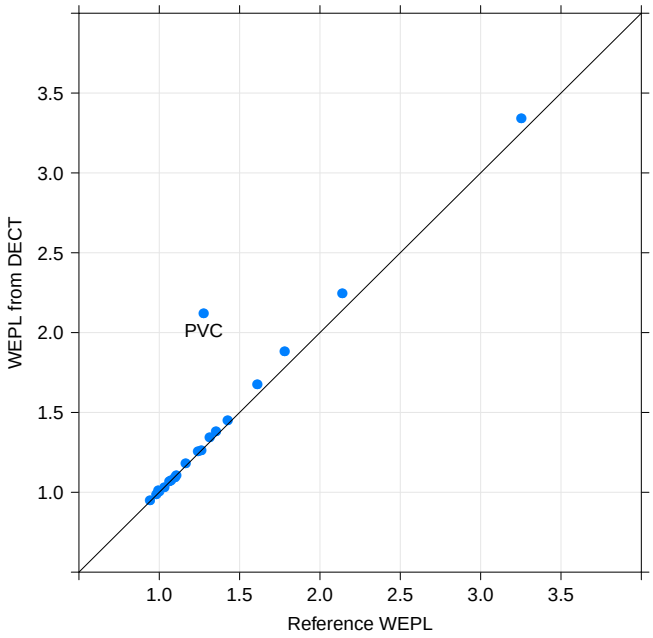

Figure 4.8: Reference WEPL over WEPL calculated from measured relative electron density and effective atomic number.

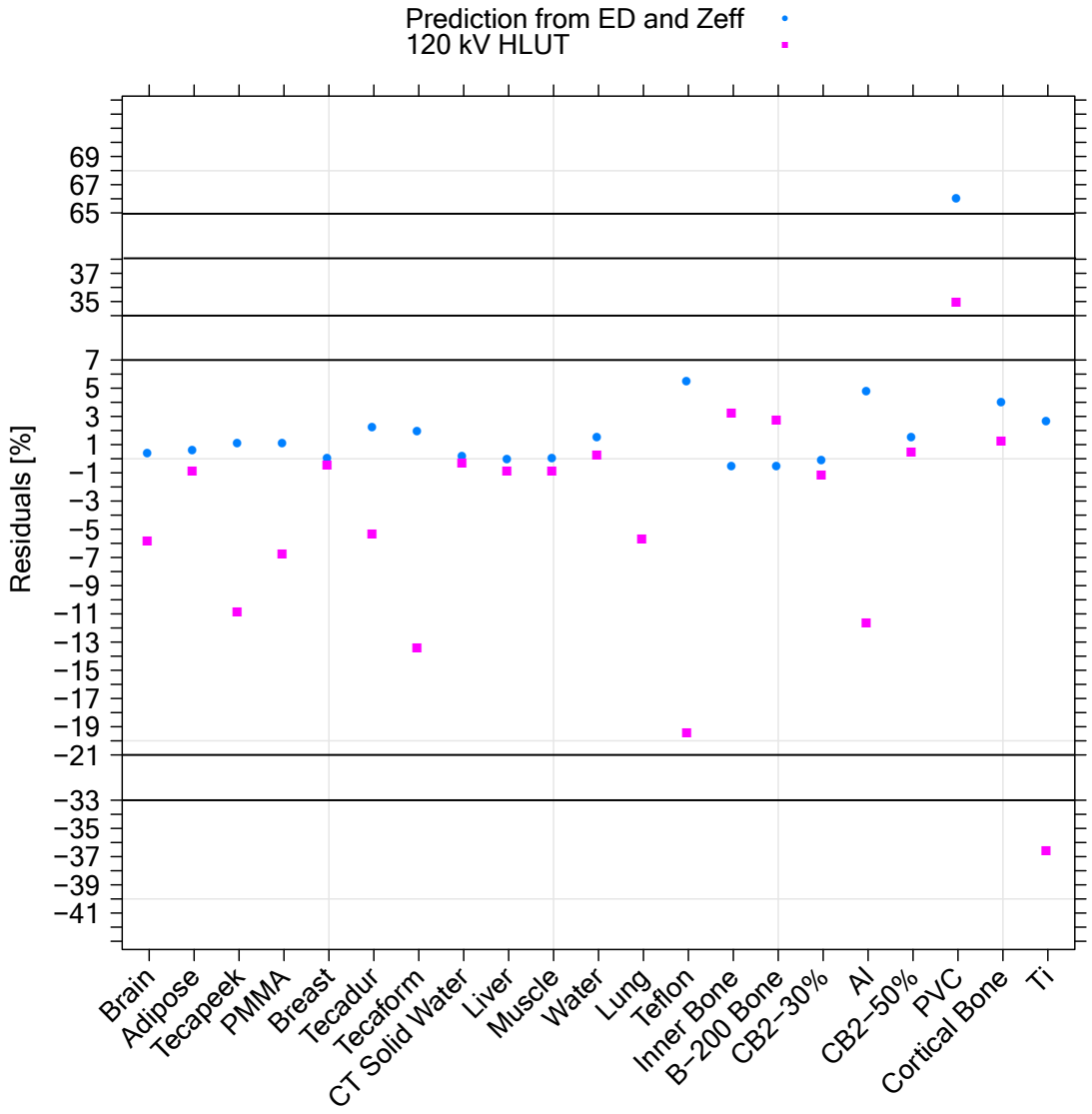

Figure 4.9: Comparison of the residuals of WEPL calculated from DECT and WEPL from a standard 120 kV HLUT.

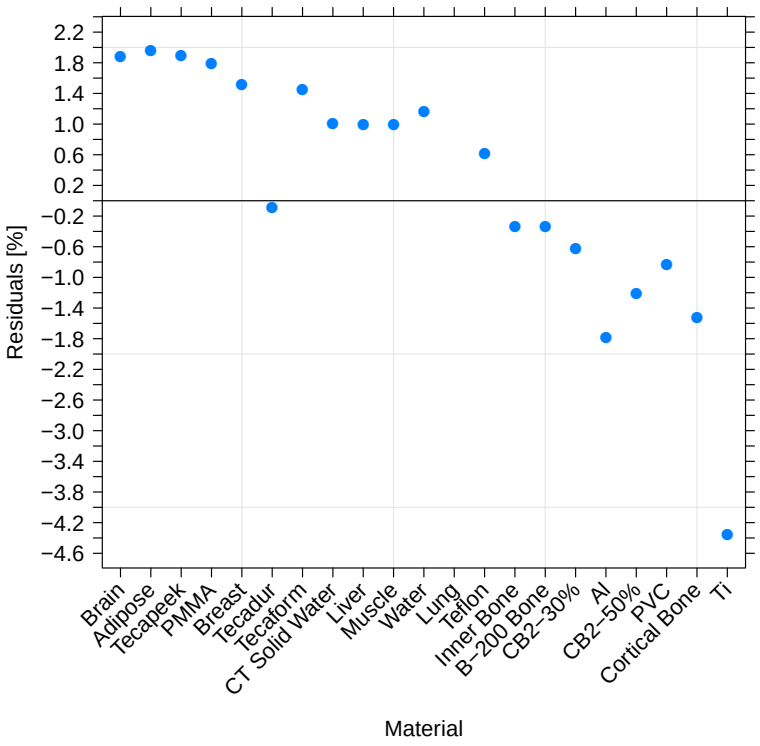

Figure 4.10: Residuals between WEPL calculated from relative electron density alone and WEPL calculated from relative electron density and effective atomic number.

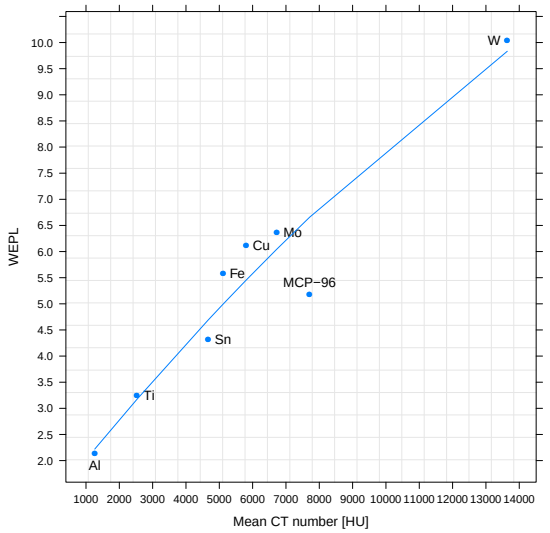

(a) WEPL over MVCT number fit with quadratic polynomial. Adjusted R^2: 0.9442.

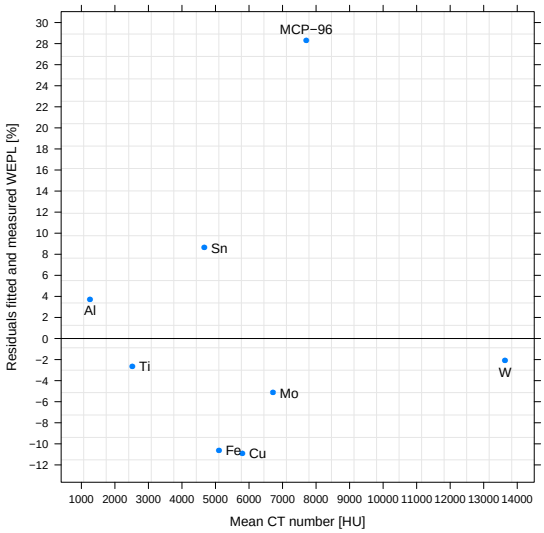

(b) Residuals of measured WEPL and WEPL from fit of MVCT numbers.

Figure 4.11

4.3.2 MVCT

The MVCT and WEPL data were fit with a quadratic polynomial to obtain a function that relates the MVCT numbers to the WEPL as at present there is no clinically established HLUT. Figure 4.11a shows the fit. The residuals between measured WEPL of the samples and the WEPL predicted by the fit are displayed in figure 4.11b. The WEPL of the pure metal samples can be predicted with 10% accuracy or better. The predicted WEPL of MCP-96, the only alloy in the set, shows a much larger deviation from the measured value.

A preliminary MVCT HLUT established at HIT [33] was alternatively used to obtain the WEPL. However, the HLUT only covers MVCT numbers up to 3096 HU and was therefore linearly extrapolated to 14000 HU. The results are shown for all materials in 4.12a and for materials up to titanium in 4.12b. The MVCT data of non-metal samples were measured and provided by N. Hünemohr. For the non-metal samples and metals up to titanium, high accuracy was achieved. The HLUT's accuracy is, however, not stable for heavier metals as high deviations from the reference WEPL can be observed for molybdenum, tin, tungsten and MCP-96.

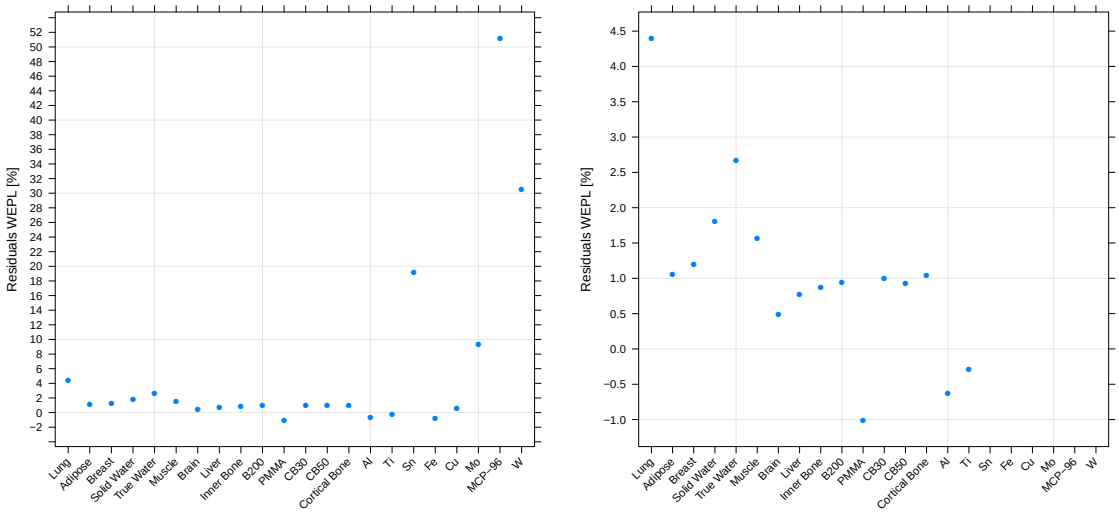

(a) Residuals of measured WEPL and WEPL from HLUT of MVCT numbers.

(b) Residuals of measured WEPL and WEPL from HLUT up to titanium.

Figure 4.12

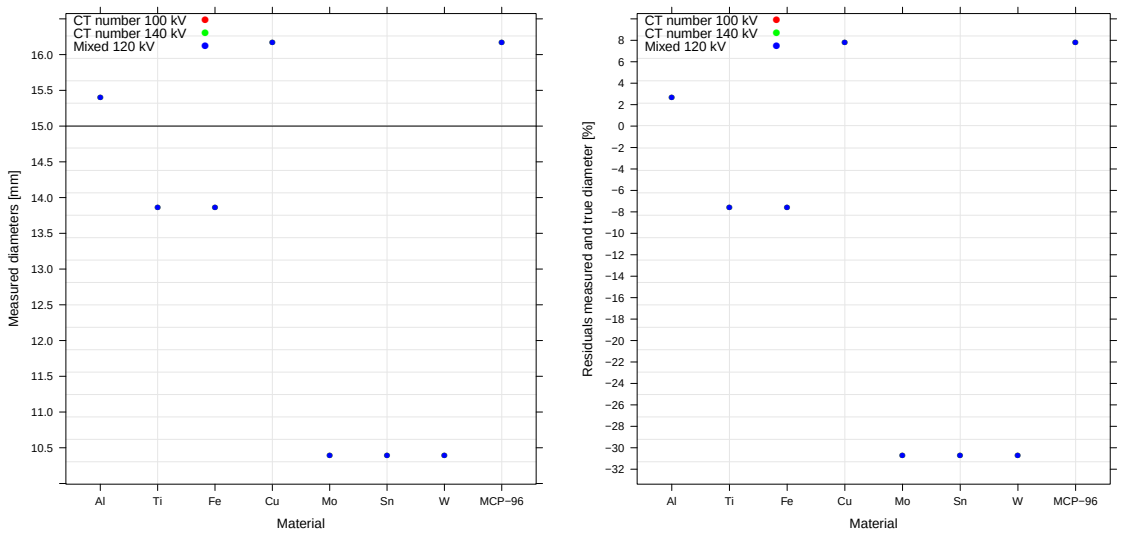

(a) Insert diameters calculated from 12 bit DECT data. The data points of all three contrasts lie on top of each other.

(b) Residuals between insert diameters calculated from 12 bit DECT data and true diameters.

Figure 4.13

4.4 Artifacts due to High Z Materials

Imaging artifacts due to the high attenuation of the metal samples were investigated. A focus was set on insert diameter and (stripe) artifacts in the material surrounding the inserts.

4.4.1 Insert Geometry

The insert diameters of the metal samples were estimated using images on a 12 bit as well as a 16 bit CT scale. The diameters were determined automatically using a R script. Voxels on a line through the insert center were considered to estimate the insert's diameter. The image positions were the gradient of th CT values were steepest was considered as the edges of an insert. This method is roughly equivalent to windowing the image to FWHM to determine the insert geometry. In practice, the absolute value of the voxel-wise differences of the CT values were used to find the steepest gradient. This approach sounds unstable at first but turned out to be rather reliable.

Figure 4.13a shows the resulting diameters if the 12 bit data is used. A black line indicates the true insert diameter. In figure 4.13b the residuals between true diameter and calculated diameter in percent are shown. The deviations from the true value are quite high, especially for the heavier metals. It is clearly visible that the insert diameters cannot be estimated very precisely using the 12 bit images.

The results that can be obtained if the 16 bit images are used to estimate the image diameters are shown in Figure 4.14a. The corresponding residuals are plotted in figure4.14b. Again the true insert diameter is marked by a black line. The results for the 140 kV

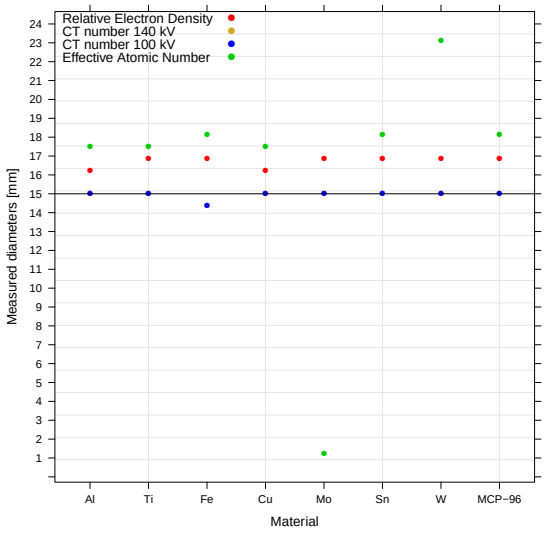

(a) Insert diameters calculated from 16 bit DECT data.

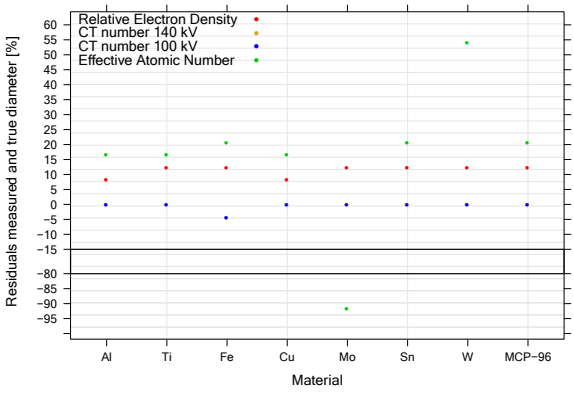

(b) Residuals between insert diameters calculated from 16 bit DECT data and true diameters.

Figure 4.14

and the 100 kV images are identical and almost perfectly agree with the true diameters. The resulting diameter estimations one obtains if the relative electron density or effective atomic number images are used are less precise and show in general a overestimation of the insert diameters.

MVCT images are the third data set that was used to calculate the insert diameters. Figure 4.15a and figure 4.15b show the estimated diameters and the residuals in percent. The true diameter in figure 4.15a is as always marked by a black line. The insert diameters can be estimated for all but the copper insert with a precision of at least 2%.

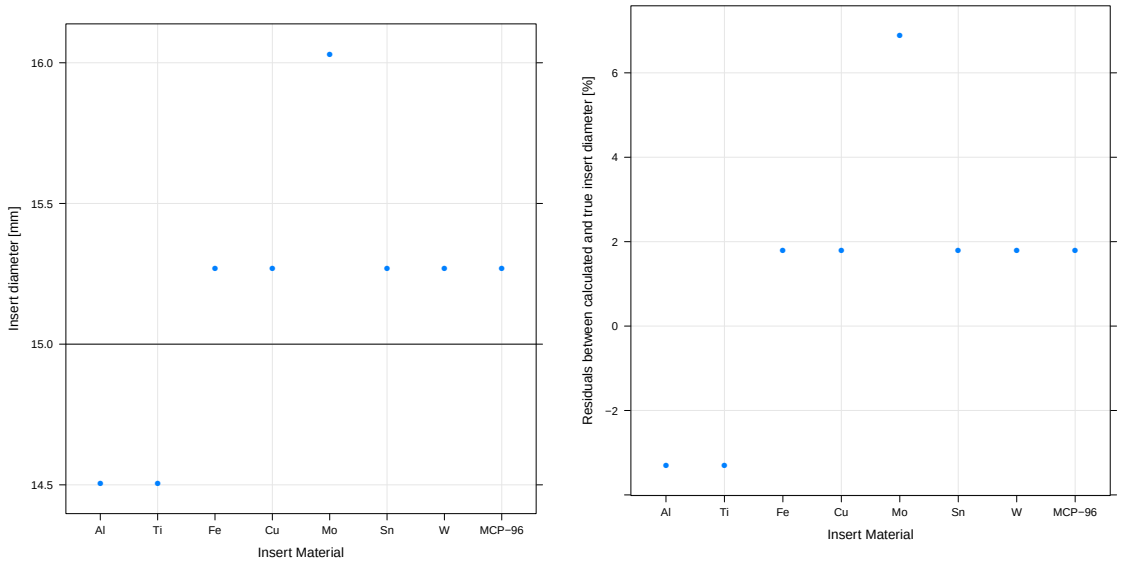

(a) Insert diameters calculated from MVCT data.

(b) Difference between insert diameters calculated from MVCT data and true insert diameters.

Figure 4.15

4.4.2 Artifacts in The Surrounding Material

The artifacts in the PMMA around the metal inserts were assessed by considering the CT values on a circle with a radius of 70 pixels around the insert center. This allows to investigate the severeness of streaking artifacts which reach radially from the insert into the surrounding material. To make the images easier to compare, the scales were converted to the scale of the relative electron density images. This was done by using a linear function to translate between electron density and the other contrasts. A linear function has two parameters and can therefore be defined by two data points. As first point the value of PMMA was used. The second point is given by the assumption that a relative electron density of 1 corresponds to a CT number of 0 HU and a relative electron density of 0 corresponds to an effective atomic number of 0. This kind of conversion is in general not valid if arbitrary materials are compared because the electron density is not necessarily a unique function of the atomic number. Here it is used to compare fluctuations in only one material, namely PMMA, which should avoid this dilemma. The effects of image noise that are present even without artifacts were reduced by smoothening the values with a running median smoothing filter from the *stats* package in R. A smoothing window of 11 bins was used.

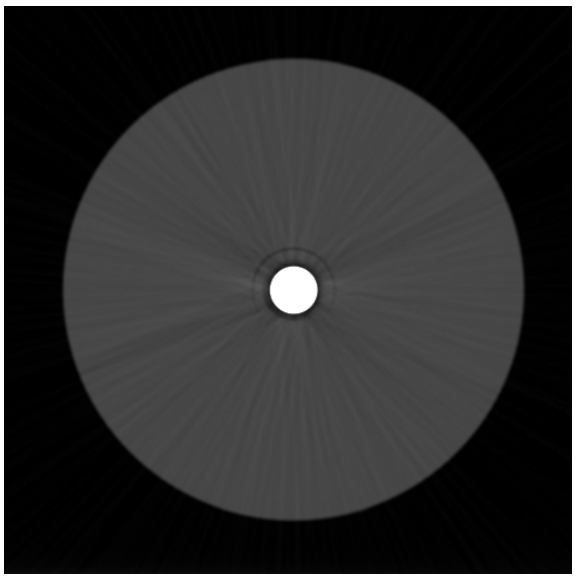

Figure 4.16: Artifacts in PMMA in a 140 kV image of the tungsten sample.

Figure 4.17a and figure 4.17b show the values of PMMA in the 100 kV and 140 kV CT images on a circle around all metal samples. The CT numbers are plotted over the angle between voxel position, insert center and horizontal image axis. For aluminum and titanium the artifacts are rather moderate and can hardly be distinguished from image noise. For more dense materials, however, significant artifact peaks can be observed. The artifacts in the 140 kV images are less pronounced than in the 100 kV images because the photon spectrum is harder due to higher voltage and additional tin filtration.

In 4.18a and 4.18b the results for the electron density and effective atomic number images are given. It can be noted that the artifacts in the electron density images are almost identical to the 100 kV and 140 kV images. The image values of PMMA in the

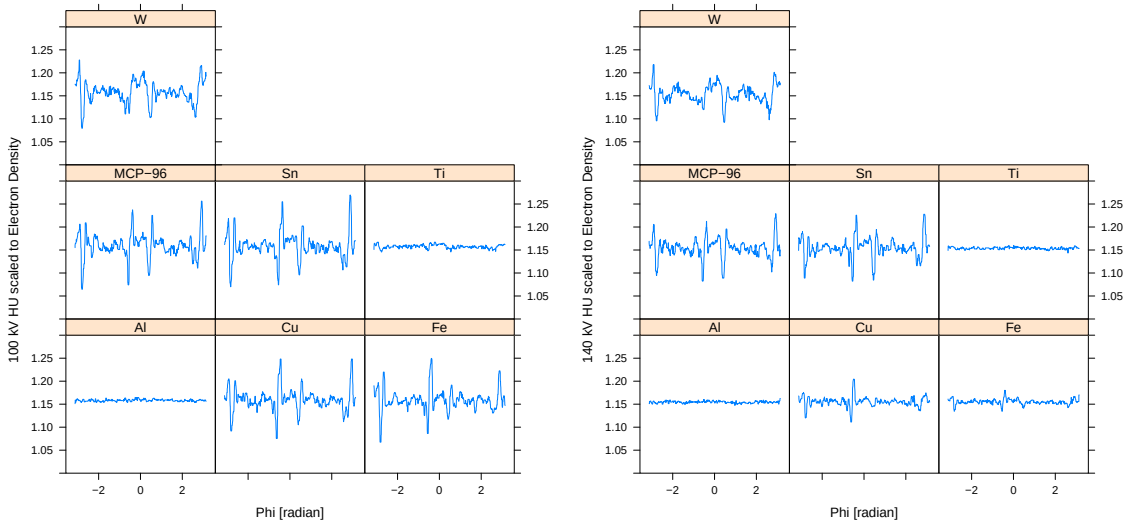

(a) Artifacts on a circle line around the metal sample in the 100 kV CT image converted to relative electron density scale.

(b) Artifacts on a circle line around the metal sample in 140 kV CT image converted to relative electron density scale.

Figure 4.17

effective atomic number images, however, show significantly larger artifacts than the other image modalities. In conclusion, it can be noted that relative electron density and effective atomic number images do not seem to be less affected by metal induced artifacts.

Figure 4.19 shows the standard deviations of the CT values on the circle around the insert. It is clearly visible that the standard deviations in the 100 kV, 140 kV and electron density data are very similar. Only the values of the effective atomic number image show much higher standard deviations due to significantly more pronounced artifacts.

Figure 4.20a shows the MVCT values on a circle around the inserts. In figure 4.20b the standard deviations of the CT numbers on the circle around the inserts are depicted. Artifacts in the PMMA are hardly visible, only image noise can be observed. All CT values lie in a very narrow range. No significant increase for metals with high atomic number can be noticed.

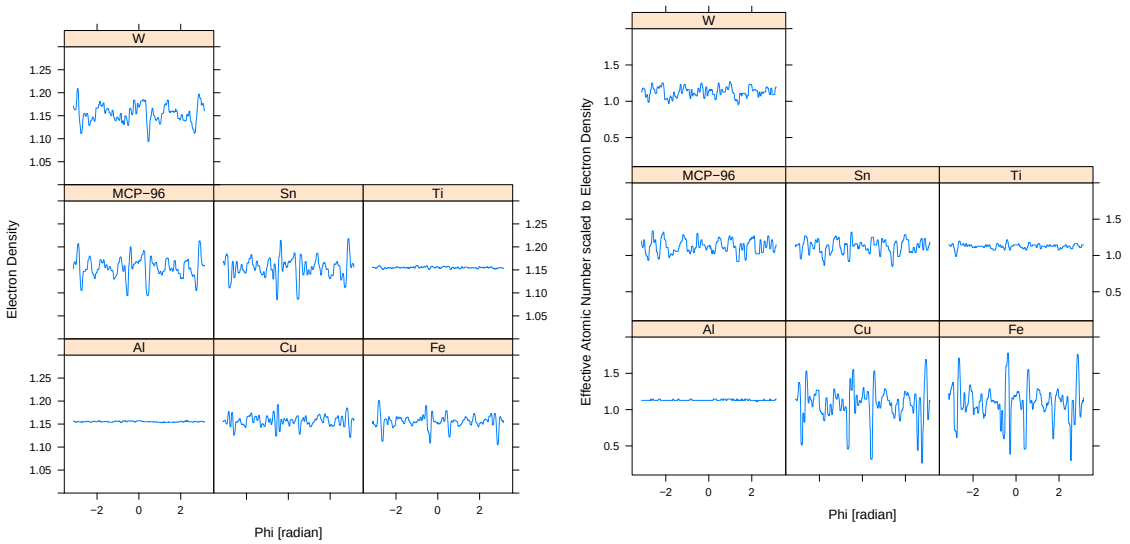

(a) Artifacts on a circle line around the metal sample in the relative electron density image.

(b) Artifacts on a circle line around the metal sample in the effective atomic number image converted to relative electron density scale.

Figure 4.18

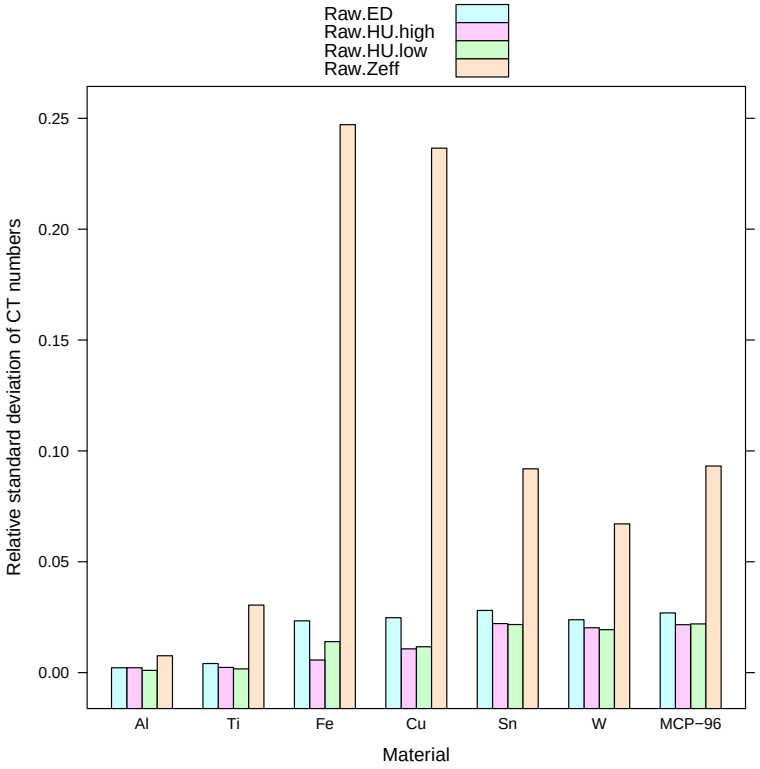

Figure 4.19: Standard deviation of kV CT values on circle line around metal samples.

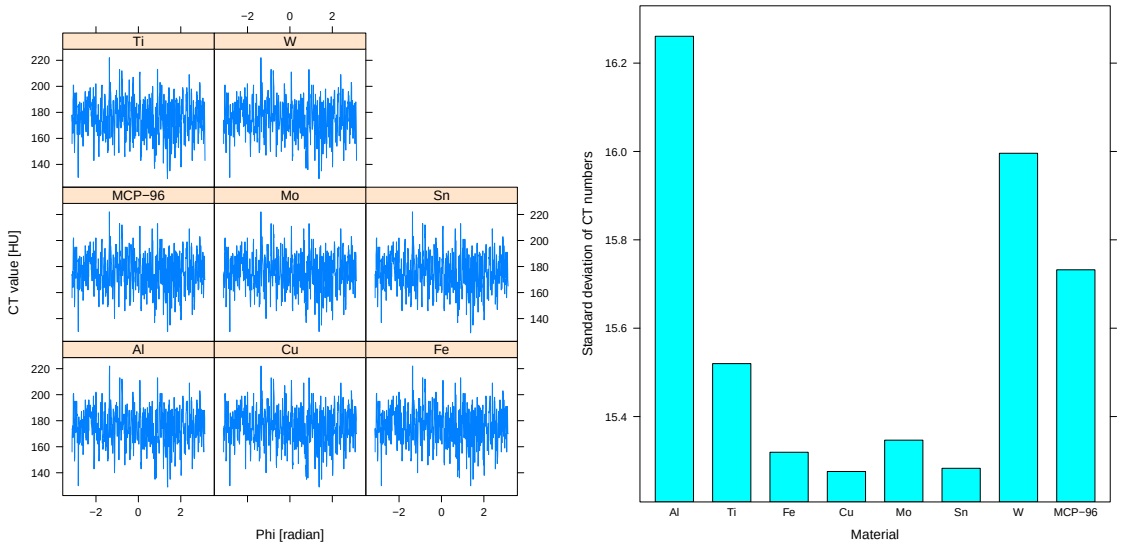

(a) MVCT values on a circle around the metal samples. No significant difference of artifact intensity can be noticed.

(b) Standard deviation of the CT values measured with MVCT on a circle around the inserts.

Figure 4.20

Figure 4.21: An overview of the mean values, standard deviations and min. and max. values of the CT numbers around the inserts converted to the electron density scale ("relative") and in absolute numbers.

Material	Mode	Relative Maximum	Relative Minimum	Relative Mean	Relative Standard Deviation	Absolute Maximum	Absolute Minimum	Absolute Mean	Absolute Standard Deviation
Al	100 kV	1.165	1.151	1.158	0.002	122	112	117.349	1.629
Cu	100 kV	1.248	1.076	1.159	0.025	184	56	118.097	18.372
Fe	100 kV	1.250	1.067	1.159	0.023	185	50	117.647	17.321
MCP-96	100 kV	1.256	1.065	1.159	0.027	190	48	118.045	19.972
Sn	100 kV	1.270	1.070	1.159	0.028	200	52	117.516	20.799
Ti	100 kV	1.167	1.146	1.157	0.004	124	108	116.762	3.051
W	100 kV	1.228	1.080	1.158	0.024	169	59	116.821	17.689
Al	140 kV	1.162	1.148	1.154	0.002	146	133	138.864	1.982
Cu	140 kV	1.205	1.111	1.155	0.011	184	100	139.733	9.651
Fe	140 kV	1.180	1.135	1.155	0.006	162	121	139.541	5.116
MCP-96	140 kV	1.229	1.082	1.154	0.022	206	74	138.259	19.450
Sn	140 kV	1.228	1.082	1.154	0.022	205	74	138.835	19.899
Ti	140 kV	1.160	1.143	1.154	0.002	144	129	138.327	2.117
W	140 kV	1.218	1.092	1.154	0.020	196	83	138.221	18.211
Al	ED	1.157	1.153	1.155	0.001	1.157	1.153	1.155	0.001
Cu	ED	1.192	1.121	1.157	0.012	1.192	1.121	1.157	0.012
Fe	ED	1.201	1.105	1.156	0.014	1.201	1.105	1.156	0.014
MCP-96	ED	1.213	1.094	1.155	0.022	1.213	1.094	1.155	0.022
Sn	ED	1.218	1.085	1.155	0.022	1.218	1.085	1.155	0.022
Ti	ED	1.160	1.151	1.155	0.002	1.160	1.151	1.155	0.002
W	ED	1.209	1.094	1.155	0.019	1.209	1.094	1.155	0.019
Al	Zeff	1.145	1.110	1.131	0.008	6.500	6.300	6.421	0.043
Cu	Zeff	1.691	0.264	1.078	0.237	9.600	1.500	6.122	1.343
Fe	Zeff	1.779	0.299	1.095	0.247	10.100	1.700	6.219	1.403
MCP-96	Zeff	1.339	0.916	1.124	0.093	7.600	5.200	6.381	0.529
Sn	Zeff	1.321	0.845	1.123	0.092	7.500	4.800	6.374	0.522
Ti	Zeff	1.215	0.986	1.127	0.030	6.900	5.600	6.396	0.173
W	Zeff	1.268	0.951	1.127	0.067	7.200	5.400	6.399	0.381

5 Discussion

In this chapter the results of the conducted experiments and analyses are discussed. An outlook suggesting further experiments and topics that may be worth investigating is given.

5.1 CT Measurements

5.1.1 DECT Measurements

The results showed that only aluminum can be measured properly with 12 bit reconstruction as the CT values of more dense metals are beyond the upper limit of the 12 bit scale. Therefore, the CT data of the metal samples was reconstructed on a 16 bit scale. The results suggest that the electron density and effective atomic number of metals can be determined reliably up to $Z = 22$. The computed electron density and effective atomic number of the sample with the next higher atomic number, iron, already showed huge deviations from the reference values. This behavior was observed for iron and copper. Thus, $26 \leq Z \leq 29$ sets the limits of a regime where large large deviations from the reference values may be observed and no precise measurements seem to be possible. For atomic numbers $Z \geq 42$ the measurements yielded similar results for all materials. In this third regime a "saturation" of CT numbers seems to set in where no information can be obtained. The reasons for the deviations from the reference values and eventual saturation are most likely photon starvation in the detectors and cross scattering between detectors [18]. Therefore, a reliable measurement of metals in kilo voltage CT seems to be possible up to titanium. However, due to the fact that there are huge gaps between the atomic numbers of the metal samples, it cannot be determined precisely for which materials the deviations from the reference values become significant, where saturation sets in and if there are materials that do not follow the described trends. Therefore, the limits of the described material regimes should be regarded as rather qualitative. Moreover, it would be interesting to study if alloys conform to the observed regimes or if the regimes' limits would be shifted.

Nevertheless, DECT combined with the use of a 16 bit CT scale may be employable for patients with implants made from light metals. This is insofar satisfactory as especially titanium is a common implant material.

5.1.2 MVCT Measurements

All metal samples could be measured with MVCT without noticeable saturation of CT numbers as observed in DECT for materials with high atomic number. Image noise was higher than in the kV CT images. In addition, pixel size and slice thickness are more coarse than in the DECT images as the scanner used for the MVCT measurements does not allow to vary the pixel size. The slice thickness can be chosen between 2, 4 an 6 mm; however, the scanning time increases anti-proportionally to the slice thickness. Therefore,

the slice thickness was set to 6 mm. These limitations are due to technical properties of the Tomotherapy device, which is rather a linear accelerator with full axial angle coverage and additional imaging features than a full-fledged CT scanner. Nevertheless, the obtained results recommend MVCT for cases where the presence of implants composed of very dense materials is expected. The absence of pronounced streaking artifacts as shown in 4.20a and 4.20b makes it even more interesting. The drawback would be increased dose in comparison to kilo voltage CT. However, implants are in many cases attached to bone structures, which are rather static. One single MVCT scan to evaluate implants might therefore be sufficient for the whole treatment. This would limit the amount of additional dose. A risk-benefit assessment might therefore in certain, complicated cases favor MVCT.

5.2 Hounsfield Look-Up Tables

5.2.1 DECT

The WEPL of all materials up to Titanium was calculated using the DECT HLUT introduced in 2.2.4. The WEPL of these samples could be determined with accuracy of 5% or better except for the PVC sample. An accuracy of 4% or better was achieved for the tissue equivalent Gammex materials. For the Gammex samples modeling soft tissues the accuracy was below 1 % except for the "Lung" sample where no effective atomic number was available and thus no WEPL could be computed. The WEPL estimation of the Gammex bone samples could be improved as well except for " CB2-50%" and "Cortical Bone". These samples are the Gammex samples with the highest electron densities and are composed of more than 20% calcium. There may be an impact of the high calcium content on the DECT algorithm, but this is just a conjecture. The accuracy of the WEPL results of the polymer samples could be increased in comparison to the 120 kV HLUT. For all polymers except for PVC an accuracy of 5.5 % or better was achieved. For example, the accuracy of the WEPL of Teflon could be improved from -19.3% to 5.6% and the accuracy for Tecaform from -13.2% to 2.1%. The exact reason for the huge deviation from the reference WEPL of PVC is probably related to the elemental composition of the material which contains over 50% of chlorine[1]. However, it has to be acknowledged that the DECT result for PVC is significantly worse than the result obtained from the 120 kV scan. The WEPL estimation for the aluminum and titanium samples could be improved dramatically in comparison to the results obtained from the 120 kV HLUT. Aluminum was improved from -11.5% to 4.9% and titanium from -36.4% to 2.7%. Similar to the measurement of DECT numbers, it would be interesting to see how precise the WEPL of alloys can be estimated. This point is of course closely related to the accuracy of DECT measurements of alloys. The fact that the WEPL of titanium can be obtained is of high relevance since the material is often used in implants due to it's high biocompatibility.

Figure 5.1a shows the influence of the Z_{eff} term in equation 2.14 on the WEPL. As described in 2.14, the correction essentially fits the logarithm of the mean excitation potential that occurs in the Bethe formula with a linear function of $ln(Z_{eff})$. It has to be noted that the fit seems to lead to an overestimation of the WEPL for water equivalent materials. For

[1]Though it should not be related to edges in the photo effect cross section as the K-edge of chlorine is at $\tilde{1}7$ keV.

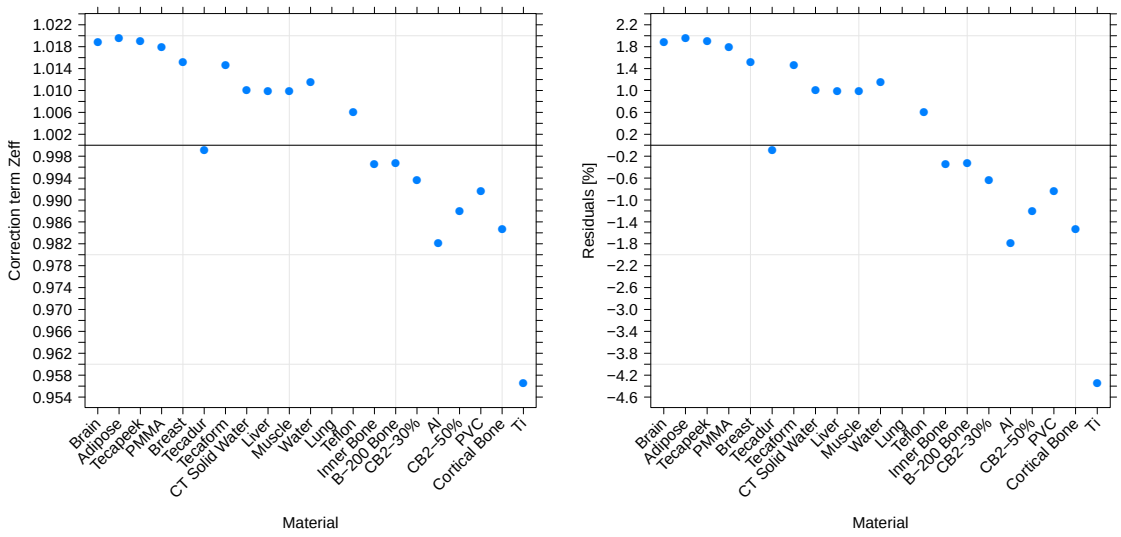

(a) The influence of the Z_{eff} correction term on the WEPL.

(b) Correction of the WEPL by the Z_{eff} term in percent.

Figure 5.1

water, the correction factor should be 1 since in this case the relative stopping power is exactly the relative electron density due to the normalization to the value of water. For dense materials like bone and metals the correction factor decreases the WEPL estimation which is consistent with the observed overestimation of the WEPL if it is estimated by the relative electron density alone (see 4.7a).

The correction introduced by the fit of $ln(Z_{eff})$ may be biased to a certain degree. It was determined by fitting the logarithm of the effective atomic numbers $ln(Z_{eff})$ of the Gammex samples to the logarithm of their mean ionization potentials $ln(I)$. However, two parameters of the fit function were determined by fitting 8 data points. It is thus legitimate to use the fit as there are still degrees of freedom. In future studies, a greater number of data points should be used though.

5.2.2 MVCT

A polynomial of second order was used to fit the relation between MVCT number and WEPL. Using this fit an accuracy of 10% or better was achieved for all metal samples but MCP-96. This means that MVCT could in principle be used to obtain the WEPL of metals. However, the suboptimal result for MCP-96, the only alloy in the sample, raises the question if this still holds true for more realistic implant materials for it has in general to be assumed that implants are made from alloys. The behavior of alloys should therefore be investigated in future studies.

The WEPL results obtained using the HLUT show very high accuracy for most materials. However, it has to be noted that the HLUT is an empirical HLUT that was set up using Gammex tissue equivalent materials, aluminum and titanium as calibration materials. The same materials were used in the measurements of this thesis. This makes the HLUT to a

certain degree biased towards these materials and may at least in part be the reason for the small residuals in the soft tissue regime and for light metals. Figure 5.2 shows the HLUT and the measured values of the Gammex and metal samples. It would be interesting to test the HLUT with other tissue equivalent samples to see if such good results can also be achieved with materials that were not used to set up the HLUT.

Some of the metal samples with high Z show high deviations from the reference WEPL. The results for iron and copper are better than those yielded by the fit that are shown in 4.11b, but the values for tungsten and tin are less precise than the results of the fit. Thus, the results do not suggest that the HLUT is in general superior to the fit. On the other hand, the HLUT was not set up to estimate the WEPL of heavy had to be extrapolated for CT numbers higher than 3096 HU.

To summarize, the HLUT has the disadvantage that it was extrapolated for high MVCT numbers and that the sample materials were used to set up the HLUT. This makes it possibly arbitrary for high CT numbers and to a certain degree biased for low CT numbers. The polynomial fit is, however, not a alternative as it is a very basic MVCT to WEPL relation compared to a look-up table. If MVCT was to be used to determine ion ranges in materials with high Z, it would be advisable to set up a HLUT optimized for this purpose. A dedicated HLUT set up to estimate ion ranges in typical implant materials might be a possibility to obtain more precise ion range estimations in such materials with a positive impact on clinical cases.

5.3 Artifacts due to High Z Materials

5.3.1 Insert Geometry

The results presented in the last chapter suggest that using a 16 bit CT scale instead of a 12 bit CT scale improves the insert diameter estimations obtained from the DECT measurements. It was possible to estimate the insert diameters very precise using 16 bit 100 and 140 kV DECT images combined with appropriate windowing as described in 4.4.1. Even the diameters of samples for which no reliable CT number was measurable (Fe, Cu, Mo, Sn, W, MCP-96) were estimated with good precision. The electron density and effective atomic number images do not seem to offer advantages for the estimation of the size of metal objects as the resulting diameters were less precise than those calculated from the 100 and 140 kV images.

The diameters estimated from the MVCT measurements could be measured with 2% accuracy except for the copper insert. However, the deviations are in order of the pixel size of the MVCT images (again except for copper).

In a more clinical situation, the windowing would likely be done manually. However, the point of this analysis rather was to show that size estimations of the investigated samples are possible.

In summary, both DECT and MVCT may be used to estimate the size of metal objects. The applicability of the method for real implant geometries, especially for very small implants where partial volume effects might be relevant or alloys and objects of unusual composition has yet to be investigated.

5.3.2 Artifacts in The Surrounding Material

The results from 4.4.2 show that the artifacts in the material around the inserts were comparable for all DECT contrasts. The artifacts around the aluminum and titanium inserts were rather moderate The severeness of the artifacts increased significantly for materials with higher atomic number. Only in the Z_{eff} images the artifact intensity was greatest around the iron and copper inserts which is unintuitive. Anyway, it has to be noted that the electron density and effective atomic number images do not show a reduction of artifacts around the metal inserts.

The artifacts are most likely caused by the high attenuation of metals and the resulting photon starvation as described in 2.1.6. The beam hardening correction applied to the images of the metal samples is obviously not sufficient to prevent artifacts, especially in case of materials with atomic numbers above that of titanium. Raw data based approaches that try to correct for missing projections as proposed in [37] might be tested to reduce the artifact's severeness. This kind of method removes projections with no information and tries to estimate their value from neighboring projections. The CT numbers of the object causing the artifacts is then lost, but may be restored by inserting the object's CT values yielded by a reconstruction without corrections. Such methods would be useful if no or few information on the artifact-causing object is expected from an image, e.g. for heavy metals in kV CT.

In the MVCT images an increase in artifact severeness is not observed. The image noise is in general higher than in kV CT, but the images do not seem to be affected by pronounced artifacts as figure 4.20 in the previous chapter clearly illustrates. MVCT measurements might therefore be an alternative imaging modality in case metal artifacts produced by kilo voltage imaging modalities pose a problem.

5.4 Differentiation of Materials

Even though it was not possible to measure the electron density and effective atomic number of iron and heavier metals, it can be noted that the limit where distinguishing between materials is not possible anymore is reached only for molybdenum and heavier metals. This leaves a gap reaching from at worst vanadium to at least copper where materials can not be measured accurately but the remaining information of the CT numbers may allow to distinguish these materials. At least, one may classify a material with the corresponding DECT characteristics as belonging to an effective atomic number range between 23 and 29. It might even be possible to distinguish materials inside this range from each other, though this claim would need additional experimental support.

To summarize, there may be three regimes for metal samples in DECT:

1. *Up to at least Z = 22:* A reliable measurement of the electron density and the effective atomic number is possible for materials with lower effective atomic number.

2. *Z = 23 to at least Z = 29:* Materials with a medium effective atomic number may be distinguishable from materials outside of the regime and perhaps even from each other.

3. *Z = 30 and higher:* No information can be obtained for materials with high effective

atomic number, but they may be distinguishable from materials in the other two regimes.

This observation may be used for the discrimination or even identification of materials. However, it has to be noted that this notion was only derived from one measurement; the claim was not thoroughly tested. On the other hand, implants are usually made of a limited number of base materials. Additionally, some materials can be found only in certain body regions, e.g. newer hip prostheses are often made from titanium whereas older models may be composed of denser alloys. Titanium and these alloys can be distinguished by the DECT method as demonstrated in 5.7.2. This limitation of certain implant materials to certain body regions may in combination with the (residual) information of the DECT values allow to identify materials or at least distinguish them from other possible materials. Therefore, it might be worth to keep this point in mind during further studies with realistic implant samples.

5.5 Comparison Between DECT And MVCT

The most obvious difference between DECT and MVCT is the fact that the latter allowed quantitative measurements of CT numbers for all metal samples. This makes MVCT the method of choice if materials with high atomic number need to be characterized quantitatively. The absence of streaking artifacts around heavy metals is another huge advantage of MVCT in the high Z regime.

The precision of the WEPL of light metals was improved by DECT in comparison with a 120 kV HLUT. Therefore, the WEPL estimations for these materials from DECT and MVCT should be considered in a comparison of both modalities. With DECT, the WEPL of aluminum had an accuracy of 4.88% and that of titanium an accuracy of 2.75%. The accuracy obtained with the MVCT fit was under 4% for aluminum and about 2% for titanium. The MVCT HLUT yielded an accuracy of under 1% for both materials. The results from the HLUT are, however, biased for these materials as already discussed in 5.2.2. Still, even the WEPL yielded by the fit is not only comparable, but slightly better than the result obtained with DECT. The artifacts observed in DECT with raw data based beam hardening correction and MVCT are for both modalities not very pronounced. With regard to WEPL values alone, MVCT seems to have at least a slight advantage over DECT.

However, there is a number of practical considerations in favor of DECT. MVCT scans are not very flexible, at least using the device employed in this thesis. Only one field of view and only three different slice thicknesses are possible. MVCT scans also take considerably more time. DECT scans can be done within seconds, MVCT scans take several minutes even with the biggest slice thickness. DECT is faster and more flexible than MVCT, at least if done with the devices used in this thesis, and enables a WEPL estimation for light metals with an accuracy comparable to that achieved with MVCT. If a material discrimination as discussed in 5.4 was possible, DECT might even be sufficient for certain cases involving metals that are denser than titanium. Additionally, DECT offers in principle more tissue information than MVCT because the electron density and effective atomic number can be computed, while MVCT only offers one image contrast. The resulting WEPL estimations, however, suggest that the additional information of DECT may not provide an advantage over MVCT for the characterization of light metals. Furthermore, the patient receives less

dose from DECT. These advantages make it more of a routine device. The performance of MVCT comes at the cost of higher dose, less flexibility and longer measurement times. Still, it may be of advantage in complicated cases where materials with high Z cannot be avoided in treatment planning and exact ion range estimations of these materials are necessary.

5.6 DECT to WEPL by Classification

Discriminant analysis was used to predict the WEPL of a tissue sample. The sample was a frozen pig head that was measured with DECT with 80/140 kV. Figure 5.3a shows a slice from the 80 kV image. The WEPL prediction was done for each voxel independently using QDA. Figure 5.4a shows the results of the WEPL prediction. The predicted WEPL was compared to a reference WEPL obtained from a 120 kV CT scan of the sample. Figure 5.3b shows a slice image of this reference WEPL. The posterior probabilities yielded by the prediction were used to interpolate between WEPL classes. Figure 5.4b shows the results. In Figure 5.5 the differences between predicted WEPL and WEPL calculated with a 120 kV HLUT are plotted. Unfortunately, the WEPL predictions don't improve significantly if the additional correction by interpolation is applied. The mean absolute deviation between predicted WEPL and WEPL calculated with the HLUT is 0.0205 without interpolation and 0.0202 with interpolation between WEPL classes.

However, it can be noted in 5.5 that there are "hot spots" with very high deviation from the reference WEPL calculated with the HLUT. These areas are predominantly situated at edges or other positions where high WEPL gradients can be found. It seems that partial volume effects at edges make it hard for the discriminant algorithm to determine the right WEPL class because the "mixed" CT numbers of voxels that cover areas with very different CT numbers do not fit to the characteristic CT values of the classes from the learning sample. One might try to use some sort of edge detection algorithm to identify edges and smoothen the WEPL in case of suspicious WEPL values. However, one might introduce new uncertainties by doing this and decrease the overall accuracy.

A principle limitation of predicting the WEPL from DECT the way it was done in this thesis is that discrete WEPL classes are predicted. The classes are given by the materials that were used as learning sample, in this case the Gammex and polymer samples. This is of course not very realistic as real tissue samples have a continuous WEPL range. Therefore it is inevitable that many or even most voxels will be assigned an inaccurate WEPL. The WEPL class predicted for a certain voxel will be the WEPL of the material from the learning sample whose DECT numbers are nearest to those of the voxel. A WEPL determination by classification as described here can therefore never be as exact as a well set up HLUT using the same data.

The idea to interpolate between WEPL classes with the posterior probabilities as interpolation weights to improve the predicted WEPL of materials whose DECT numbers are in the "gaps" between the DECT numbers of the materials from the learning sample sounds reasonable at first. However, the discriminant analysis routines used in this thesis yield posterior probability distributions that assign materials in general very decidedly to a certain WEPL class. Usually one WEPL class has a posterior probability of approximately 1 and all other classes have a posterior probability of nearly 0. Figure 5.6 shows this very clearly. This means that the attempt to interpolate between WEPL classes using

the posterior probabilities as weights will most likely not yield a significant improvement of the WEPL prediction. Judging from these results, a WEPL determination using some sort of continuous function like a HLUT might be superior to discriminant analysis approaches similar to the method used in this thesis.

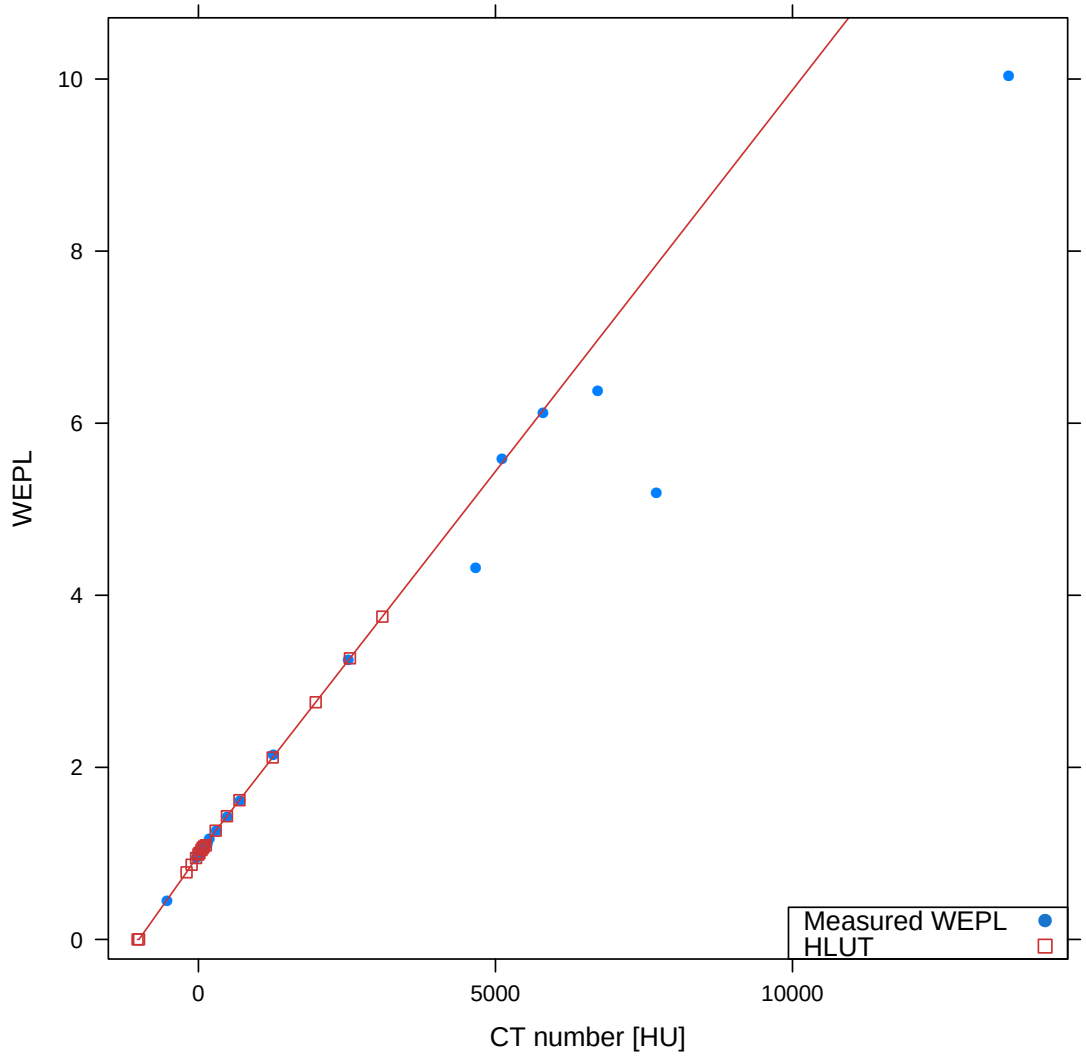

Figure 5.2: The MVCT HLUT is shown in red. The HLUT was extrapolated linearly using the last two data points to cover CT numbers beyond its upper limit of 3096. The measured WEPL of the samples is depicted in blue.

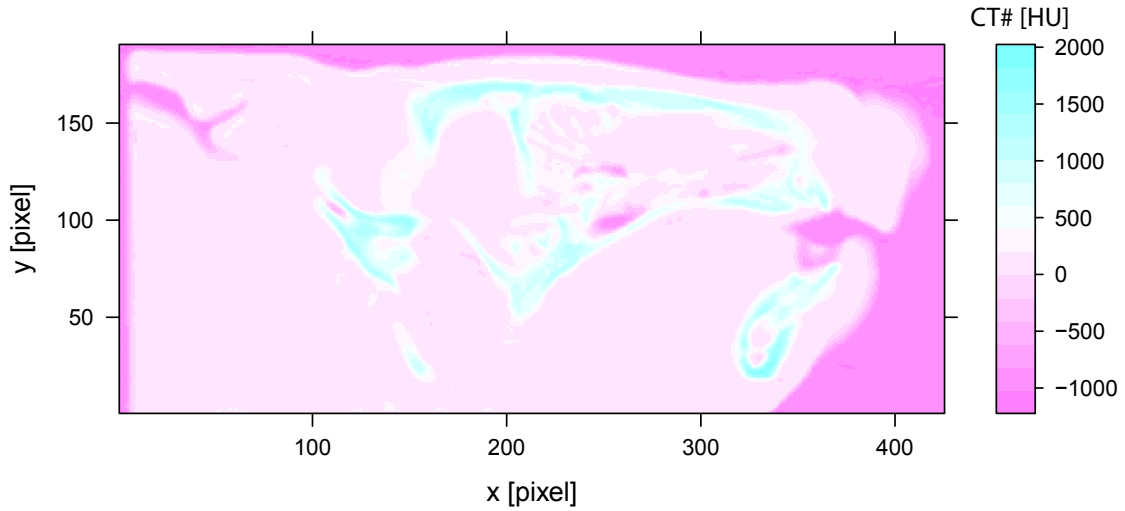

(a) DECT 80 kV image of pig head sample.

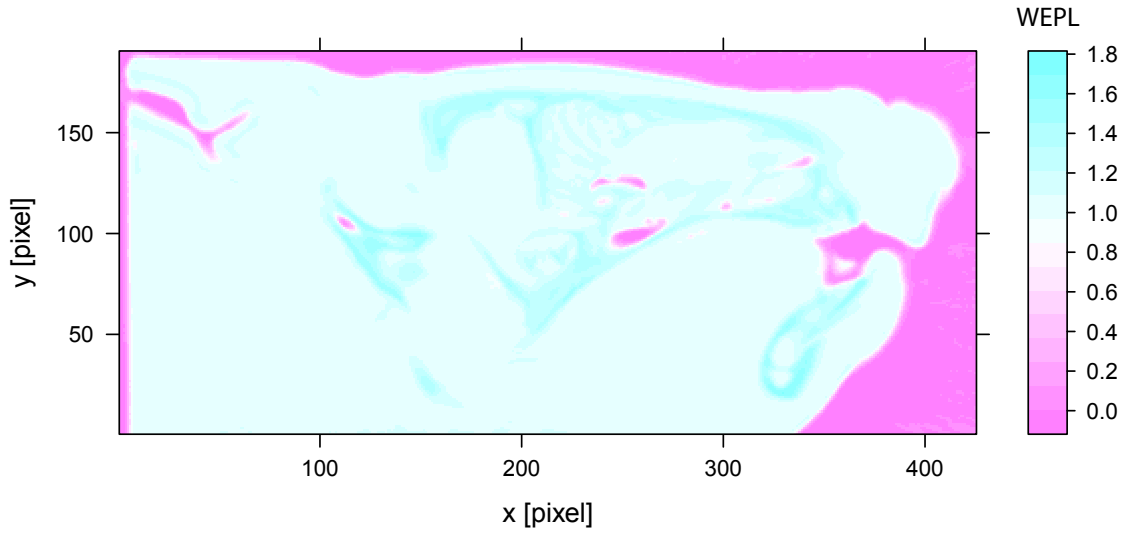

(b) WEPL of pig head sample calculated with 120 kV HLUT.

Figure 5.3

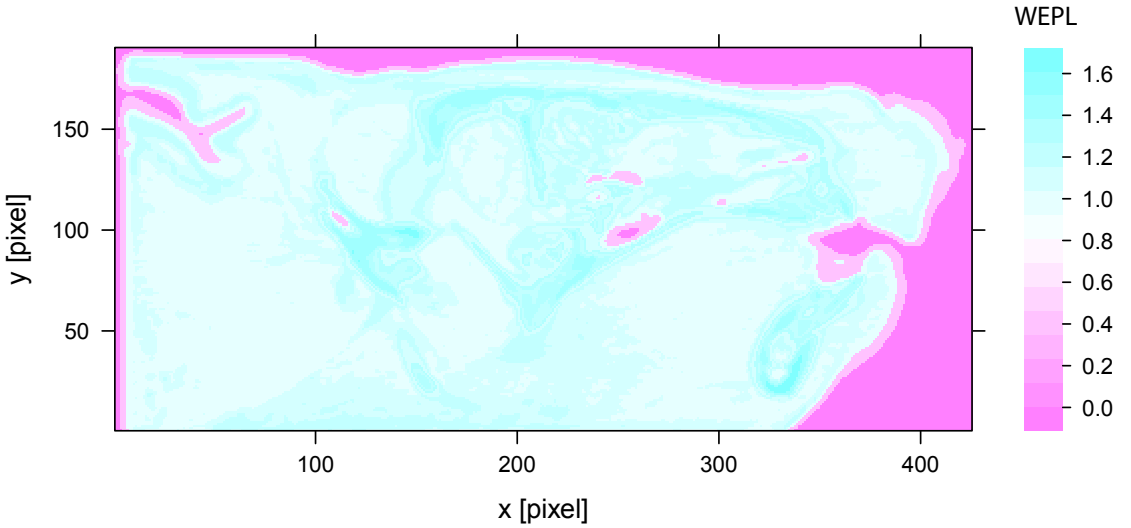

(a) WEPL of pig sample predicted from DECT data.

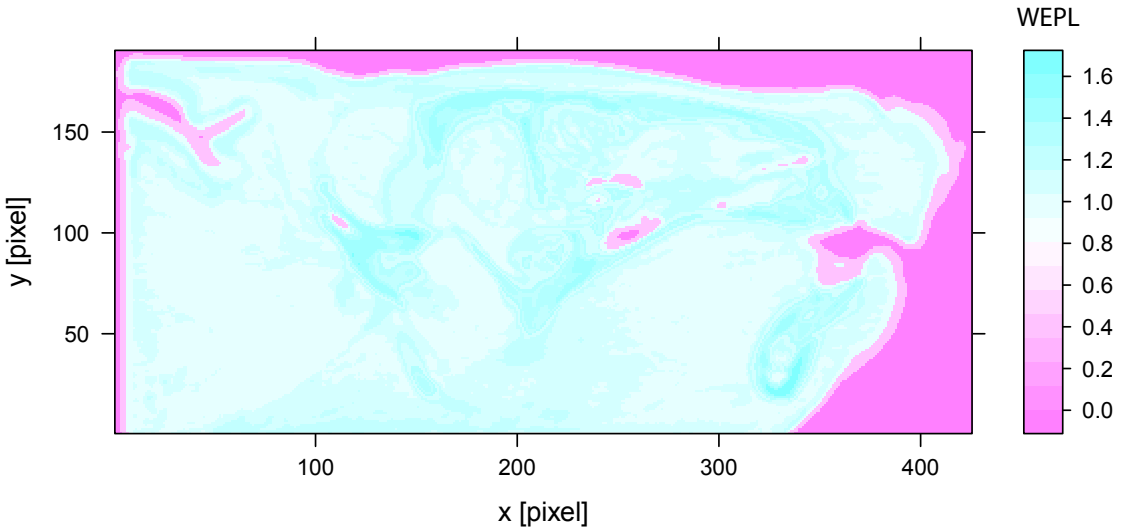

(b) WEPL of pig sample predicted from DECT data with interpolation between WEPL classes.

Figure 5.4

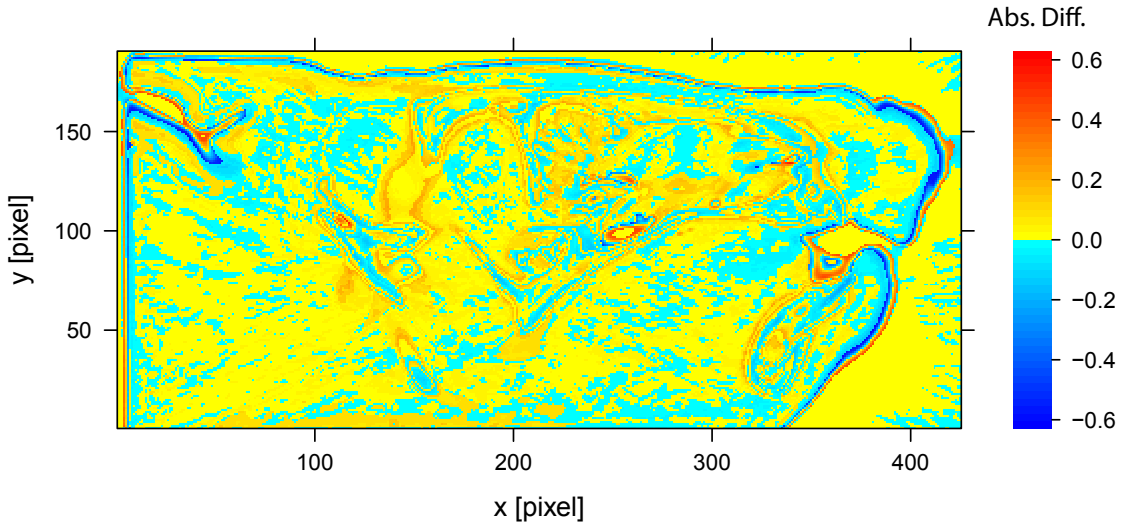

(a) Difference between WEPL predicted by discriminant analysis and WEPL calculated with 120 kV HLUT.

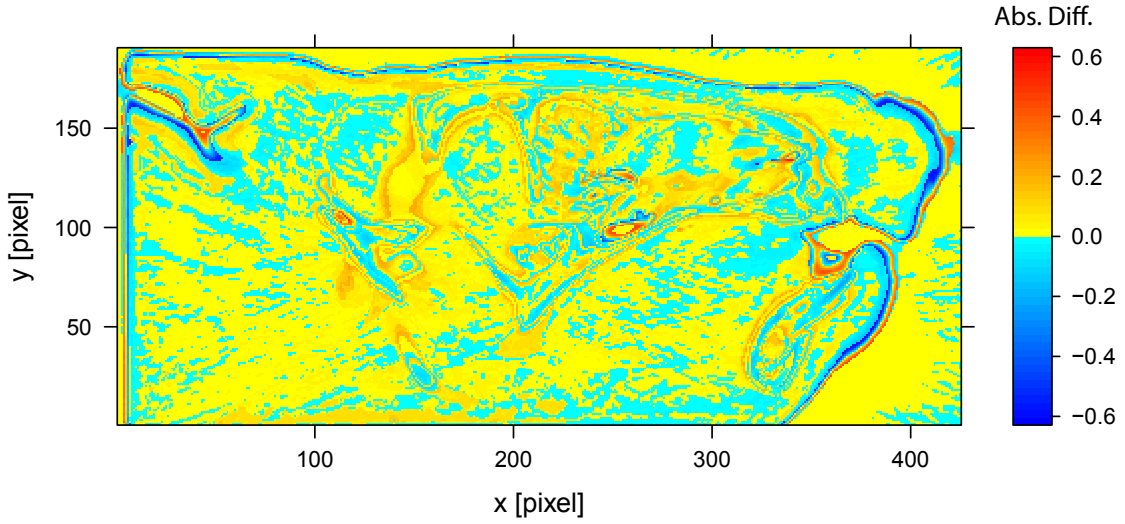

(b) Difference between WEPL predicted by discriminant analysis with additional interpolation between WEPL classes based on the posterior probabilities and WEPL calculated with 120 kV HLUT.

Figure 5.5: Pig head sample.

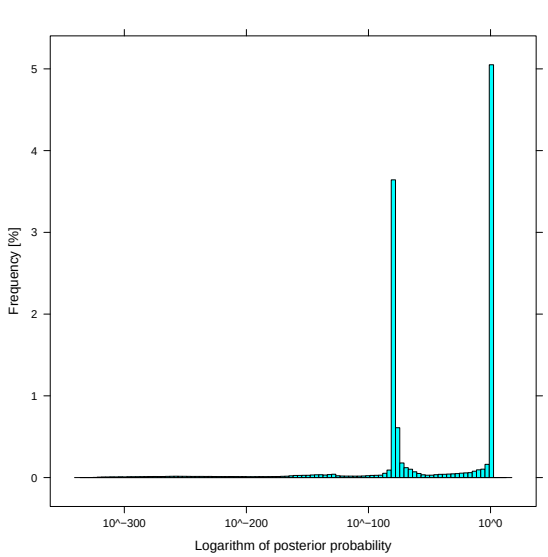

(a) The values of the posterior probabilities of all sample voxels. This is to show that the posterior probabilities are usually either approximately 0 or approximately 1.

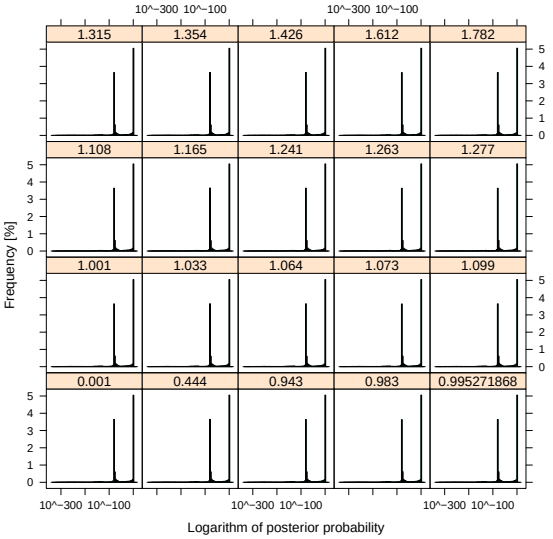

(b) The posterior probability values of each WEPL class. The same pattern as in (a) is observed: the posterior probability is either approximately 0 or approximately 1.

Figure 5.6

5.7 Outlook

5.7.1 General Questions And Issues

Alloys and realistic implant samples. In this thesis the emphasis was put on pure metals to study the general feasibility of WEPL estimations with DECT and MVCT over a large atomic number scale. However, implant materials are usually alloys because of their often superior material properties. Therefore, the behavior of realistic implant alloys should be investigated. The fact that the WEPL of MCP-96, the only alloy used in this thesis, showed great deviations when it was estimated from MVCT data suggests that alloys and the behavior of composite materials should be investigated further. Ideally, one would use actual implants as this would allow to study the preciseness of the DECT and MVCT HLUTs and the geometrical characterization of metal implants for complex material compositions and object shapes.

DECT algorithm. One might investigate if there are known limitations of the algorithm that computes the electron density and effective atomic number for composite materials containing certain elements such as chlorine because great deviations of the computed electron density and effective atomic number from the reference values were observed for PVC.

Artifact reduction for high Z materials. The DECT images of materials with high atomic number showed severe streaking artifacts. The images were corrected for beam hardening. However, the high attenuation of high Z metals still caused streaking artifacts. It should therefore be investigated if correction algorithms are available. Possible approaches are for example iterative algorithms that combine corrections for beam hardening effects which cause artifacts around low Z metals and corrections for missing projections caused by high Z metals as proposed in [37] or normalized metal artifact reduction as presented in [21].

Monoenergetic extrapolation which computes a virtual monoenergetic image using the DECT information may be an alternative to reduce artifacts at least for light metals. In [2] the diagnostic value of images could be improved by this method. Its applicability for ion beam therapy treatment planning was not investigated in this thesis. However, a study would be in principle possible as the software tool is available at DKFZ's DECT scanner.

kV-MV CT. CT with x-ray spectra in the kV region offers good soft tissue contrast while MVCT allows to measure even high Z materials without significant artifacts. It was suggested by [41] that combining both energy regimes might yield better ion range estimations. Following [22] who reported possible benefits for patients with metal implants, it might be worth investigating if a WEPL estimation based on both kV CT and MVCT allows to achieve better results for scenarios where high Z materials are present.

It might be worth to try and set up a two-dimensional HLUT that links two CT numbers directly to the ion range. A calculation of electron densities and effective atomic numbers may not necessarily be required as the material information is in principle already contained in the CT images. Such a HLUT may furthermore be easier to implement as the computation of electron density and effective atomic number.

Orthovoltage CT (OVCT) using x-ray spectra of several hundred keV may be a low-dose alternative to CT with MV photons. It was reported in [42] that OVCT may be beneficial for patients with metal implants in comparison to kV CT. Unfortunately, OVCT scanners are (to the best of the author's knowledge) currently not commercially available.

The MVCT HLUT used in this thesis was not specifically set up for materials with high atomic number. Therefore, the set up of a dedicated MVCT HLUT for such materials using realistic implant alloys is another interesting topic.

Classification with interpolation between classes. The classification algorithm used in this thesis allocated to each voxel of the DECT images the WEPL of the learning sample material that fit best. The WEPL prediction for materials whose WEPL lies between the WEPL of two learning sample materials could be improved if interpolation between WEPL classes was possible. Since the classification tools used in this thesis are rather basic, improvement of the classification approach may be possible by more sophisticated tools.

5.7.2 WEPL Determination of an Implant Sample

In order to give a more clinical outlook on the implementation of DECT into the treatment planning process, the WEPL of the Harms cages and the hip endoprosthesis described in section 3.1 was determined using electron density and effective atomic number calculated from 100/140Sn kV DECT images. For voxels with a electron density larger than that of titanium the DECT results were considered as not accurate. However, as discussed in 5.4, a material discrimination is possible to a certain degree. Therefore, the electron density was used to discriminate materials.

If the electron density in a certain voxel was between the values measured for titanium and copper, a WEPL estimation by interpolation was done. The incorrect electron density value of the voxel was used to calculate a WEPL by interpolating linearly between the data points of titanium and copper in the electron density - WEPL diagram. The incorrect electron density values from DECT are thus used to distinguish materials between titanium and copper. They are not used to calculate the WEPL, but rather to scale between the WEPL values of titanium and copper. This assumes a linear trend of the wrong electron density values towards the saturation plateau which is arbitrary and cannot be motivated from the data. However, with only few data points, the use of more complex functions is pointless. This attempt to estimate a WEPL from the incorrect electron density values is very qualitative and was made to illustrate how the residual information of DECT may be used to distinguish materials.

Materials with an electron density larger than that of copper were considered indistinguishable from each other and were assigned the WEPL of molybdenum. Figure 5.7 shows the resulting WEPL images.

Table 5.1 shows results of rather qualitative measurements of the calculated WEPL in a certain region of interest in figure 5.7. Mean and maximum values are given as well as a reference WEPL calculated from the assumed composition of the implants (see section 3.1) and reference I values from [23]. However, the reference values should not be regarded as necessarily correct as the material composition of the implants is only known in approximation. The measurements show a general underestimation of the WEPL in comparison to the reference values. In case of the harms cages, this is at least in part due to partial volume effects caused by the small thickness of the implant's walls. This leads to a drastic underestimation of the WEPL of the harms cages. However, one must note that the occurrence of partial volume effects is not a problem of DECT specifically but of CT in general.

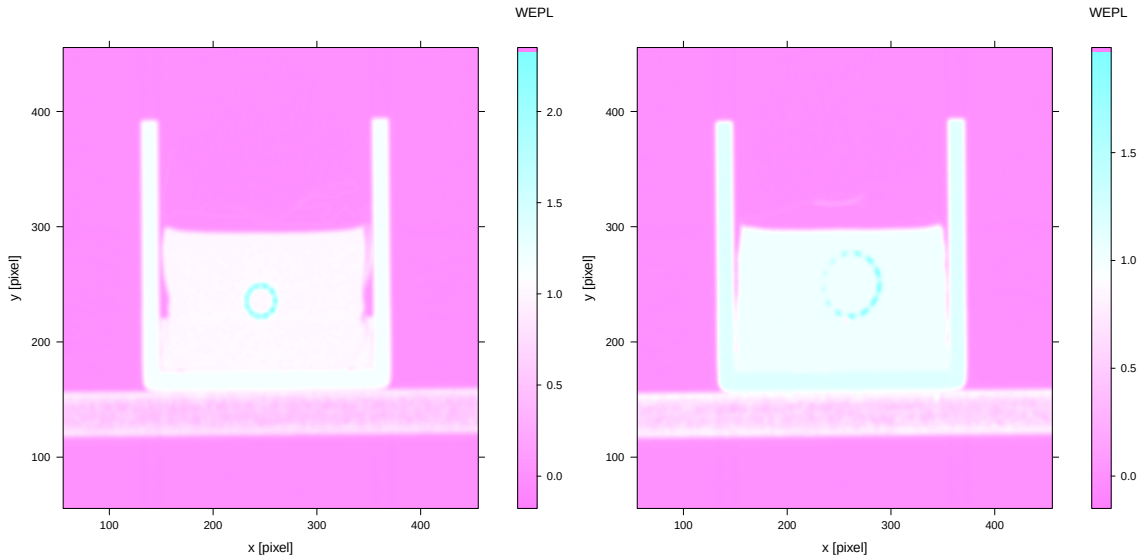

(a) WEPL estimation for the small Harms cage.

(b) WEPL estimation for the large Harms cage.

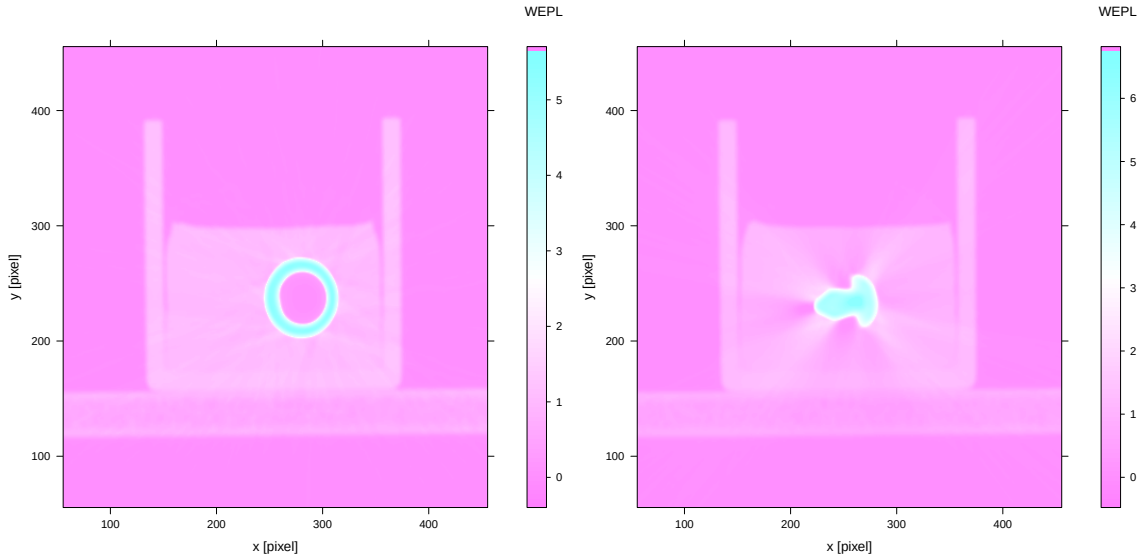

(c) WEPL estimation for a part of the head of a hip endoprosthesis. The WEPL was estimated by extrapolation using the residual information of the DECT images.

(d) WEPL estimation for a part of the shaft of a hip endoprosthesis. The WEPL was again estimated by extrapolation.

Figure 5.7

The WEPL of the hip prosthesis can be estimated surprisingly well. The high maximum value that occurs in a whole area of the shaft's center might be caused by the high attenuation of the massive and rather thick material.

Table 5.1: Results of the WEPL estimation for the implant samples.

Implant	Mean WEPL	Max WEPL	Calculated WEPL
Small Harms Cage	2.10	2.20	3.25
Large Harms Cage	1.79	1.86	3.25
Head Hip Prosthesis	5.17	5.29	5.79
Shaft Hip Prosthesis	5.49	6.37	5.79

Streak artifacts can be noticed around the hip prosthesis in both images. The artifacts are especially pronounced around the massive shaft of the implant. This may reduce the usefulness of the WEPL images. Additional artifact corrections as mentioned in 2.1.6 might be used to facilitate a clinical application.

6 Conclusion

This thesis investigated the potential of DECT to improve ion range estimations of metal objects. A number of pure metals from aluminum up to tungsten was used as sample materials. The samples were measured with DECT. The WEPL was calculated with a DECT HLUT. For comparison with DECT, the samples were also measured with MVCT. Also, classification with discriminant analysis was investigated as an alternative approach to predict ion ranges without physical model.

The DECT images of the metal samples were provided on a 16 bit CT scale and with raw data based beam hardening correction and the electron density, effective atomic number and CT numbers were analyzed. The electron density and effective atomic number of aluminum ($Z = 13$) and titanium ($Z = 22$) could be determined within the range of a few percent. The electron density and effective atomic number of the metal samples with an atomic number higher than that of titanium could not be determined precisely, but up to at least copper ($Z = 29$) a material distinction may be possible using the residual information of the CT numbers. The samples with $Z \geq 42$ were not distinguishable. It is assumed that photon starvation and cross scattering prevent meaningful measurements in this material region.

The WEPL was measured and independently predicted from the electron density and effective atomic number. For aluminum the deviation from the reference value was 4.88% and for titanium 2.75%. The WEPL of metal samples with higher atomic number could not be calculated because the electron density and effective atomic number could not be determined from DECT. A material distinction may in certain cases allow to estimate the WEPL of these materials.

The rod diameters of all samples could be determined with high accuracy from 16 bit CT images using appropriate windowing (full width at half maximum of the CT number).

The severeness of artifacts in the material around the metal samples was assessed. No significant improvement between the 100/140 kV images and the electron density and effective number images could be noted. The artifacts around the aluminum and titanium samples were not very pronounced. It seems that the artifacts around these materials are mostly due to beam hardening and that the applied correction allows to obtain largely artifact-free images. However, severe streaking artifacts could be observed around the samples with higher atomic number. Apparently, a correction for beam hardening is not sufficient for these materials as the artifacts seem to be caused by photon starvation and cross scattering. Additional corrections have to be applied as discussed in 5.7.1.

The samples were additionally scanned with MVCT for comparison with DECT. The WEPL was calculated using a fit of the MVCT numbers with a polynomial of second order and an experimental HLUT and could be determined with similar precision as with DECT for materials up to titanium. In contrast to DECT, the WEPL of the high Z samples could be determined as well, but for some materials with high deviations from the reference values. Streak artifacts were hardly noticeable in the MVCT images. The sample diameters could be determined for all metal samples. MVCT may therefore be superior

to DECT in case of materials with very high atomic number, but suffers from higher dose and increased scan time. Thus, DECT may be considered as a device for routine cases involving metal implants while MVCT may be employed in selected, more critical cases.

To investigate an alternative approach to predict ion ranges from DECT measurements, discriminant analysis was used to predict the WEPL of a pig head sample from 100/140Sn kV DECT numbers. The mean absolute deviation from the WEPL estimation of a standard 120 kV HLUT was $2.05 \cdot 10^{-2}$ without interpolation between WEPL classes and $2.02 \cdot 10^{-2}$ with interpolation. However, very high deviations occurred at edges of the sample with a high WEPL gradient. These deviations may be caused by miss-classifications due to partial volume effects. However, the results might be improved by more sophisticated classification tools.

The metal samples were mostly pure metals. Therefore, the accuracy of the used methods should be tested for alloys and realistic implant samples in future studies.

6.1 List of Figures

6.2 List of Tables

7 Bibliography

[1] R. E. Alvarez and a. Macovski. Energy-selective reconstructions in X-ray computerized tomography. *Physics in medicine and biology*, 21(5):733–44, Sept. 1976.

[2] F. Bamberg, A. Dierks, K. Nikolaou, M. F. Reiser, C. R. Becker, and T. R. C. Johnson. Metal artifact reduction by dual energy computed tomography using monoenergetic extrapolation. *European radiology*, 21(7):1424–9, July 2011.

[3] M. Bazalova, J.-F. Carrier, L. Beaulieu, and F. Verhaegen. Dual-energy CT-based material extraction for tissue segmentation in Monte Carlo dose calculations. *Physics in medicine and biology*, 53(9):2439–56, May 2008.

[4] M. Bazalova, J.-F. Carrier, L. Beaulieu, and F. Verhaegen. Tissue segmentation in Monte Carlo treatment planning: a simulation study using dual-energy CT images. *Radiotherapy and oncology : journal of the European Society for Therapeutic Radiology and Oncology*, 86(1):93–8, Jan. 2008.

[5] S. Breusch and K.-D. Kühn. Knochenzement auf Basis von Polymethylmethacrylat. *Der Orthopäde*, 32(1):41–50, 2003.

[6] N. G. Burnet, E. J. Adams, J. Fairfoul, G. S. J. Tudor, a. C. F. Hoole, D. S. Routsis, J. C. Dean, R. D. Kirby, M. Cowen, S. G. Russell, Y. L. Rimmer, and S. J. Thomas. Practical aspects of implementation of helical tomotherapy for intensity-modulated and image-guided radiotherapy. *Clinical oncology (Royal College of Radiologists (Great Britain))*, 22(4):294–312, May 2010.

[7] T. M. Buzug. *Einführung in dieComputertomographie*. Springer-Verlag, Berlin Heidelberg New York, 2004.

[8] A. J. Coleman and M. Sinclair. A beam-hardening correction using dual-energy computed tomography. *Physics in medicine and biology*, 30(11):1251–6, Nov. 1985.

[9] S. E. Combs, O. Jäkel, T. Haberer, and J. Debus. Particle therapy at the Heidelberg Ion Therapy Center (HIT) - Integrated research-driven university-hospital-based radiation oncology service in Heidelberg, Germany. *Radiotherapy and oncology : journal of the European Society for Therapeutic Radiology and Oncology*, 95(1):41–4, Apr. 2010.

[10] S. Ecker. Heidelberger Ionenstrahl-Therapiezentrum (HIT). Personal communication.

[11] K. J. Engel, C. Herrmann, and G. Zeitler. X-ray scattering in single- and dual-source CT. *Medical Physics*, 35(1):318, 2008.

[12] T. Hastie, R. Tibshirani, and J. Friedman. *The Elements of Statistical Learning*. Springer-Verlag, New York, NY, USA, 2009.

[13] N. Hünemohr. DKFZ, Heidelberg. Personal communication.

[14] N. Hünemohr. *Improvement of ion therapy planning by the use of dual energy computed tomography*. Diploma thesis, University of Heidelberg, 2011.

[15] O. Jäkel and P. Reiss. The influence of metal artefacts on the range of ion beams. *Physics in medicine and biology*, 52(3):635–44, Feb. 2007.

[16] T. R. Johnson, C. Fink, S. O. Schönberg, and M. F. Reiser. *Dual Energy CT in Clinical Practice*. Springer-Verlag, Berlin Heidelberg, 2011.

[17] W. A. Kalender. *Computed Tomography*. Publicis MCD Verlag, Munich, Germany, 2000.

[18] B. Krauss. Siemens Healthcare AG. Personal communication.

[19] Y. Kyriakou, E. Meyer, D. Prell, and M. Kachelrieß. Empirical beam hardening correction (EBHC) for CT. *Medical Physics*, 37(10):5179, 2010.

[20] C. Maass, E. Meyer, and M. Kachelriess. Exact dual energy material decomposition from inconsistent rays (MDIR). *Medical physics*, 38(2):691–700, Feb. 2011.

[21] E. Meyer, R. Raupach, M. Lell, B. Schmidt, and M. Kachelrieß. Normalized metal artifact reduction (NMAR) in computed tomography. *Medical Physics*, 37(10):5482, 2010.

[22] W. D. Newhauser, A. Giebeler, K. M. Langen, D. Mirkovic, and R. Mohan. Can megavoltage computed tomography reduce proton range uncertainties in treatment plans for patients with large metal implants? *Physics in medicine and biology*, 53(9):2327–44, May 2008.

[23] I. C. on Radiation Units and Measurements. *ICRU Report*. Number Nr. 37 in National Bureau of Standards handbook. International Commission on Radiation Units and Measurements., 1984.

[24] M. Petersilka, K. Stierstorfer, H. Bruder, and T. Flohr. Strategies for scatter correction in dual source CT. *Medical Physics*, 37(11):5971, 2010.

[25] D. Prell, Y. Kyriakou, M. Kachelrieß, and W. A. Kalender. Reducing Metal Artifacts in Computed Tomography Caused by Hip Endoprostheses Using a Physics-Based Approach. *Investigative Radiology*, 45(11):747–754, 2010.

[26] R Development Core Team. *R: A Language and Environment for Statistical Computing*. R Foundation for Statistical Computing, Vienna, Austria, 2012. ISBN 3-900051-07-0.

[27] E. Rietzel, D. Schardt, and T. Haberer. Range accuracy in carbon ion treatment planning based on CT-calibration with real tissue samples. *Radiation oncology (London, England)*, 2:14, Jan. 2007.

[28] E.-P. Ruehrnschopf and K. Klingenbeck. A general framework and review of scatter correction methods in x-ray cone-beam computerized tomography. Part 1: Scatter compensation approaches. *Medical Physics*, 38(7):4296, 2011.

[29] U. Schneider, E. Pedroni, and A. Lomax. The calibration of CT Hounsfield units for radiotherapy treatment planning. *Physics in medicine and biology*, 41(1):111–24, Jan. 1996.

[30] M. Semlitsch. Properties of wrought CoNiCrMo alloy Protasul-10, a highly corrosion and fatigue resistant implant material for joint endoprostheses. *Engineering in medicine*, 9(4):201–207, 1980.

[31] P. M. Shikhaliev and S. G. Fritz. Photon counting spectral CT versus conventional CT: comparative evaluation for breast imaging application. *Physics in medicine and biology*, 56(7):1905–30, Apr. 2011.

[32] Siemens. Somatom Workflow Assistant - Definition syngo CT 2012A, 2009.

[33] M. Splinter. *Erstellung einer MV-CT Hounsfield Look Up Tabelle (HLUT) für die Bestrahlungsplanung in der Ionenstrahltherapie*. Projektarbeit, Duale Hochschule Baden Württemberg Karlsruhe, 2012.

[34] M. Torikoshi, T. Tsunoo, M. Sasaki, M. Endo, Y. Noda, Y. Ohno, T. Kohno, K. Hyodo, K. Uesugi, and N. Yagi. Electron density measurement with dual-energy x-ray CT using synchrotron radiation. *Physics in Medicine and Biology*, 48(5):673, 2003.

[35] G. Van Gompel, K. Van Slambrouck, M. Defrise, K. J. Batenburg, J. de Mey, J. Sijbers, and J. Nuyts. Iterative correction of beam hardening artifacts in CT. *Medical physics*, 38 Suppl 1(7):S36, May 2011.

[36] W. J. H. Veldkamp, R. M. S. Joemai, A. J. van der Molen, and J. Geleijns. Development and validation of segmentation and interpolation techniques in sinograms for metal artifact suppression in CT. *Medical Physics*, 37(2):620, 2010.

[37] J. M. Verburg and J. Seco. CT metal artifact reduction method correcting for beam hardening and missing projections. *Physics in medicine and biology*, 57(9):2803–18, May 2012.

[38] J. F. Williamson, S. Li, S. Devic, B. R. Whiting, and F. a. Lerma. On two-parameter models of photon cross sections: Application to dual-energy CT imaging. *Medical Physics*, 33(11):4115, 2006.

[39] C. Xu, F. Verhaegen, D. Laurendeau, S. a. Enger, and L. Beaulieu. An algorithm for efficient metal artifact reductions in permanent seed implants. *Medical Physics*, 38(1):47, 2011.

[40] M. Yang, G. Virshup, J. Clayton, X. R. Zhu, R. Mohan, and L. Dong. Theoretical variance analysis of single- and dual-energy computed tomography methods for calculating proton stopping power ratios of biological tissues. *Physics in medicine and biology*, 55(5):1343–62, Mar. 2010.

[41] M. Yang, G. Virshup, J. Clayton, X. R. Zhu, R. Mohan, and L. Dong. Does kV-MV dual-energy computed tomography have an advantage in determining proton stopping power ratios in patients? *Physics in medicine and biology*, 56(14):4499–515, July 2011.

[42] M. Yang, G. Virshup, R. Mohan, C. C. Shaw, X. R. Zhu, and L. Dong. Improving accuracy of electron density measurement in the presence of metallic implants using orthovoltage computed tomography. *Medical Physics*, 35(5):1932, 2008.

[43] N. Yang, P. Leichner, and W. Hawkins. Effective atomic numbers for low-energy total photon interactions in human tissues. *Medical Physics*, 14(5):759–766, 1987.

[44] X. Zhang, J. Wang, and L. Xing. Metal artifact reduction in x-ray computed tomography (CT) by constrained optimization. *Medical Physics*, 38(2):701, 2011.

A Boxplots Describing Artifacts Around The Metal Samples in DECT

This section shows Box and Whisker plots of the artifacts on a circle with radius of 70 pixel around the metals samples. The median value is at the middle of the boxes. The outer limits of the boxes are the 25 % and 75 % quartiles of the distribution of measurement values. The whiskers mark the point of $1.5 \cdot IQR$ (**I**nter **Q**uartile **R**ange, the distance between the quartiles). Outliers are drawn seperately.

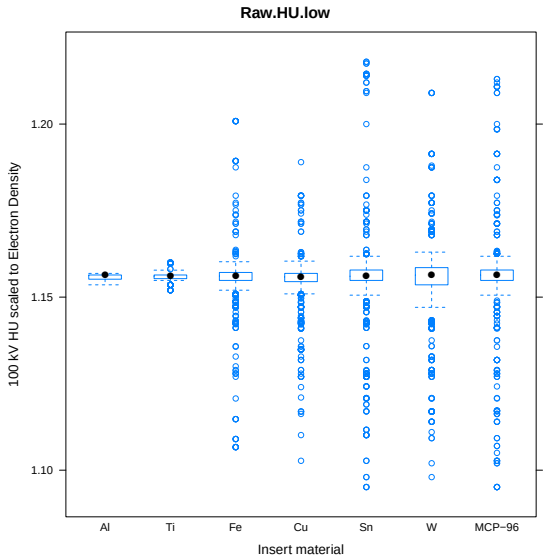

(a) Artifacts in the 100 kV DECT images on a circle with radius of 70 pixel around the metal sample's center.

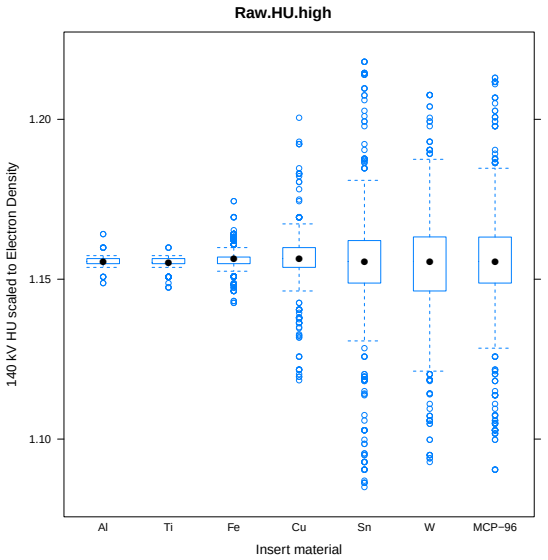

(b) Artifacts in the 140 kV DECT images.

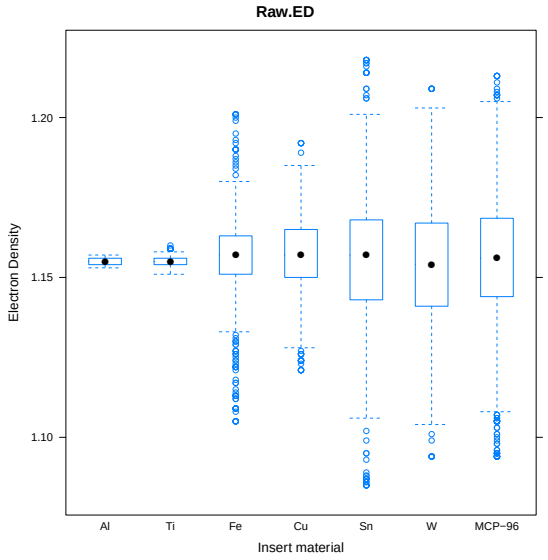

(c) Artifacts in the electron density images. No improvement over the 100 and 140 kV images is visible.

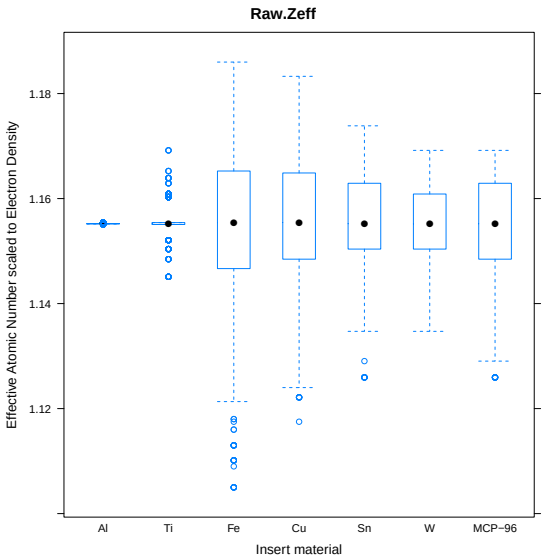

(d) Artifacts in the effective atomic number images. Again no improvement is visible.

Figure A.1

B Impact of Phantom Size on DECT Numbers

The impact of the size of the PMMA phantom around the metal samples was studied by varying the phantom radius between 80 mm, 50 mm and 25 mm. It has to be noted that the results of this analysis are only of limited value since the CT reconstruction algorithms are not optimized for very small phantom radii. The reason for this is that very small phantom radii are not considered as realistic patient sizes.

Nevertheless, the variation of electron density and effective atomic number for different phantom radii is not very pronounced, see B.1.

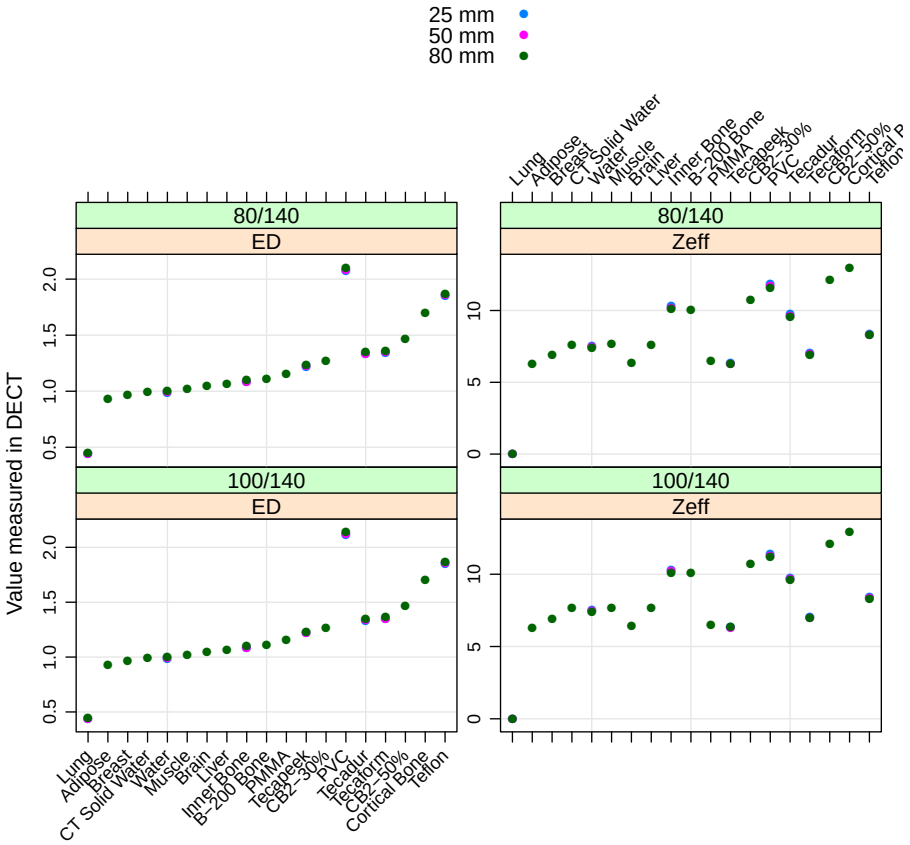

Figure B.1: Electron density ED and effective atomic number Zeff measured with 100/140 kV and 80/140 kV and the following phantom radii: 25 mm, 50 mm and 80 mm.

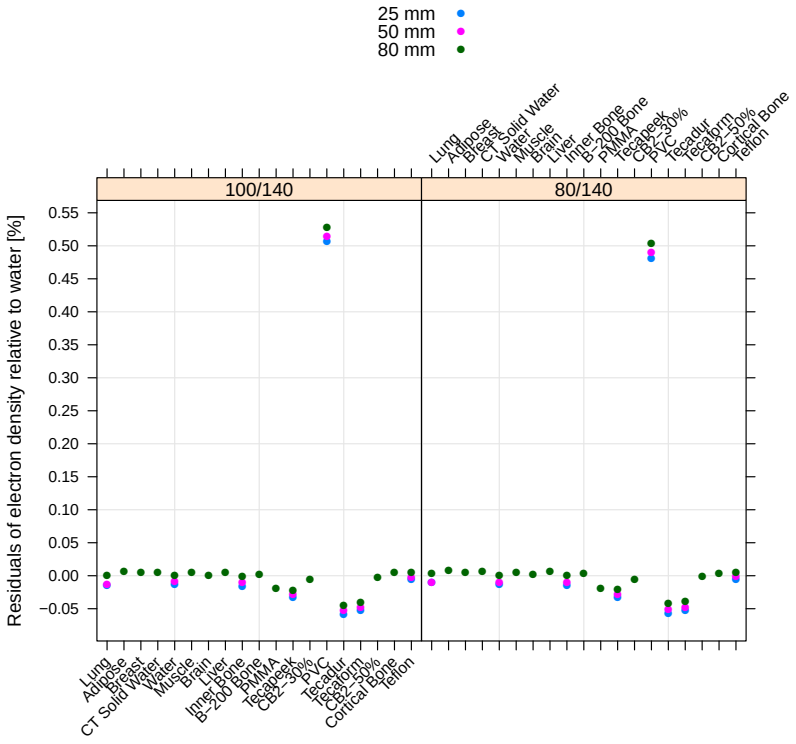

(a) Residuals of measured electron density and reference value for 100/140 kV and 80/140 kV and the following phantom radii: 25 mm, 50 mm and 80 mm.

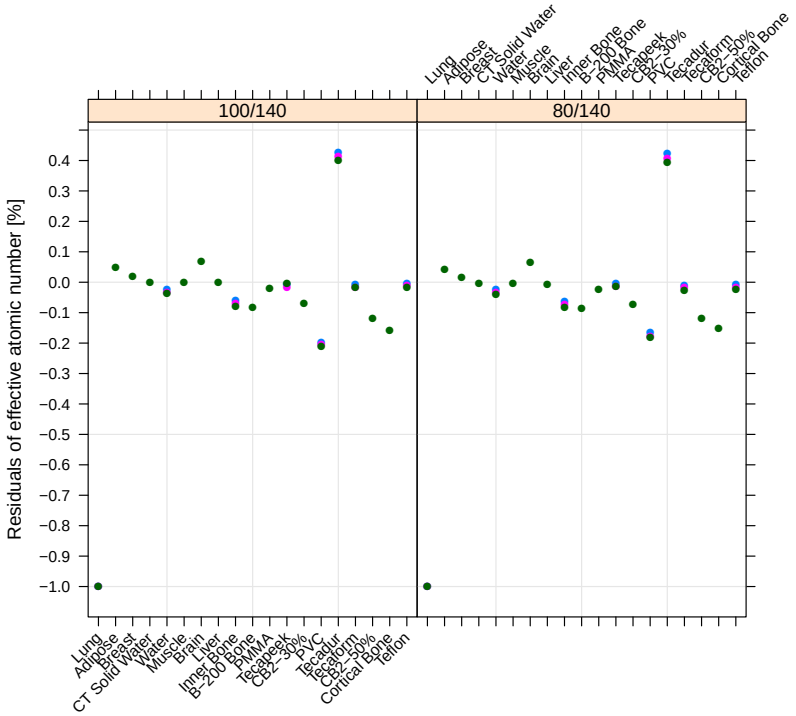

(b) Residuals of measured effective atomic number and reference value for 100/140 kV and 80/140 kV and the following phantom radii: 25 mm, 50 mm and 80 mm.

C Tables

Table C.1: CT numbers of all samples.

Material	Energy [kV]	Mode	Phantom radius [mm]	Mean CT Value	SD Mean CT Value	n Pixel
MCP-96	140	Dual 12 bit	80	3071.000	0.000	2068
MCP-96	80	Dual 12 bit	80	3071.000	0.000	2068
MCP-96	nA	Dual 12 bit	80	3071.000	0.000	2068
Al	140	Dual 12 bit	80	1769.620	12.276	2068
Al	80	Dual 12 bit	80	2762.428	24.856	2068
Al	nA	Dual 12 bit	80	2266.272	14.328	2068
Ti	140	Dual 12 bit	80	3071.000	0.000	2068
Ti	80	Dual 12 bit	80	3071.000	0.000	2068
Ti	nA	Dual 12 bit	80	3071.000	0.000	2068
Fe	140	Dual 12 bit	80	3071.000	0.000	2068
Fe	80	Dual 12 bit	80	3071.000	0.000	2068
Fe	nA	Dual 12 bit	80	3071.000	0.000	2068
Cu	140	Dual 12 bit	80	3071.000	0.000	2068
Cu	80	Dual 12 bit	80	3071.000	0.000	2068
Cu	nA	Dual 12 bit	80	3071.000	0.000	2068
Mo	140	Dual 12 bit	80	3071.000	0.000	2068
Mo	80	Dual 12 bit	80	3071.000	0.000	2068
Mo	nA	Dual 12 bit	80	3071.000	0.000	2068
Sn	140	Dual 12 bit	80	3071.000	0.000	2068
Sn	80	Dual 12 bit	80	3071.000	0.000	2068
Sn	nA	Dual 12 bit	80	3071.000	0.000	2068
W	140	Dual 12 bit	80	3071.000	0.000	2068
W	80	Dual 12 bit	80	3071.000	0.000	2068
W	nA	Dual 12 bit	80	3071.000	0.000	2068
MCP-96	100	Dual 12 bit	80	3071.000	0.000	2068
MCP-96	140	Dual 12 bit	80	3071.000	0.000	2068
MCP-96	nA	Dual 12 bit	80	3071.000	0.000	2068
Al	100	Dual 12 bit	80	2374.336	17.327	2068
Al	140	Dual 12 bit	80	1772.643	9.258	2068
Al	nA	Dual 12 bit	80	2073.742	10.931	2068
Ti	100	Dual 12 bit	80	3071.000	0.000	2068
Ti	140	Dual 12 bit	80	3071.000	0.000	2068
Ti	nA	Dual 12 bit	80	3071.000	0.000	2068
Fe	100	Dual 12 bit	80	3071.000	0.000	2068
Fe	140	Dual 12 bit	80	3071.000	0.000	2068
Fe	nA	Dual 12 bit	80	3071.000	0.000	2068
Cu	100	Dual 12 bit	80	3070.556	1.317	2068
Cu	140	Dual 12 bit	80	3070.735	0.616	2068
Cu	nA	Dual 12 bit	80	3070.745	0.660	2068
Mo	100	Dual 12 bit	80	3071.000	0.000	2068
Mo	140	Dual 12 bit	80	3071.000	0.000	2068
Mo	nA	Dual 12 bit	80	3071.000	0.000	2068
Sn	100	Dual 12 bit	80	3071.000	0.000	2068
Sn	140	Dual 12 bit	80	3071.000	0.000	2068
Sn	nA	Dual 12 bit	80	3071.000	0.000	2068
W	100	Dual 12 bit	80	3071.000	0.000	2068
W	140	Dual 12 bit	80	3071.000	0.000	2068
W	nA	Dual 12 bit	80	3071.000	0.000	2068
MCP-96	140	Dual 12 bit	80	3071.000	0.000	6721
MCP-96	80	Dual 12 bit	80	3071.000	0.000	6721
MCP-96	nA	Dual 12 bit	80	3071.000	0.000	6721
Al	140	Dual 12 bit	80	1772.543	11.489	9306
Al	80	Dual 12 bit	80	2736.600	28.264	9306
Al	nA	Dual 12 bit	80	2254.827	16.657	9306
Ti	140	Dual 12 bit	80	3071.000	0.000	9823
Ti	80	Dual 12 bit	80	3071.000	0.000	9823
Ti	nA	Dual 12 bit	80	3071.000	0.000	9823
Fe	140	Dual 12 bit	80	3071.000	0.000	8272
Fe	80	Dual 12 bit	80	3071.000	0.000	8272
Fe	nA	Dual 12 bit	80	3071.000	0.000	8272
Cu	140	Dual 12 bit	80	3071.000	0.000	10340
Cu	80	Dual 12 bit	80	3071.000	0.000	10340
Cu	nA	Dual 12 bit	80	3071.000	0.000	10340
Mo	140	Dual 12 bit	80	3071.000	0.000	9823
Mo	80	Dual 12 bit	80	3071.000	0.000	9823
Mo	nA	Dual 12 bit	80	3071.000	0.000	9823
Sn	140	Dual 12 bit	80	3071.000	0.000	9306
Sn	80	Dual 12 bit	80	3071.000	0.000	9306
Sn	nA	Dual 12 bit	80	3071.000	0.000	9306
W	140	Dual 12 bit	80	3071.000	0.000	6204
W	80	Dual 12 bit	80	3071.000	0.000	6204

W	nA	Dual 12 bit	80	3071.000	0.000	6204
MCP-96	100	Dual 12 bit	80	3071.000	0.000	6721
MCP-96	140	Dual 12 bit	80	3071.000	0.000	6721
MCP-96	nA	Dual 12 bit	80	3071.000	0.000	6721
Al	100	Dual 12 bit	80	2362.391	19.833	9306
Al	140	Dual 12 bit	80	1770.828	9.946	9306
Al	nA	Dual 12 bit	80	2066.864	12.403	9306
Ti	100	Dual 12 bit	80	3071.000	0.000	9823
Ti	140	Dual 12 bit	80	3071.000	0.000	9823
Ti	nA	Dual 12 bit	80	3071.000	0.000	9823
Fe	100	Dual 12 bit	80	3071.000	0.000	8272
Fe	140	Dual 12 bit	80	3071.000	0.000	8272
Fe	nA	Dual 12 bit	80	3071.000	0.000	8272
Cu	100	Dual 12 bit	80	3071.000	0.000	10340
Cu	140	Dual 12 bit	80	3071.000	0.000	10340
Cu	nA	Dual 12 bit	80	3071.000	0.000	10340
Mo	100	Dual 12 bit	80	3071.000	0.000	9823
Mo	140	Dual 12 bit	80	3071.000	0.000	9823
Mo	nA	Dual 12 bit	80	3071.000	0.000	9823
Sn	100	Dual 12 bit	80	3071.000	0.000	9306
Sn	140	Dual 12 bit	80	3071.000	0.000	9306
Sn	nA	Dual 12 bit	80	3071.000	0.000	9306
W	100	Dual 12 bit	80	3071.000	0.000	6204
W	140	Dual 12 bit	80	3071.000	0.000	6204
W	nA	Dual 12 bit	80	3071.000	0.000	6204
Lung	140	Dual 12 bit	80	-555.610	27.964	6204
Lung	80	Dual 12 bit	80	-553.246	27.476	6204
Lung	nA	Dual 12 bit	80	-554.182	27.147	6204
Adipose	140	Dual 12 bit	80	-85.214	8.416	8272
Adipose	80	Dual 12 bit	80	-124.690	7.929	8272
Adipose	nA	Dual 12 bit	80	-104.703	5.909	8272
Breast	140	Dual 12 bit	80	-39.104	8.762	8789
Breast	80	Dual 12 bit	80	-60.236	8.134	8789
Breast	nA	Dual 12 bit	80	-49.422	6.027	8789
CT Solid Water	140	Dual 12 bit	80	-1.034	9.124	7755
CT Solid Water	80	Dual 12 bit	80	7.392	8.034	7755
CT Solid Water	nA	Dual 12 bit	80	3.425	6.248	7755
Muscle	140	Dual 12 bit	80	28.999	9.507	8272
Muscle	80	Dual 12 bit	80	38.184	9.028	8272
Muscle	nA	Dual 12 bit	80	33.843	7.154	8272
Brain	140	Dual 12 bit	80	31.915	8.753	8789
Brain	80	Dual 12 bit	80	-8.487	7.836	8789
Brain	nA	Dual 12 bit	80	11.967	5.831	8789
Liver	140	Dual 12 bit	80	68.989	8.912	8272
Liver	80	Dual 12 bit	80	77.558	8.412	8272
Liver	nA	Dual 12 bit	80	73.527	6.461	8272
Water	140	Dual 12 bit	80	-0.138	9.318	2068
Water	80	Dual 12 bit	80	-1.846	8.068	2068
Water	nA	Dual 12 bit	80	-0.747	6.098	2068
Lung	100	Dual 12 bit	80	-555.435	27.364	6204
Lung	140	Dual 12 bit	80	-555.936	27.373	6204
Lung	nA	Dual 12 bit	80	-555.436	27.055	6204
Adipose	100	Dual 12 bit	80	-109.573	5.394	8272
Adipose	140	Dual 12 bit	80	-85.507	6.565	8272
Adipose	nA	Dual 12 bit	80	-97.290	4.373	8272
Breast	100	Dual 12 bit	80	-51.890	5.391	8789
Breast	140	Dual 12 bit	80	-39.208	6.537	8789
Breast	nA	Dual 12 bit	80	-45.302	4.121	8789
CT Solid Water	100	Dual 12 bit	80	4.666	5.724	7755
CT Solid Water	140	Dual 12 bit	80	-1.397	6.399	7755
CT Solid Water	nA	Dual 12 bit	80	1.887	4.366	7755
Muscle	100	Dual 12 bit	80	35.565	7.013	8272
Muscle	140	Dual 12 bit	80	28.688	7.616	8272
Muscle	nA	Dual 12 bit	80	32.378	5.898	8272
Brain	100	Dual 12 bit	80	6.805	5.496	8789
Brain	140	Dual 12 bit	80	31.577	6.374	8789
Brain	nA	Dual 12 bit	80	19.435	4.216	8789
Liver	100	Dual 12 bit	80	74.936	6.116	8272
Liver	140	Dual 12 bit	80	68.011	7.030	8272
Liver	nA	Dual 12 bit	80	71.728	4.979	8272
Water	100	Dual 12 bit	80	-0.369	5.681	2068
Water	140	Dual 12 bit	80	-0.194	6.299	2068
Water	nA	Dual 12 bit	80	-0.037	4.274	2068
Inner Bone	140	Dual 12 bit	80	177.108	9.342	8272
Inner Bone	80	Dual 12 bit	80	350.913	11.223	8272
Inner Bone	nA	Dual 12 bit	80	264.261	7.431	8272
B-200 Bone	140	Dual 12 bit	80	185.850	9.678	7755
B-200 Bone	80	Dual 12 bit	80	358.934	11.166	7755
B-200 Bone	nA	Dual 12 bit	80	272.644	7.650	7755
CB2-30%	140	Dual 12 bit	80	390.924	10.025	8789
CB2-30%	80	Dual 12 bit	80	657.721	12.853	8789
CB2-30%	nA	Dual 12 bit	80	524.570	8.476	8789
CB2-50%	140	Dual 12 bit	80	697.434	10.852	7238
CB2-50%	80	Dual 12 bit	80	1208.796	16.027	7238
CB2-50%	nA	Dual 12 bit	80	953.364	9.812	7238
Cortical Bone	140	Dual 12 bit	80	1046.069	12.258	8789
Cortical Bone	80	Dual 12 bit	80	1816.020	22.485	8789
Cortical Bone	nA	Dual 12 bit	80	1431.294	13.725	8789
Inner Bone	100	Dual 12 bit	80	286.351	8.142	8272
Inner Bone	140	Dual 12 bit	80	176.724	6.671	8272

Inner Bone	nA	Dual 12 bit	80	231.790	5.495	8272
B-200 Bone	100	Dual 12 bit	80	295.437	7.934	7755
B-200 Bone	140	Dual 12 bit	80	185.486	6.973	7755
B-200 Bone	nA	Dual 12 bit	80	240.709	5.542	7755
CB2-30%	100	Dual 12 bit	80	558.796	8.534	8789
CB2-30%	140	Dual 12 bit	80	390.842	7.343	8789
CB2-30%	nA	Dual 12 bit	80	475.068	5.738	8789
CB2-50%	100	Dual 12 bit	80	1012.930	10.456	7238
CB2-50%	140	Dual 12 bit	80	696.195	7.788	7238
CB2-50%	nA	Dual 12 bit	80	854.813	6.562	7238
Cortical Bone	100	Dual 12 bit	80	1509.219	12.887	8272
Cortical Bone	140	Dual 12 bit	80	1043.903	8.724	8272
Cortical Bone	nA	Dual 12 bit	80	1276.811	8.119	8272
PMMA	140	Dual 12 bit	80	140.087	11.914	4653
PMMA	80	Dual 12 bit	80	99.820	10.848	4653
PMMA	nA	Dual 12 bit	80	120.205	7.825	4653
Tecapeek	140	Dual 12 bit	80	211.796	12.289	5170
Tecapeek	80	Dual 12 bit	80	161.864	11.054	5170
Tecapeek	nA	Dual 12 bit	80	187.080	8.335	5170
Tecadur	140	Dual 12 bit	80	421.001	18.752	4653
Tecadur	80	Dual 12 bit	80	578.642	21.453	4653
Tecadur	nA	Dual 12 bit	80	500.067	17.601	4653
Tecaform	140	Dual 12 bit	80	352.634	13.304	4653
Tecaform	80	Dual 12 bit	80	324.405	12.471	4653
Tecaform	nA	Dual 12 bit	80	338.773	8.486	4653
Teflon	140	Dual 12 bit	80	901.954	15.235	5170
Teflon	80	Dual 12 bit	80	972.606	17.061	5170
Teflon	nA	Dual 12 bit	80	937.535	11.711	5170
PVC	140	Dual 12 bit	80	1378.128	19.214	4136
PVC	80	Dual 12 bit	80	1982.872	26.772	4136
PVC	nA	Dual 12 bit	80	1680.743	17.883	4136
PMMA	100	Dual 12 bit	80	115.660	6.666	4653
PMMA	140	Dual 12 bit	80	140.310	8.096	4653
PMMA	nA	Dual 12 bit	80	128.233	5.320	4653
Tecapeek	100	Dual 12 bit	80	181.160	7.045	4653
Tecapeek	140	Dual 12 bit	80	211.146	8.457	4653
Tecapeek	nA	Dual 12 bit	80	196.396	5.448	4653
Tecadur	100	Dual 12 bit	80	521.022	17.494	5170
Tecadur	140	Dual 12 bit	80	419.597	16.354	5170
Tecadur	nA	Dual 12 bit	80	470.552	15.603	5170
Tecaform	100	Dual 12 bit	80	336.649	9.177	5687
Tecaform	140	Dual 12 bit	80	351.120	8.740	5687
Tecaform	nA	Dual 12 bit	80	344.137	6.408	5687
Teflon	100	Dual 12 bit	80	949.044	12.328	4653
Teflon	140	Dual 12 bit	80	903.869	10.149	4653
Teflon	nA	Dual 12 bit	80	926.703	7.884	4653
PVC	100	Dual 12 bit	80	1702.436	18.432	3619
PVC	140	Dual 12 bit	80	1377.831	14.258	3619
PVC	nA	Dual 12 bit	80	1540.383	13.494	3619
MCP-96	140	Dual 12 bit	14	3071.000	0.000	2068
MCP-96	80	Dual 12 bit	14	3071.000	0.000	2068
MCP-96	nA	Dual 12 bit	14	3071.000	0.000	2068
Al	140	Dual 12 bit	14	1802.205	7.250	2068
Al	80	Dual 12 bit	14	2950.448	26.622	2068
Al	nA	Dual 12 bit	14	2376.571	14.655	2068
Ti	140	Dual 12 bit	14	3071.000	0.000	2068
Ti	80	Dual 12 bit	14	3071.000	0.000	2068
Ti	nA	Dual 12 bit	14	3071.000	0.000	2068
Fe	140	Dual 12 bit	14	3071.000	0.000	2068
Fe	80	Dual 12 bit	14	3071.000	0.000	2068
Fe	nA	Dual 12 bit	14	3071.000	0.000	2068
Cu	140	Dual 12 bit	14	3071.000	0.000	2068
Cu	80	Dual 12 bit	14	3071.000	0.000	2068
Cu	nA	Dual 12 bit	14	3071.000	0.000	2068
Mo	140	Dual 12 bit	14	3071.000	0.000	2068
Mo	80	Dual 12 bit	14	3071.000	0.000	2068
Mo	nA	Dual 12 bit	14	3071.000	0.000	2068
Sn	140	Dual 12 bit	14	3071.000	0.000	2068
Sn	80	Dual 12 bit	14	3071.000	0.000	2068
Sn	nA	Dual 12 bit	14	3071.000	0.000	2068
W	140	Dual 12 bit	14	3071.000	0.000	2068
W	80	Dual 12 bit	14	3071.000	0.000	2068
W	nA	Dual 12 bit	14	3071.000	0.000	2068
MCP-96	100	Dual 12 bit	14	3071.000	0.000	2068
MCP-96	140	Dual 12 bit	14	3071.000	0.000	2068
MCP-96	nA	Dual 12 bit	14	3071.000	0.000	2068
Al	100	Dual 12 bit	14	2530.421	20.315	2068
Al	140	Dual 12 bit	14	1804.236	6.811	2068
Al	nA	Dual 12 bit	14	2167.584	11.873	2068
Ti	100	Dual 12 bit	14	3071.000	0.000	2068
Ti	140	Dual 12 bit	14	3071.000	0.000	2068
Ti	nA	Dual 12 bit	14	3071.000	0.000	2068
Fe	100	Dual 12 bit	14	3071.000	0.000	2068
Fe	140	Dual 12 bit	14	3071.000	0.000	2068
Fe	nA	Dual 12 bit	14	3071.000	0.000	2068
Cu	100	Dual 12 bit	14	3071.000	0.000	2068
Cu	140	Dual 12 bit	14	3071.000	0.000	2068
Cu	nA	Dual 12 bit	14	3071.000	0.000	2068
Mo	100	Dual 12 bit	14	3071.000	0.000	2068
Mo	140	Dual 12 bit	14	3071.000	0.000	2068

Mo	nA	Dual 12 bit	14	3071.000	0.000	2068
Sn	100	Dual 12 bit	14	3071.000	0.000	2068
Sn	140	Dual 12 bit	14	3071.000	0.000	2068
Sn	nA	Dual 12 bit	14	3071.000	0.000	2068
W	100	Dual 12 bit	14	3071.000	0.000	2068
W	140	Dual 12 bit	14	3071.000	0.000	2068
W	nA	Dual 12 bit	14	3071.000	0.000	2068
MCP-96	140	Dual 12 bit	14	3071.000	0.000	8789
MCP-96	80	Dual 12 bit	14	3071.000	0.000	8789
MCP-96	nA	Dual 12 bit	14	3071.000	0.000	8789
Al	140	Dual 12 bit	14	1802.685	7.279	8272
Al	80	Dual 12 bit	14	2901.135	27.260	8272
Al	nA	Dual 12 bit	14	2352.163	15.857	8272
Ti	140	Dual 12 bit	14	3071.000	0.000	8789
Ti	80	Dual 12 bit	14	3071.000	0.000	8789
Ti	nA	Dual 12 bit	14	3071.000	0.000	8789
Fe	140	Dual 12 bit	14	3071.000	0.000	8272
Fe	80	Dual 12 bit	14	3071.000	0.000	8272
Fe	nA	Dual 12 bit	14	3071.000	0.000	8272
Cu	140	Dual 12 bit	14	3071.000	0.000	8272
Cu	80	Dual 12 bit	14	3071.000	0.000	8272
Cu	nA	Dual 12 bit	14	3071.000	0.000	8272
Mo	140	Dual 12 bit	14	3071.000	0.000	8789
Mo	80	Dual 12 bit	14	3071.000	0.000	8789
Mo	nA	Dual 12 bit	14	3071.000	0.000	8789
Sn	140	Dual 12 bit	14	3071.000	0.000	8789
Sn	80	Dual 12 bit	14	3071.000	0.000	8789
Sn	nA	Dual 12 bit	14	3071.000	0.000	8789
W	140	Dual 12 bit	14	3071.000	0.000	8272
W	80	Dual 12 bit	14	3071.000	0.000	8272
W	nA	Dual 12 bit	14	3071.000	0.000	8272
MCP-96	100	Dual 12 bit	14	3071.000	0.000	8789
MCP-96	140	Dual 12 bit	14	3071.000	0.000	8789
MCP-96	nA	Dual 12 bit	14	3071.000	0.000	8789
Al	100	Dual 12 bit	14	2502.654	21.092	8272
Al	140	Dual 12 bit	14	1798.493	6.822	8272
Al	nA	Dual 12 bit	14	2150.820	12.787	8272
Ti	100	Dual 12 bit	14	3071.000	0.000	8789
Ti	140	Dual 12 bit	14	3071.000	0.000	8789
Ti	nA	Dual 12 bit	14	3071.000	0.000	8789
Fe	100	Dual 12 bit	14	3071.000	0.000	8789
Fe	140	Dual 12 bit	14	3071.000	0.000	8789
Fe	nA	Dual 12 bit	14	3071.000	0.000	8789
Cu	100	Dual 12 bit	14	3071.000	0.000	8272
Cu	140	Dual 12 bit	14	3071.000	0.000	8272
Cu	nA	Dual 12 bit	14	3071.000	0.000	8272
Mo	100	Dual 12 bit	14	3071.000	0.000	8789
Mo	140	Dual 12 bit	14	3071.000	0.000	8789
Mo	nA	Dual 12 bit	14	3071.000	0.000	8789
Sn	100	Dual 12 bit	14	3071.000	0.000	8789
Sn	140	Dual 12 bit	14	3071.000	0.000	8789
Sn	nA	Dual 12 bit	14	3071.000	0.000	8789
W	100	Dual 12 bit	14	3071.000	0.000	7755
W	140	Dual 12 bit	14	3071.000	0.000	7755
W	nA	Dual 12 bit	14	3071.000	0.000	7755
MCP-96	140	Dual 12 bit	25	3071.000	0.000	2068
MCP-96	80	Dual 12 bit	25	3071.000	0.000	2068
MCP-96	nA	Dual 12 bit	25	3071.000	0.000	2068
Al	140	Dual 12 bit	25	1791.985	7.530	2068
Al	80	Dual 12 bit	25	2906.297	24.620	2068
Al	nA	Dual 12 bit	25	2349.396	13.978	2068
Ti	140	Dual 12 bit	25	3071.000	0.000	2068
Ti	80	Dual 12 bit	25	3071.000	0.000	2068
Ti	nA	Dual 12 bit	25	3071.000	0.000	2068
Fe	140	Dual 12 bit	25	3071.000	0.000	2068
Fe	80	Dual 12 bit	25	3071.000	0.000	2068
Fe	nA	Dual 12 bit	25	3071.000	0.000	2068
Cu	140	Dual 12 bit	25	3071.000	0.000	2068
Cu	80	Dual 12 bit	25	3071.000	0.000	2068
Cu	nA	Dual 12 bit	25	3071.000	0.000	2068
Mo	140	Dual 12 bit	25	3071.000	0.000	2068
Mo	80	Dual 12 bit	25	3071.000	0.000	2068
Mo	nA	Dual 12 bit	25	3071.000	0.000	2068
Sn	140	Dual 12 bit	25	3071.000	0.000	2068
Sn	80	Dual 12 bit	25	3071.000	0.000	2068
Sn	nA	Dual 12 bit	25	3071.000	0.000	2068
W	140	Dual 12 bit	25	3071.000	0.000	2068
W	80	Dual 12 bit	25	3071.000	0.000	2068
W	nA	Dual 12 bit	25	3071.000	0.000	2068
MCP-96	100	Dual 12 bit	25	3071.000	0.000	2068
MCP-96	140	Dual 12 bit	25	3071.000	0.000	2068
MCP-96	nA	Dual 12 bit	25	3071.000	0.000	2068
Al	100	Dual 12 bit	25	2491.688	19.100	2068
Al	140	Dual 12 bit	25	1794.556	6.933	2068
Al	nA	Dual 12 bit	25	2143.371	11.672	2068
Ti	100	Dual 12 bit	25	3071.000	0.000	2068
Ti	140	Dual 12 bit	25	3071.000	0.000	2068
Ti	nA	Dual 12 bit	25	3071.000	0.000	2068
Fe	100	Dual 12 bit	25	3071.000	0.000	2068
Fe	140	Dual 12 bit	25	3071.000	0.000	2068

Fe	nA	Dual 12 bit	25	3071.000	0.000	2068
Cu	100	Dual 12 bit	25	3071.000	0.000	2068
Cu	140	Dual 12 bit	25	3071.000	0.000	2068
Cu	nA	Dual 12 bit	25	3071.000	0.000	2068
Mo	100	Dual 12 bit	25	3071.000	0.000	2068
Mo	140	Dual 12 bit	25	3071.000	0.000	2068
Mo	nA	Dual 12 bit	25	3071.000	0.000	2068
Sn	100	Dual 12 bit	25	3071.000	0.000	2068
Sn	140	Dual 12 bit	25	3071.000	0.000	2068
Sn	nA	Dual 12 bit	25	3071.000	0.000	2068
W	100	Dual 12 bit	25	3071.000	0.000	2068
W	140	Dual 12 bit	25	3071.000	0.000	2068
W	nA	Dual 12 bit	25	3071.000	0.000	2068
MCP-96	140	Dual 12 bit	25	3071.000	0.000	8272
MCP-96	80	Dual 12 bit	25	3071.000	0.000	8272
MCP-96	nA	Dual 12 bit	25	3071.000	0.000	8272
Al	140	Dual 12 bit	25	1794.190	8.046	8789
Al	80	Dual 12 bit	25	2861.925	28.339	8789
Al	nA	Dual 12 bit	25	2328.309	16.739	8789
Ti	140	Dual 12 bit	25	3071.000	0.000	9823
Ti	80	Dual 12 bit	25	3071.000	0.000	9823
Ti	nA	Dual 12 bit	25	3071.000	0.000	9823
Fe	140	Dual 12 bit	25	3071.000	0.000	9823
Fe	80	Dual 12 bit	25	3071.000	0.000	9823
Fe	nA	Dual 12 bit	25	3071.000	0.000	9823
Cu	140	Dual 12 bit	25	3071.000	0.000	9306
Cu	80	Dual 12 bit	25	3071.000	0.000	9306
Cu	nA	Dual 12 bit	25	3071.000	0.000	9306
Mo	140	Dual 12 bit	25	3071.000	0.000	7755
Mo	80	Dual 12 bit	25	3071.000	0.000	7755
Mo	nA	Dual 12 bit	25	3071.000	0.000	7755
Sn	140	Dual 12 bit	25	3071.000	0.000	8272
Sn	80	Dual 12 bit	25	3071.000	0.000	8272
Sn	nA	Dual 12 bit	25	3071.000	0.000	8272
W	140	Dual 12 bit	25	3071.000	0.000	7755
W	80	Dual 12 bit	25	3071.000	0.000	7755
W	nA	Dual 12 bit	25	3071.000	0.000	7755
MCP-96	100	Dual 12 bit	25	3071.000	0.000	8789
MCP-96	140	Dual 12 bit	25	3071.000	0.000	8789
MCP-96	nA	Dual 12 bit	25	3071.000	0.000	8789
Al	100	Dual 12 bit	25	2468.958	21.932	8789
Al	140	Dual 12 bit	25	1790.669	7.691	8789
Al	nA	Dual 12 bit	25	2130.062	13.788	8789
Ti	100	Dual 12 bit	25	3071.000	0.000	9823
Ti	140	Dual 12 bit	25	3071.000	0.000	9823
Ti	nA	Dual 12 bit	25	3071.000	0.000	9823
Fe	100	Dual 12 bit	25	3071.000	0.000	9823
Fe	140	Dual 12 bit	25	3071.000	0.000	9823
Fe	nA	Dual 12 bit	25	3071.000	0.000	9823
Cu	100	Dual 12 bit	25	3071.000	0.000	9306
Cu	140	Dual 12 bit	25	3071.000	0.000	9306
Cu	nA	Dual 12 bit	25	3071.000	0.000	9306
Mo	100	Dual 12 bit	25	3071.000	0.000	7755
Mo	140	Dual 12 bit	25	3071.000	0.000	7755
Mo	nA	Dual 12 bit	25	3071.000	0.000	7755
Sn	100	Dual 12 bit	25	3071.000	0.000	8272
Sn	140	Dual 12 bit	25	3071.000	0.000	8272
Sn	nA	Dual 12 bit	25	3071.000	0.000	8272
W	100	Dual 12 bit	25	3071.000	0.000	7755
W	140	Dual 12 bit	25	3071.000	0.000	7755
W	nA	Dual 12 bit	25	3071.000	0.000	7755
MCP-96	140	Dual 12 bit	50	3071.000	0.000	2068
MCP-96	80	Dual 12 bit	50	3071.000	0.000	2068
MCP-96	nA	Dual 12 bit	50	3071.000	0.000	2068
Al	140	Dual 12 bit	50	1778.679	7.932	2068
Al	80	Dual 12 bit	50	2831.803	22.036	2068
Al	nA	Dual 12 bit	50	2305.488	12.673	2068
Ti	140	Dual 12 bit	50	3071.000	0.000	2068
Ti	80	Dual 12 bit	50	3071.000	0.000	2068
Ti	nA	Dual 12 bit	50	3071.000	0.000	2068
Fe	140	Dual 12 bit	50	3071.000	0.000	2068
Fe	80	Dual 12 bit	50	3071.000	0.000	2068
Fe	nA	Dual 12 bit	50	3071.000	0.000	2068
Cu	140	Dual 12 bit	50	3071.000	0.000	2068
Cu	80	Dual 12 bit	50	3071.000	0.000	2068
Cu	nA	Dual 12 bit	50	3071.000	0.000	2068
Mo	140	Dual 12 bit	50	3071.000	0.000	2068
Mo	80	Dual 12 bit	50	3071.000	0.000	2068
Mo	nA	Dual 12 bit	50	3071.000	0.000	2068
Sn	140	Dual 12 bit	50	3071.000	0.000	2068
Sn	80	Dual 12 bit	50	3071.000	0.000	2068
Sn	nA	Dual 12 bit	50	3071.000	0.000	2068
W	140	Dual 12 bit	50	3071.000	0.000	2068
W	80	Dual 12 bit	50	3071.000	0.000	2068
W	nA	Dual 12 bit	50	3071.000	0.000	2068
MCP-96	100	Dual 12 bit	50	3071.000	0.000	2068
MCP-96	140	Dual 12 bit	50	3071.000	0.000	2068
MCP-96	nA	Dual 12 bit	50	3071.000	0.000	2068
Al	100	Dual 12 bit	50	2428.248	16.856	2068
Al	140	Dual 12 bit	50	1781.520	7.364	2068

Al	nA	Dual 12 bit	50	2105.131	10.496	2068
Ti	100	Dual 12 bit	50	3071.000	0.000	2068
Ti	140	Dual 12 bit	50	3071.000	0.000	2068
Ti	nA	Dual 12 bit	50	3071.000	0.000	2068
Fe	100	Dual 12 bit	50	3071.000	0.000	2068
Fe	140	Dual 12 bit	50	3071.000	0.000	2068
Fe	nA	Dual 12 bit	50	3071.000	0.000	2068
Cu	100	Dual 12 bit	50	3071.000	0.000	2068
Cu	140	Dual 12 bit	50	3071.000	0.000	2068
Cu	nA	Dual 12 bit	50	3071.000	0.000	2068
Mo	100	Dual 12 bit	50	3071.000	0.000	2068
Mo	140	Dual 12 bit	50	3071.000	0.000	2068
Mo	nA	Dual 12 bit	50	3071.000	0.000	2068
Sn	100	Dual 12 bit	50	3071.000	0.000	2068
Sn	140	Dual 12 bit	50	3071.000	0.000	2068
Sn	nA	Dual 12 bit	50	3071.000	0.000	2068
W	100	Dual 12 bit	50	3071.000	0.000	2068
W	140	Dual 12 bit	50	3071.000	0.000	2068
W	nA	Dual 12 bit	50	3071.000	0.000	2068
MCP-96	140	Dual 12 bit	50	3071.000	0.000	8272
MCP-96	80	Dual 12 bit	50	3071.000	0.000	8272
MCP-96	nA	Dual 12 bit	50	3071.000	0.000	8272
Al	140	Dual 12 bit	50	1781.551	10.359	8272
Al	80	Dual 12 bit	50	2791.875	26.553	8272
Al	nA	Dual 12 bit	50	2286.964	15.707	8272
Ti	140	Dual 12 bit	50	3071.000	0.000	8789
Ti	80	Dual 12 bit	50	3071.000	0.000	8789
Ti	nA	Dual 12 bit	50	3071.000	0.000	8789
Fe	140	Dual 12 bit	50	3071.000	0.000	7238
Fe	80	Dual 12 bit	50	3071.000	0.000	7238
Fe	nA	Dual 12 bit	50	3071.000	0.000	7238
Cu	140	Dual 12 bit	50	3071.000	0.000	7755
Cu	80	Dual 12 bit	50	3071.000	0.000	7755
Cu	nA	Dual 12 bit	50	3071.000	0.000	7755
Mo	140	Dual 12 bit	50	3071.000	0.000	8789
Mo	80	Dual 12 bit	50	3071.000	0.000	8789
Mo	nA	Dual 12 bit	50	3071.000	0.000	8789
Sn	140	Dual 12 bit	50	3071.000	0.000	8272
Sn	80	Dual 12 bit	50	3071.000	0.000	8272
Sn	nA	Dual 12 bit	50	3071.000	0.000	8272
W	140	Dual 12 bit	50	3071.000	0.000	7238
W	80	Dual 12 bit	50	3071.000	0.000	7238
W	nA	Dual 12 bit	50	3071.000	0.000	7238
MCP-96	100	Dual 12 bit	50	3071.000	0.000	8272
MCP-96	140	Dual 12 bit	50	3071.000	0.000	8272
MCP-96	nA	Dual 12 bit	50	3071.000	0.000	8272
Al	100	Dual 12 bit	50	2411.016	19.398	8272
Al	140	Dual 12 bit	50	1780.826	8.620	8272
Al	nA	Dual 12 bit	50	2096.172	12.266	8272
Ti	100	Dual 12 bit	50	3071.000	0.000	8789
Ti	140	Dual 12 bit	50	3071.000	0.000	8789
Ti	nA	Dual 12 bit	50	3071.000	0.000	8789
Fe	100	Dual 12 bit	50	3071.000	0.000	7238
Fe	140	Dual 12 bit	50	3071.000	0.000	7238
Fe	nA	Dual 12 bit	50	3071.000	0.000	7238
Cu	100	Dual 12 bit	50	3071.000	0.000	7755
Cu	140	Dual 12 bit	50	3071.000	0.000	7755
Cu	nA	Dual 12 bit	50	3071.000	0.000	7755
Mo	100	Dual 12 bit	50	3071.000	0.000	8789
Mo	140	Dual 12 bit	50	3071.000	0.000	8789
Mo	nA	Dual 12 bit	50	3071.000	0.000	8789
Sn	100	Dual 12 bit	50	3071.000	0.000	8272
Sn	140	Dual 12 bit	50	3071.000	0.000	8272
Sn	nA	Dual 12 bit	50	3071.000	0.000	8272
W	100	Dual 12 bit	50	3071.000	0.000	7238
W	140	Dual 12 bit	50	3071.000	0.000	7238
W	nA	Dual 12 bit	50	3071.000	0.000	7238
Water	140	Dual 12 bit	50	-9.353	6.753	3619
Water	80	Dual 12 bit	50	-9.254	5.233	3619
Water	nA	Dual 12 bit	50	-9.056	4.316	3619
Inner Bone	140	Dual 12 bit	50	171.391	7.248	7755
Inner Bone	80	Dual 12 bit	50	360.031	6.948	7755
Inner Bone	nA	Dual 12 bit	50	265.965	5.128	7755
Lung	140	Dual 12 bit	50	-563.193	29.006	8272
Lung	80	Dual 12 bit	50	-558.446	28.879	8272
Lung	nA	Dual 12 bit	50	-560.566	28.630	8272
Water	100	Dual 12 bit	50	-9.738	3.877	3619
Water	140	Dual 12 bit	50	-9.181	4.622	3619
Water	nA	Dual 12 bit	50	-9.203	3.175	3619
Inner Bone	100	Dual 12 bit	50	290.975	5.300	7755
Inner Bone	140	Dual 12 bit	50	170.970	5.312	7755
Inner Bone	nA	Dual 12 bit	50	231.225	4.050	7755
Lung	100	Dual 12 bit	50	-561.539	28.322	8272
Lung	140	Dual 12 bit	50	-563.126	27.904	8272
Lung	nA	Dual 12 bit	50	-562.085	27.920	8272
Water	140	Dual 12 bit	25	-11.921	4.206	4653
Water	80	Dual 12 bit	25	-8.662	3.406	4653
Water	nA	Dual 12 bit	25	-10.046	2.640	4653
Inner Bone	140	Dual 12 bit	25	171.750	4.661	8272
Inner Bone	80	Dual 12 bit	25	374.812	4.726	8272

Inner Bone	nA	Dual 12 bit	25	273.533	3.654	8272
Lung	140	Dual 12 bit	25	-564.389	26.456	8789
Lung	80	Dual 12 bit	25	-557.554	26.775	8789
Lung	nA	Dual 12 bit	25	-560.718	26.427	8789
Water	100	Dual 12 bit	25	-9.747	2.759	4653
Water	140	Dual 12 bit	25	-12.117	2.961	4653
Water	nA	Dual 12 bit	25	-10.685	2.046	4653
Inner Bone	100	Dual 12 bit	25	303.945	3.984	8272
Inner Bone	140	Dual 12 bit	25	171.223	3.863	8272
Inner Bone	nA	Dual 12 bit	25	237.829	3.234	8272
Lung	100	Dual 12 bit	25	-560.700	26.879	8789
Lung	140	Dual 12 bit	25	-564.618	26.316	8789
Lung	nA	Dual 12 bit	25	-562.407	26.458	8789
Tecapeek	140	Dual 12 bit	25	195.933	4.592	3102
Tecapeek	80	Dual 12 bit	25	146.280	3.461	3102
Tecapeek	nA	Dual 12 bit	25	171.350	2.798	3102
Tecadur	140	Dual 12 bit	25	411.068	15.129	5170
Tecadur	80	Dual 12 bit	25	598.217	16.795	5170
Tecadur	nA	Dual 12 bit	25	504.884	15.617	5170
Tecaform	140	Dual 12 bit	25	336.274	4.767	4653
Tecaform	80	Dual 12 bit	25	313.496	3.898	4653
Tecaform	nA	Dual 12 bit	25	325.140	2.985	4653
Teflon	140	Dual 12 bit	25	888.573	5.240	5170
Teflon	80	Dual 12 bit	25	977.958	4.890	5170
Teflon	nA	Dual 12 bit	25	933.515	3.632	5170
PVC	140	Dual 12 bit	25	1379.965	8.704	5170
PVC	80	Dual 12 bit	25	2070.842	10.016	5170
PVC	nA	Dual 12 bit	25	1725.660	7.806	5170
Tecapeek	100	Dual 12 bit	25	163.017	2.883	3102
Tecapeek	140	Dual 12 bit	25	195.918	3.324	3102
Tecapeek	nA	Dual 12 bit	25	179.720	2.291	3102
Tecadur	100	Dual 12 bit	25	532.485	15.838	5170
Tecadur	140	Dual 12 bit	25	410.695	14.832	5170
Tecadur	nA	Dual 12 bit	25	471.842	15.133	5170
Tecaform	100	Dual 12 bit	25	321.820	3.113	4653
Tecaform	140	Dual 12 bit	25	336.101	3.563	4653
Tecaform	nA	Dual 12 bit	25	329.211	2.499	4653
Teflon	100	Dual 12 bit	25	946.424	4.287	5170
Teflon	140	Dual 12 bit	25	888.553	4.063	5170
Teflon	nA	Dual 12 bit	25	917.740	2.925	5170
PVC	100	Dual 12 bit	25	1761.033	8.077	5170
PVC	140	Dual 12 bit	25	1377.635	7.608	5170
PVC	nA	Dual 12 bit	25	1569.586	6.923	5170
Tecapeek	140	Dual 12 bit	50	202.481	6.627	4653
Tecapeek	80	Dual 12 bit	50	151.395	5.529	4653
Tecapeek	nA	Dual 12 bit	50	177.186	4.318	4653
Tecadur	140	Dual 12 bit	50	413.503	15.602	5170
Tecadur	80	Dual 12 bit	50	585.557	17.117	5170
Tecadur	nA	Dual 12 bit	50	499.773	15.466	5170
Tecaform	140	Dual 12 bit	50	341.294	7.512	4136
Tecaform	80	Dual 12 bit	50	316.490	6.416	4136
Tecaform	nA	Dual 12 bit	50	329.144	4.956	4136
Teflon	140	Dual 12 bit	50	894.326	8.266	5170
Teflon	80	Dual 12 bit	50	972.854	8.278	5170
Teflon	nA	Dual 12 bit	50	933.840	5.924	5170
PVC	140	Dual 12 bit	50	1376.181	11.458	5170
PVC	80	Dual 12 bit	50	2021.501	13.324	5170
PVC	nA	Dual 12 bit	50	1699.092	9.660	5170
Tecapeek	100	Dual 12 bit	50	169.204	4.169	4653
Tecapeek	140	Dual 12 bit	50	201.731	5.006	4653
Tecapeek	nA	Dual 12 bit	50	185.716	3.307	4653
Tecadur	100	Dual 12 bit	50	523.694	16.076	5170
Tecadur	140	Dual 12 bit	50	412.596	14.681	5170
Tecadur	nA	Dual 12 bit	50	468.391	14.838	5170
Tecaform	100	Dual 12 bit	50	325.368	4.641	4136
Tecaform	140	Dual 12 bit	50	340.730	5.290	4136
Tecaform	nA	Dual 12 bit	50	333.305	3.463	4136
Teflon	100	Dual 12 bit	50	945.540	6.456	5170
Teflon	140	Dual 12 bit	50	893.336	5.796	5170
Teflon	nA	Dual 12 bit	50	919.691	4.353	5170
PVC	100	Dual 12 bit	50	1727.468	10.013	5170
PVC	140	Dual 12 bit	50	1373.531	9.140	5170
PVC	nA	Dual 12 bit	50	1550.747	7.886	5170
Solution 1	140	Dual 12 bit	80	13.900	7.672	4136
Solution 1	80	Dual 12 bit	80	22.381	6.879	4136
Solution 1	nA	Dual 12 bit	80	18.394	5.247	4136
Solution 2	140	Dual 12 bit	80	37.456	7.646	4136
Solution 2	80	Dual 12 bit	80	66.913	6.802	4136
Solution 2	nA	Dual 12 bit	80	52.438	5.042	4136
Solution 3	140	Dual 12 bit	80	64.649	7.654	4653
Solution 3	80	Dual 12 bit	80	117.805	7.076	4653
Solution 3	nA	Dual 12 bit	80	91.480	5.349	4653
Solution 4	140	Dual 12 bit	80	96.411	7.795	1034
Solution 4	80	Dual 12 bit	80	181.089	6.880	1034
Solution 4	nA	Dual 12 bit	80	139.005	5.417	1034
Solution 4	140	Dual 12 bit	80	98.140	7.669	2585
Solution 4	80	Dual 12 bit	80	181.683	7.233	2585
Solution 4	nA	Dual 12 bit	80	140.155	5.069	2585
Solution 5	140	Dual 12 bit	80	134.642	7.285	4653
Solution 5	80	Dual 12 bit	80	254.025	9.218	4653

Solution 5	nA	Dual 12 bit	80	194.590	5.882	4653
Solution 6	140	Dual 12 bit	80	94.656	7.850	4653
Solution 6	80	Dual 12 bit	80	104.214	7.316	4653
Solution 6	nA	Dual 12 bit	80	99.680	5.193	4653
Solution 7	140	Dual 12 bit	80	288.615	8.056	4136
Solution 7	80	Dual 12 bit	80	329.806	8.901	4136
Solution 7	nA	Dual 12 bit	80	309.460	6.095	4136
Solution 1	100	Dual 12 bit	80	20.279	5.359	3619
Solution 1	140	Dual 12 bit	80	14.529	6.101	3619
Solution 1	nA	Dual 12 bit	80	17.650	3.998	3619
Solution 2	100	Dual 12 bit	80	56.721	5.436	3619
Solution 2	140	Dual 12 bit	80	37.383	6.002	3619
Solution 2	nA	Dual 12 bit	80	47.303	4.094	3619
Solution 3	100	Dual 12 bit	80	98.582	5.557	3619
Solution 3	140	Dual 12 bit	80	63.958	5.840	3619
Solution 3	nA	Dual 12 bit	80	81.517	3.992	3619
Solution 4	100	Dual 12 bit	80	150.243	5.484	1551
Solution 4	140	Dual 12 bit	80	96.730	7.110	1551
Solution 4	nA	Dual 12 bit	80	123.736	4.311	1551
Solution 4	100	Dual 12 bit	80	150.364	5.532	2585
Solution 4	140	Dual 12 bit	80	97.190	6.391	2585
Solution 4	nA	Dual 12 bit	80	124.021	4.334	2585
Solution 5	100	Dual 12 bit	80	210.641	6.830	5170
Solution 5	140	Dual 12 bit	80	134.936	5.974	5170
Solution 5	nA	Dual 12 bit	80	173.037	4.673	5170
Solution 6	100	Dual 12 bit	80	101.650	5.501	4653
Solution 6	140	Dual 12 bit	80	94.279	6.331	4653
Solution 6	nA	Dual 12 bit	80	98.216	4.393	4653
Solution 7	100	Dual 12 bit	80	316.220	7.211	4136
Solution 7	140	Dual 12 bit	80	288.765	6.660	4136
Solution 7	nA	Dual 12 bit	80	302.745	4.857	4136
Al	80	Dual 16 bit	80	2751.197	20.417	193
Ti	80	Dual 16 bit	80	12338.435	166.364	193
Fe	80	Dual 16 bit	80	16152.223	1157.928	193
Al	80	Dual 16 bit	25	2882.135	78.321	193
Ti	80	Dual 16 bit	25	12955.534	477.934	193
Fe	80	Dual 16 bit	25	19758.969	1009.698	193
MCP-96	100	Dual 16 bit	25	20377.269	1293.178	193
Al	100	Dual 16 bit	25	2478.663	13.487	193
Ti	100	Dual 16 bit	25	10016.249	316.328	193
Fe	100	Dual 16 bit	25	19055.109	847.758	193
Cu	100	Dual 16 bit	25	20226.912	1077.172	193
Mo	100	Dual 16 bit	25	20207.912	1138.691	193
Sn	100	Dual 16 bit	25	20090.104	1106.436	193
W	100	Dual 16 bit	25	20132.171	1114.303	193
Al	80	Dual 16 bit	50	2817.451	14.711	193
Ti	80	Dual 16 bit	50	12767.529	144.395	193
Fe	80	Dual 16 bit	50	18480.145	400.953	193
Al	100	Dual 16 bit	50	2416.575	11.284	193
Ti	100	Dual 16 bit	50	9825.301	134.843	193
Fe	100	Dual 16 bit	50	18516.347	620.292	193
MCP-96	100	Dual 16 bit	80	17693.399	411.173	193
Al	100	Dual 16 bit	80	2364.824	15.162	193
Ti	100	Dual 16 bit	80	9530.197	99.633	193
Fe	100	Dual 16 bit	80	17410.114	324.621	193
Cu	100	Dual 16 bit	80	17392.668	409.442	193
Mo	100	Dual 16 bit	80	17501.788	447.716	193
Sn	100	Dual 16 bit	80	17752.575	480.175	193
W	100	Dual 16 bit	80	17546.990	405.601	193
Al	140	Dual 16 bit	80	1761.487	13.108	193
Ti	140	Dual 16 bit	80	6011.389	19.742	193
Fe	140	Dual 16 bit	80	13313.964	135.181	193
Al	140	Dual 16 bit	25	1767.902	50.009	193
Ti	140	Dual 16 bit	25	6213.472	161.438	193
Fe	140	Dual 16 bit	25	13808.803	159.483	193
MCP-96	140	Dual 16 bit	25	23110.492	1374.346	193
Al	140	Dual 16 bit	25	1778.321	20.080	193
Ti	140	Dual 16 bit	25	6230.518	177.474	193
Fe	140	Dual 16 bit	25	13879.539	135.679	193
Cu	140	Dual 16 bit	25	17697.389	414.754	193
Mo	140	Dual 16 bit	25	23062.207	1265.316	193
Sn	140	Dual 16 bit	25	22988.788	1223.223	193
W	140	Dual 16 bit	25	22922.135	1257.092	193
Al	140	Dual 16 bit	50	1763.990	19.024	193
Ti	140	Dual 16 bit	50	6137.606	25.474	193
Fe	140	Dual 16 bit	50	13616.290	142.893	193
Al	140	Dual 16 bit	50	1766.197	19.537	193
Ti	140	Dual 16 bit	50	6158.140	28.137	193
Fe	140	Dual 16 bit	50	13682.819	118.310	193
MCP-96	140	Dual 16 bit	80	20695.130	351.094	193
Al	140	Dual 16 bit	80	1764.021	11.398	193
Ti	140	Dual 16 bit	80	6029.373	21.959	193
Fe	140	Dual 16 bit	80	13355.580	116.923	193
Cu	140	Dual 16 bit	80	16867.948	288.722	193
Mo	140	Dual 16 bit	80	20684.031	276.598	193
Sn	140	Dual 16 bit	80	20909.767	282.796	193
W	140	Dual 16 bit	80	20499.306	368.437	193
Al	3500	MVCT	80	1263.194	50.287	1015
Ti	3500	MVCT	80	2524.436	62.527	1015
Sn	3500	MVCT	80	4666.371	78.033	1015

Fe	3500	MVCT	80	5111.621	83.979	1015
Cu	3500	MVCT	80	5801.944	78.243	1015
Mo	3500	MVCT	80	6720.494	83.539	1015
MCP-96	3500	MVCT	80	7709.727	77.057	1015
W	3500	MVCT	80	13640.846	147.472	1015

Table C.2: Electron density and effective atomic number of all samples.

Material	Energy [kV]	Mode	Phantom radius [mm]	Mean CT Value	SD Mean CT Value	n Pixel
Al	80/140	Dual ED 16 bit	80	2.28	0.016	193
Ti	80/140	Dual ED 16 bit	80	3.438	0.069	193
Fe	80/140	Dual ED 16 bit	80	12.764	0.761	193
Al	80/140	Dual ED 16 bit	25	2.24	0.095	193
Ti	80/140	Dual ED 16 bit	25	3.349	0.171	193
Fe	80/140	Dual ED 16 bit	25	11.329	0.53	193
MCP-96	100/140	Dual ED 16 bit	25	25.297	1.429	193
Al	100/140	Dual ED 16 bit	25	2.45	0.066	193
Ti	100/140	Dual ED 16 bit	25	5.078	0.288	193
Fe	100/140	Dual ED 16 bit	25	11.718	0.553	193
Cu	100/140	Dual ED 16 bit	25	17.279	0.451	193
Mo	100/140	Dual ED 16 bit	25	25.534	1.114	193
Sn	100/140	Dual ED 16 bit	25	25.585	0.961	193
W	100/140	Dual ED 16 bit	25	25.482	0.982	193
Al	80/140	Dual ED 16 bit	50	2.256	0.065	193
Ti	80/140	Dual ED 16 bit	50	3.382	0.108	193
Fe	80/140	Dual ED 16 bit	50	11.874	0.25	193
Al	100/140	Dual ED 16 bit	50	2.439	0.075	193
Ti	100/140	Dual ED 16 bit	50	5.126	0.072	193
Fe	100/140	Dual ED 16 bit	50	11.819	0.205	193
MCP-96	100/140	Dual ED 16 bit	80	24.563	0.414	193
Al	100/140	Dual ED 16 bit	80	2.285	0.013	193
Ti	100/140	Dual ED 16 bit	80	3.495	0.017	193
Fe	100/140	Dual ED 16 bit	80	9.974	0.153	193
Cu	100/140	Dual ED 16 bit	80	17.387	0.768	193
Mo	100/140	Dual ED 16 bit	80	23.47	0.176	193
Sn	100/140	Dual ED 16 bit	80	24.913	0.302	193
W	100/140	Dual ED 16 bit	80	24.328	0.432	193
Al	80/140	Dual Zeff 16 bit	80	13.545	0.05	193
Ti	80/140	Dual Zeff 16 bit	80	22.987	0.329	193
Fe	80/140	Dual Zeff 16 bit	80	12.513	1.441	193
Al	80/140	Dual Zeff 16 bit	25	13.47	0.191	193
Ti	80/140	Dual Zeff 16 bit	25	22.86	1.141	193
Fe	80/140	Dual Zeff 16 bit	25	15.517	0.719	193
MCP-96	100/140	Dual Zeff 16 bit	25	7.098	0.014	193
Al	100/140	Dual Zeff 16 bit	25	11.912	0.066	193
Ti	100/140	Dual Zeff 16 bit	25	16.899	0.275	193
Fe	100/140	Dual Zeff 16 bit	25	15.299	0.836	193
Cu	100/140	Dual Zeff 16 bit	25	11.284	0.556	193
Mo	100/140	Dual Zeff 16 bit	25	7.1	0	193
Sn	100/140	Dual Zeff 16 bit	25	7.1	0	193
W	100/140	Dual Zeff 16 bit	25	7.1	0	193
Al	80/140	Dual Zeff 16 bit	50	13.523	0.097	193
Ti	80/140	Dual Zeff 16 bit	50	23.097	0.609	193
Fe	80/140	Dual Zeff 16 bit	50	14.794	0.222	193
Al	100/140	Dual Zeff 16 bit	50	11.926	0.057	193
Ti	100/140	Dual Zeff 16 bit	50	17.063	0.107	193
Fe	100/140	Dual Zeff 16 bit	50	15.29	0.46	193
MCP-96	100/140	Dual Zeff 16 bit	80	7.1	0	193
Al	100/140	Dual Zeff 16 bit	80	13.619	0.039	193
Ti	100/140	Dual Zeff 16 bit	80	23.112	0.158	193
Fe	100/140	Dual Zeff 16 bit	80	18.415	0.181	193
Cu	100/140	Dual Zeff 16 bit	80	9.308	1.566	193
Mo	100/140	Dual Zeff 16 bit	80	7.1	0	193
Sn	100/140	Dual Zeff 16 bit	80	7.1	0	193
W	100/140	Dual Zeff 16 bit	80	7.1	0	193
MCP-96	80/140	Dual ED 12 bit	80	4.069	0.004	19521
Al	80/140	Dual ED 12 bit	80	2.342	0.016	22106
Ti	80/140	Dual ED 12 bit	80	4.068	0.007	22623
Fe	80/140	Dual ED 12 bit	80	4.071	0.001	21072
Cu	80/140	Dual ED 12 bit	80	4.071	0.001	23140
Mo	80/140	Dual ED 12 bit	80	4.071	0.001	22623
Sn	80/140	Dual ED 12 bit	80	4.071	0.001	22106
W	80/140	Dual ED 12 bit	80	4.071	0.001	19004
MCP-96	100/140	Dual ED 12 bit	80	4.069	0.006	19521
Al	100/140	Dual ED 12 bit	80	2.343	0.019	22106
Ti	100/140	Dual ED 12 bit	80	4.067	0.009	22623
Fe	100/140	Dual ED 12 bit	80	4.07	0.002	21072
Cu	100/140	Dual ED 12 bit	80	4.07	0.002	23140
Mo	100/140	Dual ED 12 bit	80	4.071	0.001	22623
Sn	100/140	Dual ED 12 bit	80	4.071	0.001	22106
W	100/140	Dual ED 12 bit	80	4.071	0.001	19004
Lung	80/140	Dual ED 12 bit	80	0.446	0.027	19004
Adipose	80/140	Dual ED 12 bit	80	0.932	0.005	21072
Breast	80/140	Dual ED 12 bit	80	0.97	0.005	21589
CT Solid Water	80/140	Dual ED 12 bit	80	0.995	0.006	20555
Muscle	80/140	Dual ED 12 bit	80	1.025	0.006	21072
Brain	80/140	Dual ED 12 bit	80	1.05	0.005	21589
Liver	80/140	Dual ED 12 bit	80	1.065	0.005	21072
Water	80/140	Dual ED 12 bit	80	1.001	0.006	14868
Lung	100/140	Dual ED 12 bit	80	0.445	0.027	19004
Adipose	100/140	Dual ED 12 bit	80	0.931	0.004	21072
Breast	100/140	Dual ED 12 bit	80	0.97	0.004	21589

CT Solid Water	100/140	Dual ED 12 bit	80	0.994	0.004	20555
Muscle	100/140	Dual ED 12 bit	80	1.024	0.005	21072
Brain	100/140	Dual ED 12 bit	80	1.049	0.004	21589
Liver	100/140	Dual ED 12 bit	80	1.063	0.004	21072
Water	100/140	Dual ED 12 bit	80	1	0.004	14868
Inner Bone	80/140	Dual ED 12 bit	80	1.099	0.006	21072
B-200 Bone	80/140	Dual ED 12 bit	80	1.109	0.006	20555
CB2-30%	80/140	Dual ED 12 bit	80	1.271	0.006	21589
CB2-50%	80/140	Dual ED 12 bit	80	1.468	0.007	20038
Cortical Bone	80/140	Dual ED 12 bit	80	1.7	0.008	21589
Inner Bone	100/140	Dual ED 12 bit	80	1.098	0.004	21072
B-200 Bone	100/140	Dual ED 12 bit	80	1.107	0.004	20555
CB2-30%	100/140	Dual ED 12 bit	80	1.271	0.005	21589
CB2-50%	100/140	Dual ED 12 bit	80	1.467	0.005	20038
Cortical Bone	100/140	Dual ED 12 bit	80	1.704	0.006	21072
PMMA	80/140	Dual ED 12 bit	80	1.158	0.007	17453
Tecapeek	80/140	Dual ED 12 bit	80	1.234	0.008	17970
Tecadur	80/140	Dual ED 12 bit	80	1.35	0.013	17453
Tecaform	80/140	Dual ED 12 bit	80	1.365	0.008	17453
Teflon	80/140	Dual ED 12 bit	80	1.869	0.01	17970
PVC	80/140	Dual ED 12 bit	80	2.105	0.012	16936
PMMA	100/140	Dual ED 12 bit	80	1.158	0.005	17453
Tecapeek	100/140	Dual ED 12 bit	80	1.232	0.005	17453
Tecadur	100/140	Dual ED 12 bit	80	1.347	0.013	17970
Tecaform	100/140	Dual ED 12 bit	80	1.362	0.006	18487
Teflon	100/140	Dual ED 12 bit	80	1.87	0.007	17453
PVC	100/140	Dual ED 12 bit	80	2.139	0.01	16419
MCP-96	80/140	Dual ED 12 bit	14	4.069	0.005	21589
Al	80/140	Dual ED 12 bit	14	2.319	0.016	21072
Ti	80/140	Dual ED 12 bit	14	4.068	0.006	21589
Fe	80/140	Dual ED 12 bit	14	4.07	0.003	21072
Cu	80/140	Dual ED 12 bit	14	4.071	0.001	21072
Mo	80/140	Dual ED 12 bit	14	4.071	0	21589
Sn	80/140	Dual ED 12 bit	14	4.071	0.001	21589
W	80/140	Dual ED 12 bit	14	4.071	0.001	21072
MCP-96	100/140	Dual ED 12 bit	14	4.068	0.006	21589
Al	100/140	Dual ED 12 bit	14	2.319	0.019	21072
Ti	100/140	Dual ED 12 bit	14	4.069	0.004	21589
Fe	100/140	Dual ED 12 bit	14	4.07	0.002	21589
Cu	100/140	Dual ED 12 bit	14	4.07	0.002	21072
Mo	100/140	Dual ED 12 bit	14	4.071	0.001	21589
Sn	100/140	Dual ED 12 bit	14	4.071	0.001	21589
W	100/140	Dual ED 12 bit	14	4.071	0.001	20555
MCP-96	80/140	Dual ED 12 bit	25	4.069	0.005	21072
Al	80/140	Dual ED 12 bit	25	2.323	0.015	21589
Ti	80/140	Dual ED 12 bit	25	4.067	0.008	22623
Fe	80/140	Dual ED 12 bit	25	4.071	0.002	22623
Cu	80/140	Dual ED 12 bit	25	4.071	0.001	22106
Mo	80/140	Dual ED 12 bit	25	4.071	0.001	20555
Sn	80/140	Dual ED 12 bit	25	4.071	0.001	21072
W	80/140	Dual ED 12 bit	25	4.071	0.001	20555
MCP-96	100/140	Dual ED 12 bit	25	4.068	0.006	21589
Al	100/140	Dual ED 12 bit	25	2.324	0.018	21589
Ti	100/140	Dual ED 12 bit	25	4.065	0.012	22623
Fe	100/140	Dual ED 12 bit	25	4.07	0.002	22623
Cu	100/140	Dual ED 12 bit	25	4.07	0.002	22106
Mo	100/140	Dual ED 12 bit	25	4.071	0.001	20555
Sn	100/140	Dual ED 12 bit	25	4.071	0.001	21072
W	100/140	Dual ED 12 bit	25	4.071	0.001	20555
MCP-96	80/140	Dual ED 12 bit	50	4.07	0.002	21072
Al	80/140	Dual ED 12 bit	50	2.33	0.015	21072
Ti	80/140	Dual ED 12 bit	50	4.069	0.004	21589
Fe	80/140	Dual ED 12 bit	50	4.071	0.001	20038
Cu	80/140	Dual ED 12 bit	50	4.071	0.001	20555
Mo	80/140	Dual ED 12 bit	50	4.071	0.001	21589
Sn	80/140	Dual ED 12 bit	50	4.071	0.001	21072
W	80/140	Dual ED 12 bit	50	4.071	0.001	20038
MCP-96	100/140	Dual ED 12 bit	50	4.069	0.003	21072
Al	100/140	Dual ED 12 bit	50	2.333	0.017	21072
Ti	100/140	Dual ED 12 bit	50	4.069	0.005	21589
Fe	100/140	Dual ED 12 bit	50	4.07	0.002	20038
Cu	100/140	Dual ED 12 bit	50	4.071	0.001	20555
Mo	100/140	Dual ED 12 bit	50	4.071	0.001	21589
Sn	100/140	Dual ED 12 bit	50	4.071	0.002	21072
W	100/140	Dual ED 12 bit	50	4.071	0.001	20038
Water	80/140	Dual ED 12 bit	50	0.991	0.004	16419
Inner Bone	80/140	Dual ED 12 bit	50	1.088	0.004	20555
Lung	80/140	Dual ED 12 bit	50	0.439	0.029	21072
Water	100/140	Dual ED 12 bit	50	0.991	0.003	16419
Inner Bone	100/140	Dual ED 12 bit	50	1.087	0.003	20555
Lung	100/140	Dual ED 12 bit	50	0.438	0.028	21072
Water	80/140	Dual ED 12 bit	25	0.987	0.002	17453
Inner Bone	80/140	Dual ED 12 bit	25	1.083	0.003	21072
Lung	80/140	Dual ED 12 bit	25	0.439	0.026	21589
Water	100/140	Dual ED 12 bit	25	0.986	0.002	17453
Inner Bone	100/140	Dual ED 12 bit	25	1.081	0.002	21072
Lung	100/140	Dual ED 12 bit	25	0.438	0.026	21589
Tecapeek	80/140	Dual ED 12 bit	25	1.218	0.003	15902
Tecadur	80/140	Dual ED 12 bit	25	1.329	0.014	17970
Tecaform	80/140	Dual ED 12 bit	25	1.346	0.003	17453

Teflon	80/140	Dual ED 12 bit	25	1.849	0.003	17970
PVC	80/140	Dual ED 12 bit	25	2.073	0.008	17970
Tecapeek	100/140	Dual ED 12 bit	25	1.218	0.002	15902
Tecadur	100/140	Dual ED 12 bit	25	1.328	0.013	17970
Tecaform	100/140	Dual ED 12 bit	25	1.346	0.002	17453
Teflon	100/140	Dual ED 12 bit	25	1.849	0.003	17970
PVC	100/140	Dual ED 12 bit	25	2.11	0.008	17970
Tecapeek	80/140	Dual ED 12 bit	50	1.225	0.004	17453
Tecadur	80/140	Dual ED 12 bit	50	1.338	0.013	17970
Tecaform	80/140	Dual ED 12 bit	50	1.352	0.005	16936
Teflon	80/140	Dual ED 12 bit	50	1.858	0.005	17970
PVC	80/140	Dual ED 12 bit	50	2.087	0.009	17970
Tecapeek	100/140	Dual ED 12 bit	50	1.225	0.003	17453
Tecadur	100/140	Dual ED 12 bit	50	1.335	0.013	17970
Tecaform	100/140	Dual ED 12 bit	50	1.352	0.003	16936
Teflon	100/140	Dual ED 12 bit	50	1.856	0.004	17970
PVC	100/140	Dual ED 12 bit	50	2.121	0.008	17970
MCP-96	80/140	Dual Zeff 12 bit	80	7.447	0.085	19521
Al	80/140	Dual Zeff 12 bit	80	12.641	0.132	22106
Ti	80/140	Dual Zeff 12 bit	80	7.463	0.092	22623
Fe	80/140	Dual Zeff 12 bit	80	7.418	0.04	21072
Cu	80/140	Dual Zeff 12 bit	80	7.416	0.039	23140
Mo	80/140	Dual Zeff 12 bit	80	7.411	0.032	22623
Sn	80/140	Dual Zeff 12 bit	80	7.413	0.034	22106
W	80/140	Dual Zeff 12 bit	80	7.413	0.035	19004
MCP-96	100/140	Dual Zeff 12 bit	80	7.455	0.096	19521
Al	100/140	Dual Zeff 12 bit	80	12.611	0.167	22106
Ti	100/140	Dual Zeff 12 bit	80	7.477	0.113	22623
Fe	100/140	Dual Zeff 12 bit	80	7.421	0.044	21072
Cu	100/140	Dual Zeff 12 bit	80	7.421	0.046	23140
Mo	100/140	Dual Zeff 12 bit	80	7.413	0.035	22623
Sn	100/140	Dual Zeff 12 bit	80	7.415	0.038	22106
W	100/140	Dual Zeff 12 bit	80	7.414	0.038	19004
Lung	80/140	Dual Zeff 12 bit	80	0	0	19004
Adipose	80/140	Dual Zeff 12 bit	80	6.256	0.204	21072
Breast	80/140	Dual Zeff 12 bit	80	6.887	0.169	21589
CT Solid Water	80/140	Dual Zeff 12 bit	80	7.641	0.13	20555
Muscle	80/140	Dual Zeff 12 bit	80	7.65	0.132	21072
Brain	80/140	Dual Zeff 12 bit	80	6.384	0.178	21589
Liver	80/140	Dual Zeff 12 bit	80	7.632	0.123	21072
Water	80/140	Dual Zeff 12 bit	80	7.396	0.143	14868
Lung	100/140	Dual Zeff 12 bit	80	0	0	19004
Adipose	100/140	Dual Zeff 12 bit	80	6.292	0.177	21072
Breast	100/140	Dual Zeff 12 bit	80	6.908	0.148	21589
CT Solid Water	100/140	Dual Zeff 12 bit	80	7.671	0.119	20555
Muscle	100/140	Dual Zeff 12 bit	80	7.685	0.119	21072
Brain	100/140	Dual Zeff 12 bit	80	6.405	0.158	21589
Liver	100/140	Dual Zeff 12 bit	80	7.681	0.112	21072
Water	100/140	Dual Zeff 12 bit	80	7.428	0.12	14868
Inner Bone	80/140	Dual Zeff 12 bit	80	10.09	0.098	21072
B-200 Bone	80/140	Dual Zeff 12 bit	80	10.063	0.099	20555
CB2-30%	80/140	Dual Zeff 12 bit	80	10.718	0.086	21589
CB2-50%	80/140	Dual Zeff 12 bit	80	12.11	0.076	20038
Cortical Bone	80/140	Dual Zeff 12 bit	80	13.005	0.074	21589
Inner Bone	100/140	Dual Zeff 12 bit	80	10.118	0.081	21072
B-200 Bone	100/140	Dual Zeff 12 bit	80	10.1	0.081	20555
CB2-30%	100/140	Dual Zeff 12 bit	80	10.737	0.068	21589
CB2-50%	100/140	Dual Zeff 12 bit	80	12.101	0.059	20038
Cortical Bone	100/140	Dual Zeff 12 bit	80	12.917	0.059	21072
PMMA	80/140	Dual Zeff 12 bit	80	6.5	0.216	17453
Tecapeek	80/140	Dual Zeff 12 bit	80	6.314	0.215	17970
Tecadur	80/140	Dual Zeff 12 bit	80	9.548	0.116	17453
Tecaform	80/140	Dual Zeff 12 bit	80	6.925	0.179	17453
Teflon	80/140	Dual Zeff 12 bit	80	8.271	0.128	17970
PVC	80/140	Dual Zeff 12 bit	80	11.608	0.093	16936
PMMA	100/140	Dual Zeff 12 bit	80	6.521	0.17	17453
Tecapeek	100/140	Dual Zeff 12 bit	80	6.375	0.18	17453
Tecadur	100/140	Dual Zeff 12 bit	80	9.605	0.094	17970
Tecaform	100/140	Dual Zeff 12 bit	80	6.987	0.178	18487
Teflon	100/140	Dual Zeff 12 bit	80	8.311	0.11	17453
PVC	100/140	Dual Zeff 12 bit	80	11.194	0.086	16419
MCP-96	80/140	Dual Zeff 12 bit	14	7.447	0.078	21589
Al	80/140	Dual Zeff 12 bit	14	12.859	0.133	21072
Ti	80/140	Dual Zeff 12 bit	14	7.449	0.077	21589
Fe	80/140	Dual Zeff 12 bit	14	7.422	0.048	21072
Cu	80/140	Dual Zeff 12 bit	14	7.416	0.038	21072
Mo	80/140	Dual Zeff 12 bit	14	7.41	0.03	21589
Sn	80/140	Dual Zeff 12 bit	14	7.411	0.031	21589
W	80/140	Dual Zeff 12 bit	14	7.416	0.037	21072
MCP-96	100/140	Dual Zeff 12 bit	14	7.461	0.103	21589
Al	100/140	Dual Zeff 12 bit	14	12.826	0.168	21072
Ti	100/140	Dual Zeff 12 bit	14	7.448	0.067	21589
Fe	100/140	Dual Zeff 12 bit	14	7.421	0.045	21589
Cu	100/140	Dual Zeff 12 bit	14	7.419	0.042	21072
Mo	100/140	Dual Zeff 12 bit	14	7.413	0.033	21589
Sn	100/140	Dual Zeff 12 bit	14	7.413	0.033	21589
W	100/140	Dual Zeff 12 bit	14	7.412	0.032	20555
MCP-96	80/140	Dual Zeff 12 bit	25	7.444	0.079	21072
Al	80/140	Dual Zeff 12 bit	25	12.79	0.133	21589
Ti	80/140	Dual Zeff 12 bit	25	7.466	0.1	22623

Fe	80/140	Dual Zeff 12 bit	25	7.418	0.04	22623
Cu	80/140	Dual Zeff 12 bit	25	7.416	0.038	22106
Mo	80/140	Dual Zeff 12 bit	25	7.412	0.033	20555
Sn	80/140	Dual Zeff 12 bit	25	7.412	0.033	21072
W	80/140	Dual Zeff 12 bit	25	7.416	0.036	20555
MCP-96	100/140	Dual Zeff 12 bit	25	7.456	0.087	21589
Al	100/140	Dual Zeff 12 bit	25	12.766	0.165	21589
Ti	100/140	Dual Zeff 12 bit	25	7.486	0.139	22623
Fe	100/140	Dual Zeff 12 bit	25	7.421	0.045	22623
Cu	100/140	Dual Zeff 12 bit	25	7.419	0.042	22106
Mo	100/140	Dual Zeff 12 bit	25	7.415	0.038	20555
Sn	100/140	Dual Zeff 12 bit	25	7.414	0.035	21072
W	100/140	Dual Zeff 12 bit	25	7.417	0.038	20555
MCP-96	80/140	Dual Zeff 12 bit	50	7.432	0.048	21072
Al	80/140	Dual Zeff 12 bit	50	12.708	0.125	21072
Ti	80/140	Dual Zeff 12 bit	50	7.442	0.059	21589
Fe	80/140	Dual Zeff 12 bit	50	7.418	0.041	20038
Cu	80/140	Dual Zeff 12 bit	50	7.415	0.036	20555
Mo	80/140	Dual Zeff 12 bit	50	7.412	0.032	21589
Sn	80/140	Dual Zeff 12 bit	50	7.415	0.038	21072
W	80/140	Dual Zeff 12 bit	50	7.41	0.03	20038
MCP-96	100/140	Dual Zeff 12 bit	50	7.44	0.061	21072
Al	100/140	Dual Zeff 12 bit	50	12.685	0.155	21072
Ti	100/140	Dual Zeff 12 bit	50	7.452	0.074	21589
Fe	100/140	Dual Zeff 12 bit	50	7.421	0.046	20038
Cu	100/140	Dual Zeff 12 bit	50	7.417	0.037	20555
Mo	100/140	Dual Zeff 12 bit	50	7.414	0.035	21589
Sn	100/140	Dual Zeff 12 bit	50	7.417	0.041	21072
W	100/140	Dual Zeff 12 bit	50	7.411	0.031	20038
Water	80/140	Dual Zeff 12 bit	50	7.448	0.098	16419
Inner Bone	80/140	Dual Zeff 12 bit	50	10.214	0.067	20555
Lung	80/140	Dual Zeff 12 bit	50	0	0	21072
Water	100/140	Dual Zeff 12 bit	50	7.434	0.081	16419
Inner Bone	100/140	Dual Zeff 12 bit	50	10.223	0.061	20555
Lung	100/140	Dual Zeff 12 bit	50	0	0	21072
Water	80/140	Dual Zeff 12 bit	25	7.517	0.068	17453
Inner Bone	80/140	Dual Zeff 12 bit	25	10.31	0.045	21072
Lung	80/140	Dual Zeff 12 bit	25	0	0	21589
Water	100/140	Dual Zeff 12 bit	25	7.525	0.059	17453
Inner Bone	100/140	Dual Zeff 12 bit	25	10.336	0.05	21072
Lung	100/140	Dual Zeff 12 bit	25	0	0	21589
Tecapeek	80/140	Dual Zeff 12 bit	25	6.387	0.076	15902
Tecadur	80/140	Dual Zeff 12 bit	25	9.761	0.05	17970
Tecaform	80/140	Dual Zeff 12 bit	25	7.048	0.064	17453
Teflon	80/140	Dual Zeff 12 bit	25	8.405	0.045	17970
PVC	80/140	Dual Zeff 12 bit	25	11.839	0.051	17970
Tecapeek	100/140	Dual Zeff 12 bit	25	6.36	0.068	15902
Tecadur	100/140	Dual Zeff 12 bit	25	9.781	0.04	17970
Tecaform	100/140	Dual Zeff 12 bit	25	7.061	0.058	17453
Teflon	100/140	Dual Zeff 12 bit	25	8.416	0.052	17970
PVC	100/140	Dual Zeff 12 bit	25	11.392	0.049	17970
Tecapeek	80/140	Dual Zeff 12 bit	50	6.311	0.113	17453
Tecadur	80/140	Dual Zeff 12 bit	50	9.654	0.063	17970
Tecaform	80/140	Dual Zeff 12 bit	50	6.992	0.097	16936
Teflon	80/140	Dual Zeff 12 bit	50	8.327	0.07	17970
PVC	80/140	Dual Zeff 12 bit	50	11.689	0.058	17970
Tecapeek	100/140	Dual Zeff 12 bit	50	6.301	0.103	17453
Tecadur	100/140	Dual Zeff 12 bit	50	9.688	0.059	17970
Tecaform	100/140	Dual Zeff 12 bit	50	6.999	0.082	16936
Teflon	100/140	Dual Zeff 12 bit	50	8.374	0.074	17970
PVC	100/140	Dual Zeff 12 bit	50	11.279	0.059	17970

Danksagung

Ich möchte Prof. Wolfgang Schlegel für die freundliche Aufnahme in seine Abteilung danken. Prof. Oliver Jäkel danke ich dafür, dass ich diese Arbeit in seiner Gruppe schreiben durfte und er mir dabei immer seine volle Unterstützung gewährte. Besonders dankbar bin ich für die Möglichkeit, die Ergebnisse meiner Arbeit auf nationalen und internationalen Konferenzen vorstellen zu dürfen. Prof. Uwe Oelfke danke ich für die Übernahme der Erstbetreuung. Prof. Heinz-Peter Schlemmer danke ich für die Unterstützung durch seine Abteilung. Prof. Marc Kachelrieß danke ich dafür, dass er sich Zeit genommen hat, meine Fragen zur CT zu beantworten.

Steffen Greilich danke ich für seine stets kompetente und umfangreiche Betreuung, die in ihrem Engagement weit über das übliche Maß hinausging. Bei Nora Hünemohr bedanke ich mich ebenfalls für ihre kompetente Betreuung und Unterstützung sowie die vielen hilfreichen Diskussionen. Allen Mitgliedern der Arbeitsgruppe an DKFZ und HIT danke ich für die immer entspannte und positive Atmosphäre, die das Arbeiten sehr angenehm gemacht hat.

Herrn Dr. Bernhard Krauss danke ich für die Berechnung der Elektronendichte- und Z_{eff}-Bilder sowie für das geduldige Beantworten meiner zahlreichen Fragen zur CT.

Bei HIT danke ich Benjamin Ackermann für seine Unterstützung bei den WEPL-Messungen sowie die Bereitstellung von Messergebnissen und der stöchiometrischen HLUT. Stephan Brons danke ich für seine großzügige Hilfe bei den WEPL-Messungen, Swantje Ecker für die Beantwortung meiner Fragen zur Therapie bei HIT und Mona Splinter dafür, dass ich ihre MVCT HLUT verwenden durfte.

Stefan Kuchenbecker und Sebastian Faby danke ich für ihre Unterstützung und die Bereitstellung eines simulierten CT-Bildes.

Martina Jochim danke ich für die stets unkomplizierten Messungen am DECT-Scanner des DKFZ sowie ihre großes Engagement.

Armin Runz und Gernot Echner danke ich für ihre Unterstützung und Geduld bei der Planung und Anfertigung der Messproben und Phantome.

Schließlich möchte ich meinen Eltern dafür danken, dass sie jedes meiner Ziele stets bedingungslos unterstützt und mich in jeder nur erdenklichen Hinsicht gefördert haben. Ohne sie wäre ich ohne Zweifel nicht, wo ich heute bin.

Erklärung:

Ich versichere, dass ich diese Arbeit selbstständig verfasst habe und keine anderen als die angegebenen Quellen und Hilfsmittel benutzt habe.

Heidelberg, den 30.11.2012 .....